Dyadic Contrast Function And Quadratic Forward Model For Radio Frequency Tomography

BY

VITTORIO PICCO
B.S. Politecnico di Torino, Italy, 2007
M.S. Politecnico di Torino, Italy, 2010
M.S. University of Illinois at Chicago, USA, 2010

THESIS

Submitted as partial fulfillment of the requirements
for the degree of Doctor of Philosophy in Electrical and Computer Engineering
in the Graduate College of the
University of Illinois at Chicago, 2014

Chicago, Illinois

Defense Committee:

Danilo Erricolo, Chair and Advisor
Natasha Devroye
Piergiorgio L.E. Uslenghi
Jaideva Goswami, Schlumberger
Carey Rappaport, Northeastern University
Francesco Soldovieri, IREA-CNR
Michael Wicks, University of Dayton

Alla mia famiglia, in particolare a chi non c'è più.

ACKNOWLEDGMENTS

Prof. Erricolo has truly been an academic father to me, guiding me throughout my graduate studies, always making sure that I had the best conditions to do my work and introducing me to some of the best minds in my field of research, both in academia and in the industry. He has also been a friend outside of the University and for all of this I am very grateful.

I would like to thank all the members of my defense committee, for their comments and feedback on my dissertation from its proposal through its defense. I am also grateful to Dr. Gianluca Gennarelli and Dr. Lorenzo Lo Monte for their collaboration and supervision on some specific aspects of my research and for sharing their expertise with me.

A sincere thank you goes to my lab mates and to the undergraduates research assistants without whose help I could not simply have made it so far.

Of course, I cannot forget all the members of the ECE department, without whose work I would not have been able to sort out all the academic and financial matters into which I so easily get lost.

Finally, thanks to all the friends and family members who made my time in Chicago not just productive but truly enjoyable.

VP

CONTRIBUTION OF AUTHORS

Chapter 1 and Chapter 2 provide a literature review that places my dissertation question in the context of the larger field and highlights the significance of my research question. Most of the review is related to work developed by Dr. Lo Monte as part of his Ph.D. research. Chapter 3 describes a system that is used by the whole Andrew Electromagnetic Laboratory at the University of Illinois at Chicago. The system has been developed as a collaborative effort between many lab members, including Mr. Tadahiro Negishi, Mr. Marcus Stephens and Mr. Douglas Spitzer. Together with Chapter 4 it provides an in-depth description and analysis of the results published in a journal article where I was first author. Mr. Tadahiro Negishi contributed to the content of the manuscript and Dr. Danilo Erricolo contributed to the writing, while Mr. Douglas Spitzer assisted with the data collection. Chapter 5 and Chapter 6 describe results already published in conference papers and in preparation for publication in journal papers. Authorship of these papers is shared between myself, Mr. Tadahiro Negishi, Dr. Francesco Soldovieri and Dr. Danilo Erricolo. Chapter 7 represents my synthesis of the research presented in this dissertation and my overarching conclusions.

VP

TABLE OF CONTENTS

TABLE OF CONTENTS (Continued)

CHAPTER **PAGE**

LIST OF TABLES

LIST OF FIGURES

LIST OF FIGURES (Continued)

FIGURE **PAGE**

LIST OF FIGURES (Continued)

FIGURE **PAGE**

LIST OF FIGURES (Continued)

FIGURE **PAGE**

LIST OF FIGURES (Continued)

LIST OF FIGURES (Continued)

FIGURE **PAGE**

LIST OF FIGURES (Continued)

FIGURE **PAGE**

LIST OF FIGURES (Continued)

LIST OF ABBREVIATIONS

ART	Algebraic Reconstruction Technique
CG	Conjugate Gradient
CW	Continuous Wave
GPR	Ground Penetrating Radar
HDBT	Hard and Deeply Buried Target
RFT	Radio Frequency Tomography
RX	Receiving antenna
SAR	Synthetic Aperture Radar
UGF	Underground Facility
TSVD	Truncated Singular Values Decomposition
TX	Transmitting antenna
UIC	University of Illinois at Chicago
VIE	Volume Integral Equation

SUMMARY

Radio Frequency Tomography is an underground imaging technology that aims to reconstruct extended, deeply buried objects such as tunnels or Underground Facilities (UGF). A network of sensors collects scattered electromagnetic field samples, which are processed to obtain 2D or 3D images of the complex dielectric permittivity profile of the volume under investigation. Unlike systems such as Synthetic Aperture Radar (SAR) or Ground Penetrating Radar (GPR) which normally employ wide-band pulses, RF Tomography uses Continuous Wave (CW) signals to illuminate the scene. The information about the target is not retrieved by relying on bandwidth but by exploiting spatial, frequency and/or polarization diversity.

Interestingly, RF Tomography can be readily adapted to obtain images of targets in free space. In this context, in the Andrew Electromagnetics Laboratory of the University of Illinois at Chicago, a measurement system aimed to validate experimentally the performance of RF Tomography has been designed and built. Experimental data have been used to validate its forward model, different inversion algorithms, its performance in terms of resolution and the ability of the system to distinguish between metallic and non-metallic targets.

In the specific case of imaging of metallic targets, this thesis proposes to extend the capabilities of RF Tomography by introducing a dyadic permittivity contrast. Electromagnetic scattering from a thin, wire-like object placed in free space with its main axis at

an angle with respect to the incident electric field is studied. It is possible to show that for this configuration a fundamental difference exists between a metallic and a dielectric object. This phenomenon can be modeled into MaxwellâĂŹs equations by using a dyadic permittivity contrast, as it is commonly done when studying crystals. As a result a new formulation of the RF Tomography forward model is obtained, based on a dyadic contrast function. Reconstruction of this dyad allows to estimate not only the location and shape, but also the spatial orientation of the target.

In addition, this dissertation proposes an alternative modification of the forward model which removes some limitations caused by the Born approximation. Traditionally, the Born approximation is used to linearize the inherently non-linear forward model. This approximation is valid if the scatterer is small and does not interact strongly with other objects. A quadratic forward model represents a more correct formulation of the scattering phenomenon, and it allows to attempt quantitative reconstruction. Numerical results are presented to highlight the advantages that such a formulation provides over the Born approximation.

CHAPTER 1

INTRODUCTION

The exploration of the underground and, more in general, the ability to see what cannot be seen by optical means has attracted the attention of researchers for decades. The fields that can benefit from such techniques are very numerous and include geology, archeology, medicine, defense and security, exploration sciences, and others. Different disciplines have often developed different methods to achieve similar goals. Great advances in mathematics and physics have allowed to find common denominators in a once very fragmented and empirical field. The Radon transform, for example, was introduced in 1917 (1) and provided the basis for imaging applications that will appear later on – around the late 1960s.

Now the term *imaging* is used in these different disciplines to indicate a very well defined process: the visual reconstruction of a physical quantity considered of interest (2; 3; 4; 5).

The methods used to make images of inaccessible objects are many. Depending on the application one could employ radio frequency waves, infrared emission, direct or alternating electrical current, ultrasounds, vibrations, etc (6; 7; 8). The choice of the technique to employ follows a series of practical considerations. One of the most important ones is the availability of a medium to carry the signals: electromagnetic (EM) waves do not need a medium to propagate, but sound waves as well as DC currents do. Restricting the attention to cases when a medium able to carry both acoustic and electromagnetic information is present, the choices are still many. The wavelength of ultrasound systems are much shorter

than the wavelengths of many EM systems thus having implications on the resolution. To increase the resolution of operation of an EM system one can increase the frequency, but this can have harmful effects on the human body; the energy of an EM wave is proportional to its frequency, as described by Planck's relation (9) and if the frequency is very high the EM wave becomes an ionizing radiation, i.e. it is able to disrupt molecular structure at an atomic level, causing nuclear damage and possibly cancer. Safety of operation must be a priority over the resolution in medical imaging. On the other hand, in very deep underground exploration, where no life is present and the risk of contamination of the environment is extremely low, the use of high-energy waves or nuclear radiation is permissible. After all these decisions have been carefully considered, the problem of practical implementation arises. In EM systems it is unrealistic to assume to be able to measure the phase of a wave with the same precision regardless of the frequency of operation. In addition, the frequency of operation and the type of signals employed (narrow-band versus wide-band, for example) have important consequences on how far waves can travel before being greatly attenuated. Furthermore, the properties of the medium where the waves travel greatly affect the direction of propagation of such waves, as well as the distance they can travel. This explains why acoustic imaging is adopted in applications that apparently have nothing in common, such as prenatal imaging in the medical field and the imaging of lake and ocean floors: in both cases the presence of liquids poses great challenges to the use of EM waves, so acoustic methods are preferred.

In conclusion, any imaging process is affected by dozens of variables, which combine in a great number of possibilities. Imaging system differ greatly because they must be designed by carefully keeping into account all these factors. However, regardless of the physical process or discipline, an imaging process usually follows three common steps.

First, the quantity of interest is defined and analyzed. In this step one answers the questions What do we want to see? and What is a physical quantity that can help us see that? For example, a doctor could be interested in seeing a tumor, and could take the density of the tissue as a measurable physical quantity of interest. Alternatively, a geophysicist might be interested in knowing the thickness of a layer of rock, and could choose the electrical resistivity of such formation as a measurable quantity that can assist her in doing so.

Second, with the help of physics, a *forward model* is created. The forward model links the quantity being reconstructed (density of tissue, electrical resistivity) with a measurable quantity. If the doctor chooses to use X-rays to probe the tissue, he will measure the attenuation of an electromagnetic radiation as it goes through the body. The geophysicist, instead, could measure the voltage observed at two electrodes that are injecting a constant current into the rock. Both scientists need an equation that converts the desired quantity into the measured quantity: that equation is the forward model. It is important to point out that the model is just a simplified description of reality, which is obtained making assumptions and approximations during its derivation. For example, even though the physics of EM propagation is fully described by Maxwell's equations, in all environment and at any

frequency, important practical differences exist between propagation in a perfectly homogeneous medium and a highly anisotropic body showing large differences in conductivity and permittivity. While deriving the forward model these consideration can be translated into different mathematical approximations that can better deal with the practical problems at hand.

Third, the measured data go through a process called *inversion*. This step corresponds to converting the measured quantity into the desired quantity and obtaining an image. Apparently this step is very simple: the geophysicist, for example, can recover the rock resistance R from her forward model $V = RI$ without great difficulty. However, in most cases this step is not trivial. The forward model used by the doctor can be such that tiny variations in the measured quantity can lead to huge variations in the reconstructed quantity, thus making his diagnosis problematic; a forward model such as the doctor's is called mathematically *ill-conditioned*. In addition, it could happen that for practical reasons one cannot collect as many data points as would be needed for a good reconstruction, leading to an image which is only an approximation of the real object; this is an *under-determined* problem. A more exotic case is the one where the forward model is not linear: what if the current injected by the geophysicist into the rock formation is not constant as he thinks, but depends on the resistivity itself of the rock being measured? Only a non-linear model can represent correctly this situation and it is not nearly as easy to invert as the simple $V = RI$. In conclusion, the inversion procedure presents many obstacles that must be carefully considered in order to obtain a meaningful image.

This dissertation is involved with all the basic steps just described, and focuses on Radio Frequency Tomography (10; 11; 12), a novel technique aimed to reconstruct extended, deeply buried objects, such as tunnels. The goal of this work is to introduce two separate modifications to the RF Tomography forward model, which allow to extract information about the imaging object which was previously unavailable and to obtain a better image quality under controlled conditions. Before delving into this, a full description of RF Tomography is provided, and some of the first measurement results obtained under controlled conditions are presented and discussed. In addition, iterative inversion algorithms have been developed to overcome some of the limitations given by regularized direct inversion methods.

This thesis is structured as follows.

In Chapter 2 RF Tomography is introduced, by describing its principles of operation, its forward model and a few inversion techniques. This description will make clear some of the limitations and challenges that this thesis will address.

In Chapter 3 a prototype experimental system designed at the Andrew Electromagnetics Laboratory of the University of Illinois at Chicago is described. The system allows to realize an experimental validation of RF Tomography in free space, scaled for operations in the microwave region.

In Chapter 4 two inversion algorithms are described, designed to overcome the limitations of the methods currently used. One of the methods is based on the Conjugate Gradient algorithm, and the other on the Algebraic Reconstruction Technique.

Chapter 5 is then dedicated to explain the idea of a dyadic contrast function. The simple case of scattering from metallic and non-metallic thin cylinders is analyzed both analytically and numerically, and provides motivation for the introduction of the dyadic contrast function. The forward model is then modified and images are obtained from simulated data. Results are presented to show the advantages that this technique can provide to the final user.

Chapter 6 instead describes an alternative modification of the forward model, which consists in introducing a quadratic formulation which replaces the classical linear one. This modification allows for better quantitative reconstruction of the contrast function under controlled conditions and is tested with both simulated and measured data.

In the end Chapter 7 summarizes the goals of this work, how they have been accomplished and presents ideas for further research.

CHAPTER 2

RADIO FREQUENCY TOMOGRAPHY

The goal of this chapter is to introduce RF Tomography forward model and all the fundamental concepts that form the base for this thesis. Although none of the topics discussed here are intended to be original, it is necessary to introduce them so as to better understand what follows, and to establish the notation used thereafter. The discussion of mathematical concepts is left to a bare minimum and the reader is referred to appropriate references when necessary. An original, complete and detailed description of RF Tomography is found in (10; 13; 11; 12; 14; 15) and (16; 17; 18; 19; 20; 21; 22; 23; 24; 25; 26; 27; 28; 29; 30; 31; 32; 33; 34; 35; 36; 37; 38; 39; 40; 41; 42; 43; 44; 45; 46).

Radio Frequency Tomography is an underground imaging technique that is based on the use of simple, spatially distributed sensors operating at a fixed frequency, that are used to illuminate a target with an electromagnetic wave, measure its scattered electric (or magnetic) field, and process it to obtain an image of the target itself, as shown in Figure 1.

In order to be able to make images of deeply buried targets, RF Tomography uses signals in the High Frequency band (3–30 MHz) or lower. In addition, it does not use pulses, i.e wide-band signals, because their broad frequency spectrum would be affected greatly by dispersion. The information about the target is not carried by a pulse, but by the amplitude and phase of a monochromatic scattered wave and by sampling the target in the spatial, rather than frequency, domain. Key to successful imaging is the spatial distribution of the

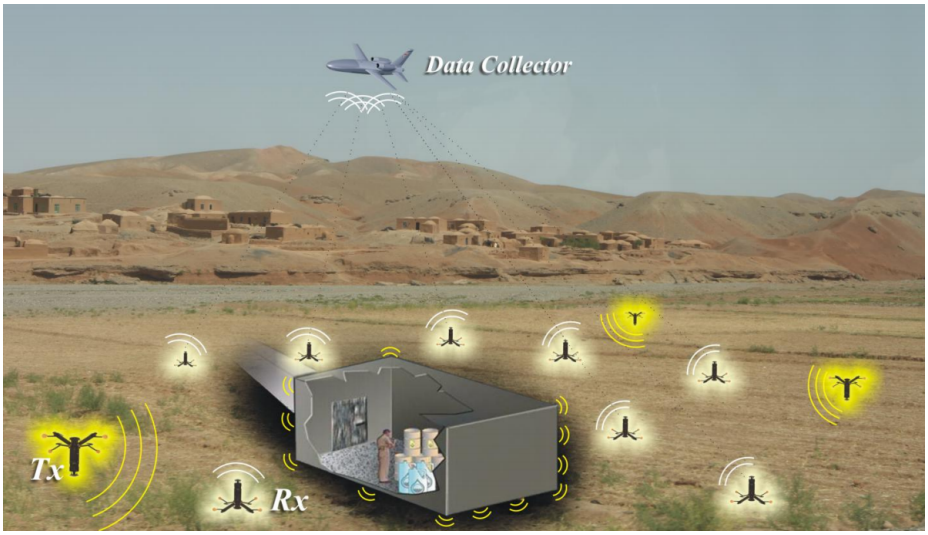

Figure 1. Schematic representation of RF Tomography, from (10).

sensor, which are deployed in a large area surrounding the target. In short, RF Tomography obtains images of targets by trading bandwidth for spatial sampling. This is opposed to other techniques such as the Synthetic Aperture Radar (SAR) or Ground Penetrating Radar (GPR), which use a localized transmitter and receiver and probe the target using wide-band signals. The choice of using monochromatic signals has the advantage that the antennas used in RFT are very simple, normally just short electric or magnetic dipoles. Also, the measurement equipment attached to the antenna is greatly simplified because it does not require to deal with wide-band signals.

RF Tomography proves to be very flexible. Its forward model can be readily adapted to operate under different conditions: free space, below-ground, thru-wall, and others. The main difference between these scenarios is given not by the model itself, but by the fact that

there arise constraints that limit the locations where sensors can be placed. Changing the location of the antennas or the medium where they are located does not change the forward model, but changes the quality of the images that can be obtained because it modifies the information retrieved by spatial sampling.

The advantages of RF Tomography over other other EM techniques are that it can achieve deeper soil penetration and reconstruct very large targets or allow surveillance of extended areas; it does not necessarily require operators on site; it can be operated remotely; it is an overall cheaper technology because it greatly simplifies the hardware requirements.

2.1 Forward model

RF Tomography is based on a Volume Integral Equation (VIE). The transmitting and receiving antennas (TX and RX, respectively) are placed around the area under investigation. If imaging is performed for underground targets this means placing the antennas either just below or just above the air-earth interface. Instead, in free-space, the antennas are placed around the target, or around the container where the target is hidden. Either way, the position of each antenna is identified with a vector, $\mathbf{r}^{\mathrm{t}}$ for the TX and $\mathbf{r}^{\mathrm{r}}$ for the RX. Since antennas are modeled as short dipoles, their orientation in space is described with a unit vector, $\mathbf{a}^{\mathrm{t}}$ for the TX and $\mathbf{a}^{\mathrm{r}}$ for the RX.

The next quantity involved in the forward model is the contrast function, i.e. the quantity being reconstructed. This is a complex scalar that represents the difference of the permittivity values between the target and the medium where the target is embedded. It is

represented with $v(\mathbf{r}')$, with the auxiliary vector $\mathbf{r}'$ indicating the particular position where the contrast function is being reconstructed. Formally, $v(\mathbf{r}')$ is given by

$$v(\mathbf{r}') = \left[\varepsilon(\mathbf{r}') - \varepsilon_b\right] - j\left[\frac{\sigma(\mathbf{r}') - \sigma_b}{2\pi f \varepsilon_0}\right]. \tag{2.1}$$

In Equation 2.1, $\varepsilon(\mathbf{r}')$ and $\sigma(\mathbf{r}')$ indicate the dielectric permittivity and the conductivity of the object, while ε_b and σ_b indicate the dielectric permittivity and the conductivity of the background medium.

Then, the propagation of the monochromatic RF signal is described using a Green's function. The choice of the Green's function depends on the medium and on the location of the antennas. For example, for below-ground imaging, a different Green's function is used depending on whether the antennas are located above or below the air-earth interface. In free space a classical spherical wave formulation is normally used. Since the forward model is vectorial, it involves *dyadic* Green's functions, i.e. they keep into account different orientations of TXs and RXs thanks to a tensor formulation. One dyad is used to describe the propagation of the RF signal from TX to target, and another for the propagation from target to RX. Therefore the two dyads are normally indicated as $\mathbf{G}(\mathbf{r}^{\mathrm{t}}, \mathbf{r}')$ and $\mathbf{G}(\mathbf{r}', \mathbf{r}^{\mathrm{r}})$.

Lastly, the total field received by the RXs is identified with E^{t}, which is the superposition of the incident field E^{i} transmitted into the space and the field scattered by the target, E^{s}. Only the E^{s} component carries information about the target. To better describe the fact

that the scattered field is measured at the location of a specific receiving antenna, for the field transmitted by a specific transmitter, it is written as $E^{\mathrm{s}}(\mathbf{r}^{\mathrm{t}}, \mathbf{r}^{\mathrm{r}})$.

In conclusion, the forward model as derived in (10) (see also (47)) is

$$\begin{aligned} E^{\mathrm{t}}(\mathbf{r}^{\mathrm{t}}, \mathbf{r}^{\mathrm{r}}) &= E^{\mathrm{i}}(\mathbf{r}^{\mathrm{t}}, \mathbf{r}^{\mathrm{r}}) + E^{\mathrm{s}}(\mathbf{r}^{\mathrm{t}}, \mathbf{r}^{\mathrm{r}}) \\ &= E^{\mathrm{i}}(\mathbf{r}^{\mathrm{t}}, \mathbf{r}^{\mathrm{r}}) + Qk_0^2 \iiint_D \mathbf{a}^{\mathrm{r}} \cdot \mathbf{G}(\mathbf{r}^{\mathrm{r}}, \mathbf{r}')v(\mathbf{r}')\mathbf{G}(\mathbf{r}', \mathbf{r}^{\mathrm{t}}) \cdot \mathbf{a}^{\mathrm{t}} d\mathbf{r}', \end{aligned} \tag{2.2}$$

where the constant Q is used to keep into account additional factors which depend on the antennas used (short dipole vs. small loop, for example), and the symbol D is used to identify the domain of investigation.

In Equation 2.2, two assumptions have been made. First, the unknown is a scalar quantity, i.e. each voxel is associated with one complex number. In chapter 5 a new formulation is described which uses a dyad to represent the contrast function, allowing to retrieve additional information about the target. Second, to obtain Equation 2.2 the Born approximation has been adopted, by replacing the total field inside the integral with the incident field only. More details about this and an another formulation which does not make this assumption are presented in Chapter 6.

The forward model is then discretized. For each measurement, i.e. each pair of TX and RX, the space is partitioned into voxels, and the integral turns into a summation

$$E^{\mathrm{s}}(\mathbf{r}^{\mathrm{t}}, \mathbf{r}^{\mathrm{r}}) = Q \sum_{\mathbf{r}' \in D} \mathbf{a}^{\mathrm{r}} \cdot \mathbf{G}(\mathbf{r}^{\mathrm{r}}, \mathbf{r}')v(\mathbf{r}')\mathbf{G}(\mathbf{r}', \mathbf{r}^{\mathrm{t}}) \cdot \mathbf{a}^{\mathrm{t}} d\mathbf{r}'. \tag{2.3}$$

The summation can be represented as a linear algebra vector multiplication, by collecting in a vector all the known terms (everything except $v(\mathbf{r}')$ and in another vector the unknown $v(\mathbf{r}')$. Each element of the vectors represents a different voxel $\mathbf{r}'$ being reconstructed. Then, all the vectors corresponding to different measurements can be stacked into a matrix that collects all the known terms. In the end the matrix formulation of the forward model is obtained

$$\mathbf{E}^{\mathrm{s}} = \mathbf{L} \cdot \mathbf{v}. \tag{2.4}$$

If the number of transmitters is M, the number of receivers is N and the domain of investigation has been partitioned into P voxels, the vector $\mathbf{E}^{\mathrm{s}}$ has size $MN \times 1$, the matrix $\mathbf{L}$ has size $MN \times P$, and the unknown vector $\mathbf{v}$ has size $P \times 1$.

A few comments can be made about this formulation. First, the matrix problem is largely under-determined. While it is reasonable to have tens of transmitters and receivers, the number of voxels can easily be in the order of tens of thousands, depending on the size of the area being reconstructed and on the size of the voxels. Therefore, since the matrix $\mathbf{L}$ is rectangular, it is not possible to invert it directly.

Second, the problem is normally ill-conditioned. This is a classic issue arising in inverse problems. When trying to recover $\mathbf{v}$, a small error in the measurement vector $\mathbf{E}^{\mathrm{s}}$ is greatly amplified by the condition number of the matrix. This is largely due to the fact that it is difficult to collect a truly independent set of measurements. For square matrices,

ill-conditioning is associated with eigenvalues very close to zero, similarly to how rank deficiency is associated with eigenvalues equal to zero. Since the matrix $\mathbf{L}$ is rectangular, the eigenvalues are not defined, but its singular values s represent the generalization of the eigenvalues. Therefore, singular values of small absolute value are symptom of an ill-conditioned rectangular matrix, suggesting that some rows of the matrix $\mathbf{L}$ are close to being linearly dependent.

These considerations have particular importance when designing inversion algorithms, able to successfully reconstruct the vector $\mathbf{v}$ and therefore leading to meaningful images.

2.2 Inversion algorithms

If the matrix $\mathbf{L}$ were not ill-conditioned, the inversion could be performed using a pseudo-inverse matrix. For matrices with more columns than rows this is normally computed as (48)

$$\mathbf{L}^{\dagger} = \mathbf{L}^{H} \left(\mathbf{L}\mathbf{L}^{H} \right)^{-1}, \tag{2.5}$$

where the notation ^{H} indicates the Hermitian transpose. Unfortunately the inversion performed in this way is poor, because of ill-conditioning. Since the condition number can be written as

$$\kappa(\mathbf{L}) = ||\mathbf{L}^{\dagger}|| \cdot ||\mathbf{L}||, \tag{2.6}$$

a high condition number means that the pseudo-inverse is really just a numerically bad approximation of a matrix that should verify the relationship $\mathbf{L}^{\dagger} \cdot \mathbf{L} = \mathbf{I}$, $\mathbf{I}$ being the identity matrix. The result is that small noise in the data lead to extremely large errors in the reconstruction of $\mathbf{v}$ if Equation 2.5 is used.

The solution to the ill-conditioning problem is to use regularization techniques. These methods attempt to mitigate the effects of small singular values by attenuating them or completely eliminating them from the computation of the pseudo-inverse.

One of the most popular methods is called the Truncated Singular Value Decomposition (TSVD) (49), which is closely related to other methods such as the Tikhonov regularization (50). These and other methods based on similar principles are called *direct* because as a result of the computation they return directly the final solution. This is opposed to the approach taken by *iterative* methods, which start from a rough approximation of the solution and then refine it in an iterative matter (48).

Truncated Singular Value Decomposition

TSVD works as follows. First, the Singular Value Decomposition is performed, which decomposes the matrix $\mathbf{L}$ as

$$\mathbf{L} = \mathbf{U}\mathbf{S}\mathbf{V}^{H}. \tag{2.7}$$

The diagonal matrix $\mathbf{S}$ contains the singular values of the matrix $\mathbf{L}$ usually sorted in descending order of magnitude. The pseudo-inverse can be easily written in terms of its singular value decomposition terms as

$$\mathbf{L}^{\dagger} = \mathbf{V}\mathbf{S}^{-1}\mathbf{U}^{H}. \tag{2.8}$$

Since $\mathbf{S}$ is diagonal, its inverse is obtained simply by replacing every nonzero diagonal entry by its reciprocal and transposing the resulting matrix.

Since the small singular values are the ones that create reconstruction problems, they are simply cut off, and so are the corresponding generalized eigenvectors contained in the matrices $\mathbf{U}$ and $\mathbf{V}$. The regularized truncated pseudo-inverse, therefore, is found as

$$\tilde{\mathbf{L}}^{\dagger} = \mathbf{V}_k\mathbf{S}_k^{-1}\mathbf{U}_k^{H}, \tag{2.9}$$

where k indicates the number of singular values that have been retained. The dimension of the final matrix is unchanged, because the truncation of $\mathbf{V}$ is done only on its columns, and the truncation of $\mathbf{U}^H$ is done only on its rows. However, the small singular values responsible for the ill-conditioning are not part of the regularized truncated pseudo-inverse. The final solution is found by a simple matrix multiplication

$$\mathbf{v} = \tilde{\mathbf{L}}^{\dagger} \cdot \mathbf{E}^{\mathrm{s}}. \tag{2.10}$$

The TSVD is an extremely popular method to obtain regularized solutions of ill conditioned problems. Another solution, possibly even more popular, is the Tikhonov regularization, which is similar both in terms of results and theoretical approach. Instead of simply cutting the small singular values, the Tikhonov regularization reduces their effect by scaling them with an appropriate regularizing parameter λ.

Both methods have drawbacks. TSVD is based on a very computationally heavy operation, the singular value decomposition. In addition, it is not clear how to choose the regularization parameter k. One way is simply to manually guess *a posteriori*, judging subjectively the quality of the reconstructed image; a more rigorous method is to analyze the L-curve (51; 52), which is described briefly in the following.

When finding a regularized solution of an under-determined, ill-conditioned problem, it is possible to plot two quantities as function of the regularization parameter. The first is the norm of the solution itself, $||\mathbf{v}||_2$, the other is the norm of the residual $r = ||\mathbf{E}^{\mathrm{s}} - \mathbf{L} \cdot \mathbf{v}||$. Plotting the first versus the second, a curve that looks like a capital L is often obtained (see Figure 2).

Each point on the L-curve corresponds to a different solution. Oftentimes, the best solution to the problem is the one corresponding to the k (or λ for Tikhonov regularization) at the knee of the curve. For example, in Figure 2 a $\lambda = 0.01$ will return a good solution.

This choice is somewhat subjective, because after all it relies on the quality of the image as it is perceived by the final user; for some problems it might not be the best. In other cases, the knee might not be easy to identify, or the method itself might fail in the case of

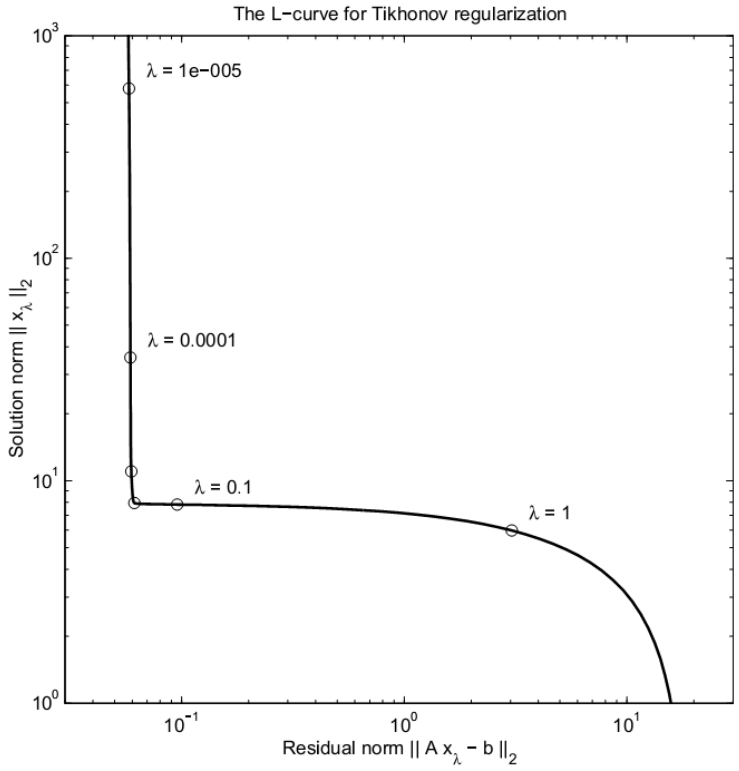

Figure 2. Example of an L-curve for an ill-conditioned problem. The points on the curve identified with different values of λ correspond to different values of the regularization parameter in a Tikhonov regularization. A similar behavior is obtained for TSVD for different values of k. Image obtained from (52).

solutions which are dominated by the first few SVD components (52). In these cases the choice of k is not simple.

In addition, the solutions returned by any regularized method are often blurry and poorly resolved. This is because the regularization has the property of obtaining a faster

convergence for low frequency components[1] (53). The regularization acts as a low-pass filter. This behavior is often desirable, because it reduces high frequency noise, but it also limits the performance of the inversion, which is unable to return images with sharp transitions and which tends to overestimate the effect of small, localized artifacts. The L-curve can be seen as a graph which separates blurry images from noisy images: the solution often lies in the middle but it is just the choice between the lesser of two evils.

The drawbacks displayed by regularized direct methods motivated research into alternative approaches. In particular, iterative methods have been investigated and are described in Chapter 4.

---

[1]Frequency here is intended as spatial frequency, in the context of the spatial Fourier transform of the solution image.

CHAPTER 3

AN RFT PROTOTYPE MEASURING SYSTEM

The performance evaluation of RF Tomography has been until now performed by means of computer simulations (11; 12; 14; 54; 55), the main reason being the practical difficulty in executing field measurements. The operating frequency, the availability of antennas, the location of a measurement site and the availability of known buried targets make the full-scale implementation of RF Tomography a rather challenging task. Some preliminary tests have been attempted (56), but have highlighted some of these practical problem.

Nonetheless, the possibility to verify in practice the theory developed about RF Tomography is very important. Laboratory experiments can provide a lot of information as well as guidelines on how to tackle the more difficult task of full-scale field measurements. The possibility of conducting scaled experiments at the Andrew Electromagnetics Laboratory at the University of Illinois at Chicago has therefore been investigated (57; 58; 59; 60; 61; 62).

Three fundamental requirements dictated the choice of these laboratory experiments. First, the goal of reconstruction: in RF Tomography the goal is to identify the location of a target, which does not require the accurate reconstruction of its electrical properties. The target is assumed to be an isolated anomaly, with sharp contrast with respect to the host medium, and with simple shape. Second, the measurement conditions: RF Tomography has been originally developed for reasons of detection and surveillance in defense systems, thus dealing in possible hostile environments. Successful imaging needs to be achieved

with a limited number of sensors and must be robust against missing or broken antennas. Third, the time required to process data to obtain images: short times are critical in RF Tomography because the goal is to obtain real time information about the target position and, possibly, to perform tracking. It is also imperative to retrieve and process information quickly because when sensors are deployed in a hostile environment, they may no longer be available at some point.[1]

All these requirements depend upon the availability of a physical system to collect measurements. A complete prototype system has therefore been designed, which allowed to recreate in a scaled version the fundamental building blocks of RF Tomography and, most importantly, to collect and process real world data for validation purposes.

The measurement system has been designed as a compromise between two opposing constraints. On one hand is the desire to reproduce as closely as possible an actual RFT system, to obtain a meaningful experimental validation; on the other hand are practical limitations that impose to limit the cost and the sources of error as well as guarantee the repeatability of the measurements. Therefore, choices were made which affected the type and number of antennas used, the operating frequency, the positioning system, the targets that could be used for imaging, and the type of tests that could be made on the system.

---

[1]Excerpt from (15)

3.1 Mechanics

The most important choice made involved the architecture of the measurement system. The chosen system is bi-static, i.e. it uses two antennas at a time. A positioning system would move these antennas in space, synthesizing multiple bi-static measurements, and therefore effectively realizing a fully multi-static (multiple illumination and multiple view) system.

This choice simplified the system both mechanically and electrically. Mechanically, because only two antennas need to be precisely placed, thus reducing the cost and the sources of errors. Electrically, because the absence of multiple co-located antennas in the same area – often within each other's near field (63) – reduces the electromagnetic interference and their mutual coupling.

In addition, the antennas move along circular paths, rather than performing linear scans. This choice has been made because most simulations presented in the literature are made according to this criteria, and also because antennas surrounding the target provide a great spatial diversity, with the target that can be observed from all angles.

As a result, an automated antenna positioning system has been designed, built, and programmed, and it is shown in Figure 3. The apparatus moves the antennas, samples the electric field, and stores the measurement data for later analysis. (For a detailed description of the system refer to Appendix A.)

The antennas are moved using two stepper motors, controlled by a PC via a controller board. Precise positioning of the antennas is paramount to achieve good quality images.

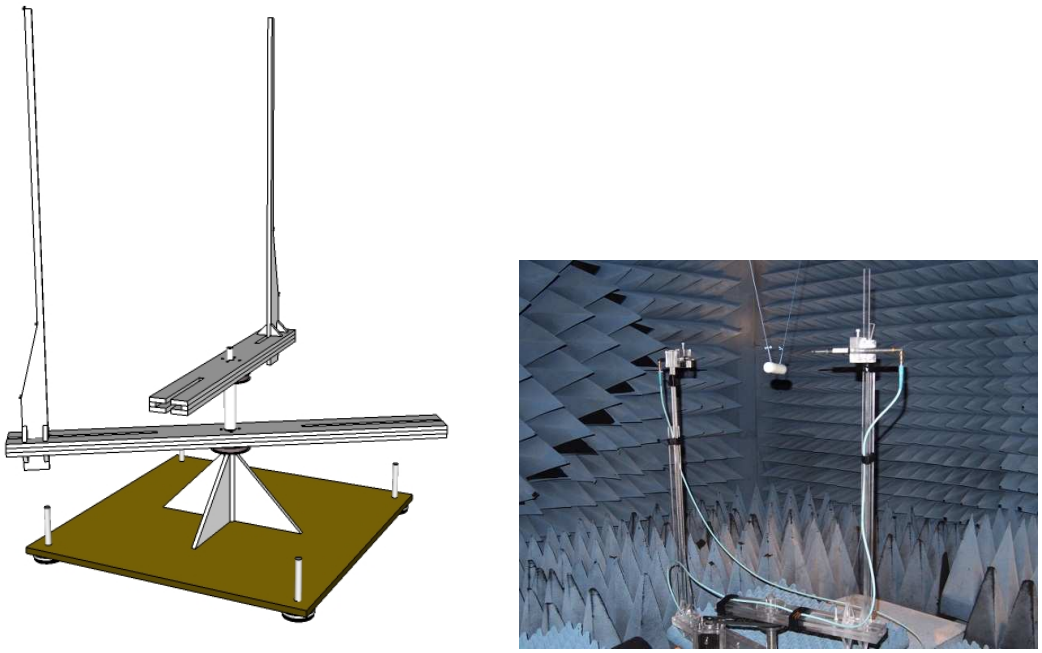

(a) (b)

Figure 3. The measuring system. Figure (a) shows a 3D CAD model prototype. Figure (b) shows a photo of the actual system at work: the TX is on the left, the RX is on the right, and a target is visible in the top-center, hanging from the ceiling.

Angular positioning with an error significantly smaller than 1° is achieved by using stepper motors in micro-stepping mode, and by using a pulley-belt system with a gear ratio of 4:1. The system is controlled by a LabVIEW ^{TM}application, which coordinates the movement of the antennas with the RF measurements.[1]

---

[1]Excerpt from (15)

In terms of limitations, the movement of the antennas is restricted to a 2D plane, with the possibility of choosing different planes for transmitting and receiving antennas. This is consistent with the RFT formulation, where antennas are scattered on the ground and are therefore approximately on the same plane. Also, each of the two antennas is mounted on its own positioning arm: this implies that the antennas cannot rotate around the same circumference, but instead rotate around concentric circles. Finally, one of the motor's support stands has been placed along the trajectory of rotation of one of the arms: while this simplifies the construction, it also limits the movement of the lower arm to approximately 285°.

3.2 RF design

The first and probably most important choice for the RF design is the choice of the operating frequency. The frequency must be sufficiently high so as to provide a good scaling factor, but not too high so as to compromise accuracy in the measurement of the phase, due to positioning errors. Given the precision achievable by the antenna positioner, data is usually collected around 3 GHz.

Simple half-wavelength dipoles are used in the experiments instead of the electrically short dipoles of the forward model. This choice was made because half-wavelength dipoles are more readily available, provide a much higher radiation resistance, and have a lower reflection coefficient to allow for a more efficient use of the input power. In the examples showed in this chapter the antennas were operated at 3.16 GHz ($\lambda \approx 9.5$ cm), with a transmit power of 20 dBmW. The choice of the operating frequency has been refined after

measuring the reflection coefficient S_{11} of the antennas. Plots of the reflection coefficient for both antennas are available in Figure 4.

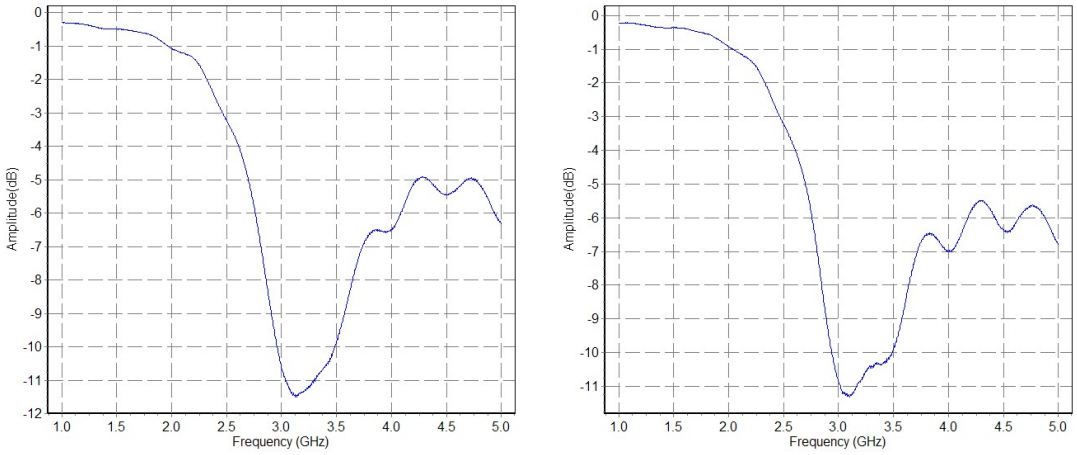

Figure 4. Reflection coefficient S_{11} for the two dipole antennas used in the measurements. Although the antennas are nominally operating at 3 GHz, the actual lowest reflection point for both antennas is located close to 3.2 GHz.

A Vector Network Analyzer (HP 8753ES) measured the scattering parameter S_{21}. For each measurement 16 samples were taken and averaged to reduce additive white Gaussian noise effects. The measurements were taken in an anechoic room to further reduce unde-

sired reflections and to mitigate external RF sources in the same frequency range. TM polarization (i.e., vertical, perpendicular to the floor plane) was used.[1]

3.3 Background subtraction and calibration

The forward model described in Equation 2.2 is based under the assumption that it is possible to separate the incident field E^{i} from the total field E^{t}, so as to obtain the scattered field only. In the laboratory this can be done by taking two measurements: in the first step the target is placed in the scene and a first measurement is taken, thus obtaining E^{t}. In the second step the target is removed and the environment only is measured, thus obtaining E^{i}. The two quantities are subtracted and the scattered field E^{s} is obtained.

This procedure is usually called *background subtraction* and is easy to perform in a laboratory, although it requires to double the number of measurements taken, see for example (62). In a real application, however, background subtraction is not applicable because the target cannot be removed from the scene. An important area of research is therefore the development of procedures that allow to extract the scattered part of the field from the total field. These are commonly referred to as *Direct Path Removal* techniques, and might involve software, hardware, or a combination of the two. Since our laboratory experiments did not require the use of these techniques a simple background subtraction is performed, but it is important to know that it represents an important assumption.

---

[1]Excerpt from (15)

Background subtraction might not be sufficient to achieve good imaging results. Although the theory describes a forward model that links a permittivity contrast function to the scattered electric field, in the laboratory it is more convenient to measure a different quantity. In fact, a Vector Network Analyzer measures the scattering parameters, which are dimensionless quantities which indicates ratios of power waves. Even though the scattering parameters provide an indication of the magnitude and phase of the measured electric field, they are not the same thing.

In order to overcome this issue, a calibration operation should be performed. There are different ways to do this, but all methods share a common trait: comparing the measurement of a known quantity against well-established numerical results or analytical formulas. Therefore some calibration methods (63; 64; 65; 66) use *standard targets*, i.e. objects whose scattering properties are very well established. These target are normally spheres, spheroidal objects, corner or tetrahedral reflectors and wedges. The field scattered from one or more of these objects is measured in the laboratory under veru well controlled conditions and is then compared to the field predicted by exact mathematical results. Other methods do not use any standard target but simply normalize the measurement to the field expected in free space (67), which can also be very well described by analytical formulas.

In both cases corrections coefficients are then applied to the measured data in order to obtain the best match between measurement and theory. In order for these procedures to work it is extremely important that the coefficients calculated are applied without any

change to all measurements, otherwise the calibration operation turns into a scientifically unsound data manipulation.

The operation adopted for the system described in this chapter consists in using the measured scattering parameter S_{21} in the absence of the target (i.e., the incident field E^{i}) and compare it to the expected value of the electric field that would be predicted by standard EM formulas. In summary, the developed procedure works as follows: E^{i} and S_{21} are linked as

$$E^{i}(\mathbf{r}^{t}, \mathbf{r}^{r}) = C(\mathbf{r}^{t}, \mathbf{r}^{r}) S_{21}(\mathbf{r}^{t}, \mathbf{r}^{r}), \tag{3.1}$$

that is, for each combination of antenna positions $(\mathbf{r}^{t}, \mathbf{r}^{r})$, E^{i} obtained from formulas is compared to the measured S_{21}, and the complex coefficients C (one per position) are computed. These coefficients are then re-used to convert the measured S_{21} in the presence of the target into the total field E^{t}.

This method has the advantage of not requiring standard targets, and is very easily implemented. It must also be pointed out that the measurement system has been designed for qualitative and not quantitative reconstruction. Therefore there is no need to calibrate the actual numerical value of the reconstructed dielectric permittivity contrast function against the material properties of a known scatterer.

CHAPTER 4

ITERATIVE INVERSION ALGORITHMS

This chapter is dedicated to describing two main inversion algorithms developed to invert RF Tomography data.

Section 2.2 introduced some direct methods used to solve under-determined, ill-conditioned, dense and large linear systems of equations. Those methods are all direct methods, i.e. they attempt to find a solution to the problem $\mathbf{E}^s = \mathbf{L} \cdot \mathbf{v}$ in one step, by using some regularization procedure. In particular, the most common method used in RF Tomography is the Truncated Singular Values Decomposition (TSVD) (10; 11; 68).

In this chapter an imaging scenario is chosen, which highlights both strengths and weaknesses of TSVD. Then, the new developed methods that allow for the introduction of physical constraints are presented and discussed.

4.1 Reference scenario

In the reference scenario a simple target is imaged. It consists of a short section of a PVC pipe: its outer diameter is 4.8 cm, its height is 5 cm, its thickness is 4 mm; the dielectric constant of PVC is estimated to be $\varepsilon_r = 2.5$ with negligible conductivity ($\tan(\delta) = 0.004$ at 3 GHz). The object is illuminated from 11 positions along a circumference of radius 38.4 cm, uniformly spaced between 0° and 280°. The electric field is sampled at 20 locations along a circumference of radius 15.4 cm, uniformly spaced between 0° and 360°. All images

shown here are obtained from real-world measurements collected at UIC with the system described in Chapter 3

A 3D model of the target, along with the location of the antennas, is shown in Figure 5.

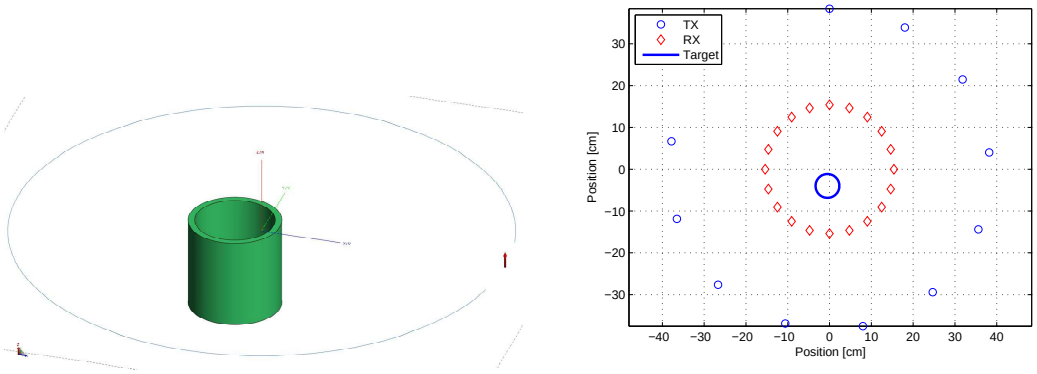

(a) (b)

Figure 5. Figure (a) shows a 3D model of the PVC pipe used in the measurement. The red arrow in the right part of the image represents one of the positions of the receiving antenna. Figure (b) shows all the positions used in the measurement.

All images are obtained considering a square domain of investigation of side equal to 20 cm, centered around the center of rotation of the antennas, and divided into 75 pixels per side. Each pixel is therefore 2.67 mm (or approximately $\lambda/37$). This leads to a problem with $75 \times 75 = 5625$ unknowns which must be reconstructed from 220 measurements. The conditioning number $\kappa(\mathbf{L})$ turns out to be approximately equal to 1.3×10^5.

4.2 Example of TSVD reconstruction

Reconstruction using TSVD is satisfactory, and is shown in Figure 6. The object is reconstructed in the correct location and its shape is preserved, although the thickness of the pipe is exaggerated. The image is affected by noise and presents a few artifacts, which are however weak when compared to the main target.

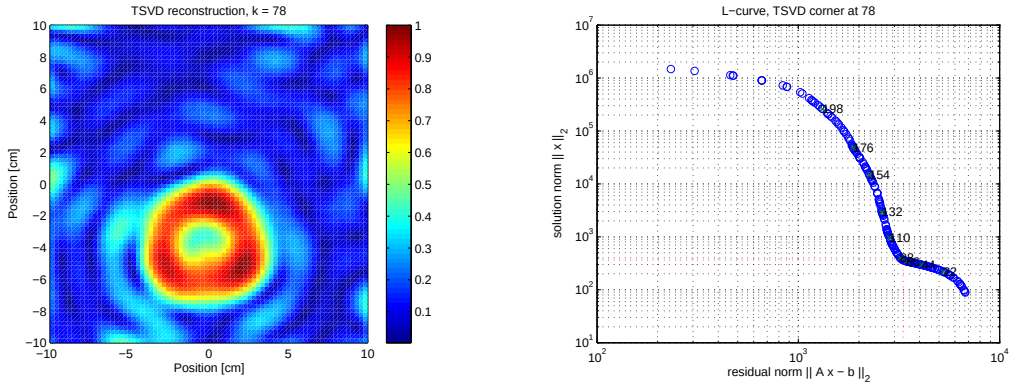

(a) (b)

Figure 6. Figure (a) shows the reconstruction obtained with TSVD in terms of magnitude of the complex dielectric permittivity contrast function, $|\mathbf{v}|$. The image is obtained by retaining $k = 78$ out of 220 singular values: the number has been automatically determined by identifying the corner of the L-curve (b).

The imaging result depends greatly on the number of singular values that are retained in the inversion, as shown in Figure 7. In addition, the TSVD reconstruction provides a solution that does not make physical sense (see Figure 8): both real and the imaginary

parts of **v** are negative, while it is clear that the real part (dielectric permittivity) must be positive.

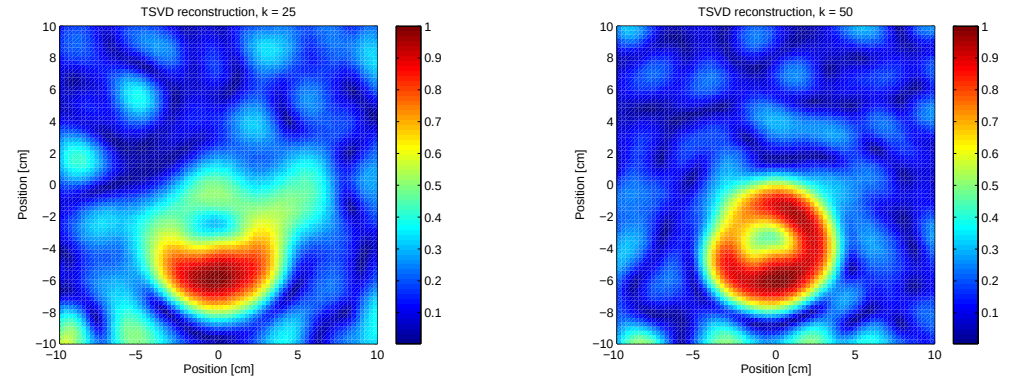

(a) $k = 25$ (b) $k = 50$

(c) $k = 100$ (d) $k = 125$

Figure 7. Reconstruction quality as function of the number of singular values retained. The solution rapidly goes from over smoothed (a), to meaningful (b), to useless (c-d)

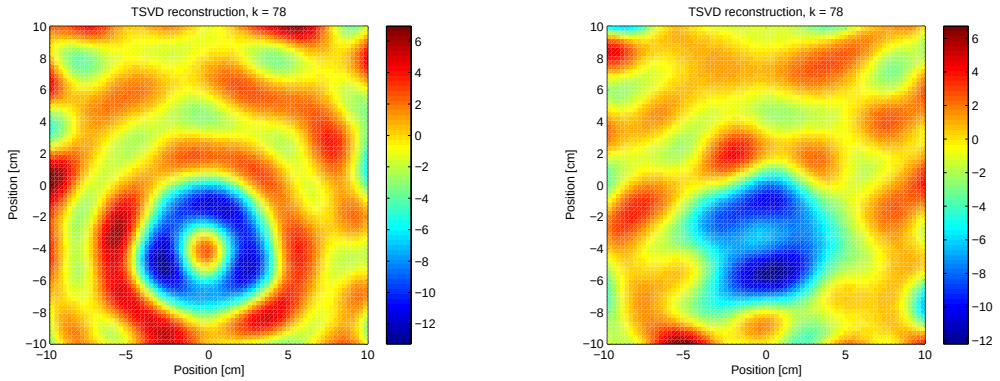

(a) $\Re(\mathbf{v})$ (b) $\Im(\mathbf{v})$

Figure 8. Real (a) and imaginary (b) parts of the solution retrieved by TSVD, for $k = 78$. The real part is negative although this does not make sense physically.

On a recent desktop computer (quad-core CPU operating at 3.7 GHz, 8 GB of memory) the time required to generate each image is approximately 4 seconds. The result is not bad, because the code was not pre-compiled or optimized. However, on a less recent laptop computer (single core CPU operating at 1.9 GHz, 1.5 GB of memory) reconstruction is impossible: the algorithm crashes because the singular value decomposition exhausts the memory of the computer.

4.3 Conjugate Gradient

The Conjugate Gradient algorithm (69; 70) is a very popular method for solving linear systems of equations. It is based on the steepest descent method and it improves on it by choosing in a smarter way the direction where to look for the solution at every iteration. The difference between the two methods can be efficiently explained with a simple example.

Suppose the minimum of a convex cost function needs to be found. The method of steepest descent starts from an initial guess, computes the gradient of the function and moves along that direction (search line) until a minimum in the gradient is reached. From that point, it computes a new gradient and it follows it again, repeating this process until a minimum in the function is reached. Thus, the method follows at every iteration a *steepest descent* path. It turns out that while moving along the search line, the function is minimized when the gradient is perpendicular to it. Therefore in the steepest descent method each step will always be taken in a direction perpendicular to the direction taken at the previous step. The phenomenon is depicted in Figure 9.

When dealing with particularly "oval" functions, unless the starting point is a particularly good one, the steepest descent method will need an extremely long time to find the solution because it will keep moving left and right along perpendicular search lines.

The Conjugate Gradient (CG) method addresses this problem by noticing that it would be better to move not along the direction of steepest descent, but along a direction that would minimize the number of steps necessary to find the minimum of the target function. This thesis is not concerned with the details of the CG algorithm, but there are many

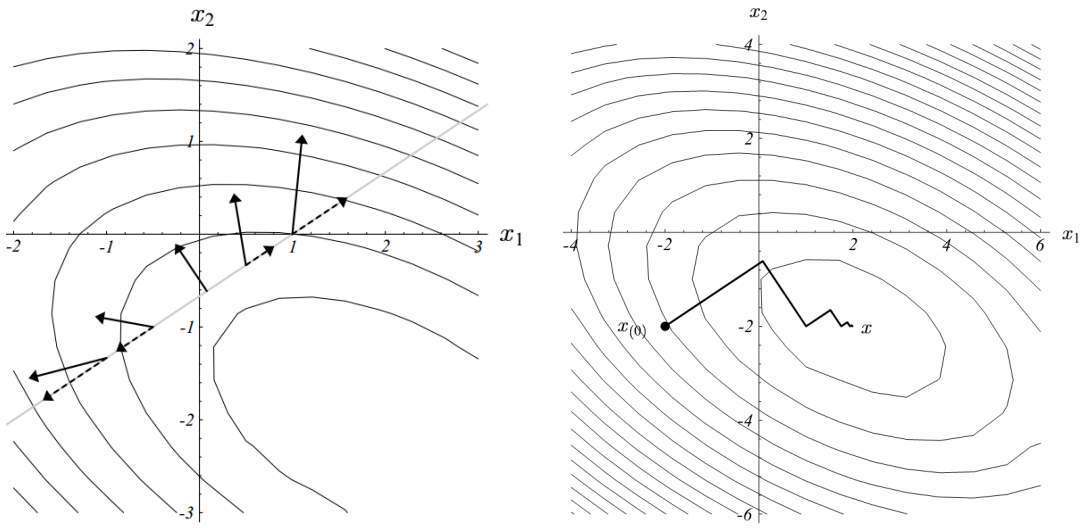

Figure 9. The steepest descent method at work. The function is minimized along a certain search line when the gradient is perpendicular to it (a). The path taken is therefore made of orthogonal segments (b). ©1994 by Jonathan Richard Shewchuk (71)

excellent references that discuss them exhaustively, (48) and (71) particularly. In a nutshell, by properly exploiting some properties of the search directions and of the residuals at every step, the CG method is guaranteed to find the solution of an n-dimensional problem in n steps. In the example used before, the CG method finds the minimum solution in 2 steps, as shown in Figure 10.

The beauty of CG is that it is very efficient, it works naturally with complex numbers, it does not require computationally heavy operations such as the Singular Value Decomposition, and it can be more or less easily customized so as to enforce some constraints on the solution. For example, the starting point can be chosen as the origin (the null vector) and

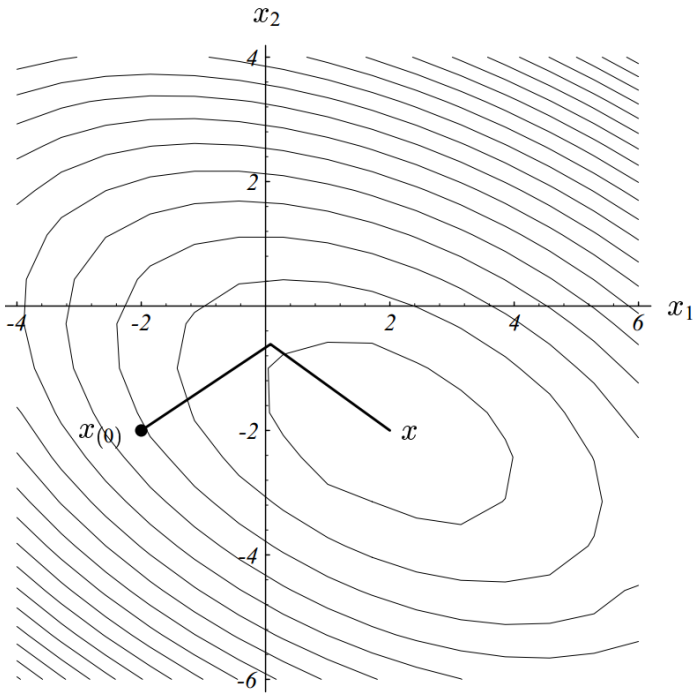

Figure 10. The CG method at work. Compare this convergence path, that takes 2 steps, with the one followed by steepest descent, in Figure 9b. ©1994 by Jonathan Richard Shewchuk (71)

then it can be enforced that the path of convergence only includes positive numbers. This can be done to apply some physical constraints on the final solution returned. Even though from a mathematical point of view it might make sense to move in a certain direction because the cost function is minimized, from a physics point of view the solution thus found might not make sense.

In addition, it is usually convenient to stop the iterative process before the minimum of the target function is actually found. Considering the details of RF Tomography, the

minimum norm solution to is usually affected by a lot of noise, because of the ill-conditioning of the problem. Therefore it can be a good idea to stop before this point is reached, and observe the quality of the reconstruction as the CG algorithm proceeds along its path.

These considerations provide motivation for applying the Conjugate Gradient method to RF Tomography, by applying some modifications to the basic algorithm.

4.3.1 Physical bounds, re-orthogonalization and termination

In RF Tomography the contrast function is the difference between the permittivity of the target and the permittivity of the background. Both quantities are in general complex, with the imaginary part depending on the conductivity σ. Therefore:

$$v(\mathbf{r}') = \left[\varepsilon(\mathbf{r}') - \varepsilon_b\right] - j\left[\frac{\sigma(\mathbf{r}') - \sigma_b}{2\pi f \varepsilon_0}\right], \tag{4.1}$$

for each pixel, where $\mathbf{r}'$ identifies each pixel. In free space it is assumed that:

$$\varepsilon(\mathbf{r}') \geq \varepsilon_b \tag{4.2}$$

$$\sigma(\mathbf{r}') \geq \sigma_b, \tag{4.3}$$

i.e. the target is denser and more conductive than free space. Therefore $\mathbf{v}$ will have positive real part and negative imaginary part. Unless enforced explicitly, nothing guarantees that

this simple physical rule will be respected by the CG inversion. Therefore the CG algorithm has been modified by imposing *hard* constraints on the solution returned. At every iteration:

$$\text{if} \quad \mathrm{Re}(\mathbf{v}) < 0 \quad \Rightarrow \quad \mathrm{Re}(\mathbf{v}) = |\,\mathrm{Re}(\mathbf{v}| \tag{4.4}$$

$$\text{if} \quad \mathrm{Im}(\mathbf{v}) > 0 \quad \Rightarrow \quad \mathrm{Im}(\mathbf{v}) = -|\,\mathrm{Im}(\mathbf{v})|, \tag{4.5}$$

which imposes the physical bound without changing the norm of the solution (as it would setting the pixel equal to zero). Still, this hard constraint has an important effect on the algorithm. Even though the norm of the solution remains unchanged, the solution is indeed changed, and so is its corresponding residual. In practice a jump is introduced in the solution space. This is undesired because it disrupts the natural convergence path that CG would take. In particular, CG is based on the property that at each iteration the residual vector is perpendicular to *every* residual found in the previous iterations. Since the residuals are used at every iteration to determine the next search direction, this operation disrupts CG.

The solution to this problem comes by operating a re-orthogonalization procedure (72; 73), using the Gram-Schmidt procedure (74; 75). Given a set of vectors, the Gram-Schmidt process generates a set of orthogonal vectors, in an iterative fashion. The first vector is taken as is, the second vector is made perpendicular to the first one, and so on, until all the vectors in the set have been made perpendicular to each other. In the CG inversion developed here, the quantity made orthogonal is the set of residuals $r = ||\mathbf{E}^{\mathrm{s}} - \mathbf{L} \cdot \mathbf{v}||$.

Therefore, at each iteration, after the new solution has been found and the physical bounds have been applied, the Gram-Schmidt procedure is applied to re-orthogonalize the residuals.

The last step in the algorithm is its termination. The algorithm must be stopped before it completes all the iterations, otherwise there would be no regularization effect on the solution. In order to establish the point when to stop, the evolution of the residual at every iteration is analyzed. The residual at the i-th iteration is defined as:

$$r^{(i)} = ||\mathbf{E}^{\mathrm{s}} - \mathbf{L} \cdot \mathbf{v}^{(i)}||_2. \tag{4.6}$$

This residual is analyzed in more details in the next section. Generally, $r^{(i)}$ changes rapidly with the first few iterations and then tends to stabilize toward an asymptote. Therefore a stopping condition can be applied on the derivative (finite-difference) of the residual. At every iteration the difference between $r^{(i)}$ and $r^{(i-1)}$ is computed. The algorithm continues until the difference at a step i is smaller than 5% of the maximum difference observed during the process. This procedure results in a stopping point reached very quickly, normally within 10 iterations.

4.3.2 Comparison of CG and TSVD

Conjugate Gradient and the Truncated Singular Value Decomposition have been compared using data coming from both real measurements and noise-free simulations. The conditions used in the experiments are replicated in the commercial software FEKO, which

produces as a result a vector containing the scattered field E^s. This field is in turn used to generate images.

The choice of a Method of Moments simulation provides certain advantages over other types of simulations. First, since it is a method based on the surface equivalence theorem, it allows to obtain the scattered field directly, with one simulation. A method like Finite Difference Time Domain (FDTD) would require two simulations, one with the object and one without, to obtain the scattered field by subtraction. Second, the method requires to mesh only the object that causes scattering, again thanks to the surface equivalence theorem. This represents another computational advantage against FDTD and the Finite Elements Method (FEM), because both would require to mesh the whole space where the measurement occur. Since the targets are small compared to the area where the measurement is performed, the computational advantage given by meshing only the target is very large.

Generating images using the simulated scattered electric field allows drawing conclusions on the quality of the inversion algorithm itself, without the interference of noise, positioning errors, measurement errors, etc. Nonetheless, showing the imaging results from actual measured data remains the main goal of this chapter.

First, the performance of CG in its basic formulation, without any modification is analyzed. The test conditions are the same as in Section 4.1.

Figure 11 shows the result. TSVD and CG return almost identical images. Therefore, CG has regularizing properties identical to TSVD, which come at a much lower computational cost. On a desktop PC equipped with a quad-core CPU operating at 3.7 GHz, 8 GB

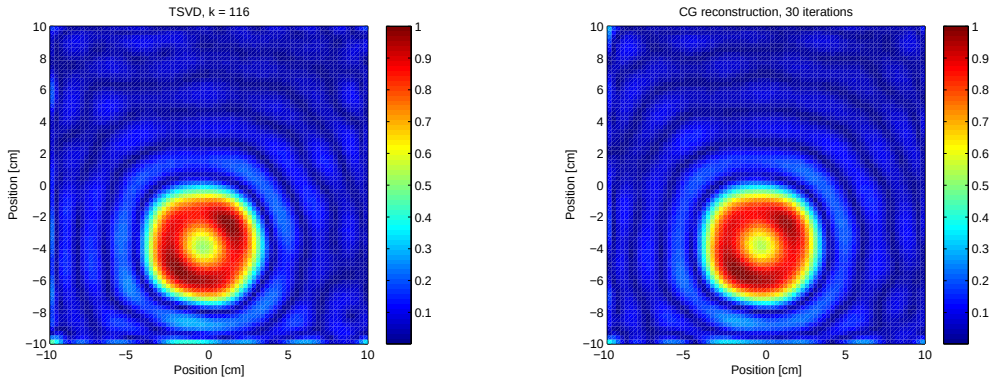

(a) (b)

Figure 11. Reconstruction of an empty PVC pipe from simulated data using TSVD (a) and CG (b). For TSVD, 116 singular values have been retained. For CG, the result is obtained after 30 iterations.

of memory, running a MATLAB code (hence, not compiled) TSVD required 4.1 seconds to find the solution, CG required less than 0.2 seconds.

For this test, CG has been forced to run for 30 iterations, overriding the automatic termination rule. This has been done to show the behavior of the residual and of the solution norm, which are displayed in Figure 12. The residual quickly decreases then it stabilizes, while the solution norm quickly increases then it stabilizes. This behavior can be observed in basically all cases, and it is what motivated the choice of the introduction of the stopping rule for the CG algorithm.

Similar results are obtained for measured data, in Figure 13. The result for TSVD is a replica of the one shown in Figure 6, while the one for CG is obtained by introducing the stopping condition. Again, the two images are extremely similar in terms of quality,

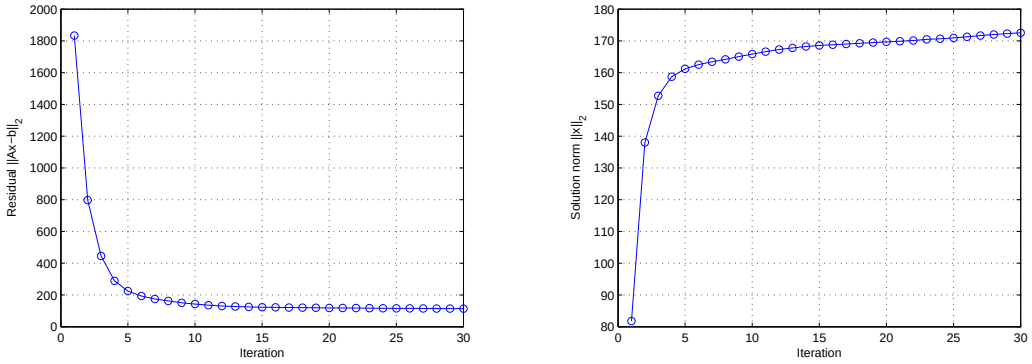

(a) (b)

Figure 12. Plots of residual (a) and solution norm (b) for CG, for simulated data. The plots show that convergence is obtained very quickly: after 10 iterations the change on both quantities is small.

with TSVD taking 4.1 seconds to find the solution and CG requiring only 0.04 seconds. CG found the solution after only 5 iterations.

4.3.3 Effect of the physical bound

The introduction of the physical bounds has beneficial effects on the quality of the solution returned by CG. Apart from the obvious advantage of avoiding solutions that do not make physical sense, restricting the space where a valid solution can be searched for has the consequence of reducing the noise present in the image. To verify this, data coming from measurements only is studied, since they are more affected by noise. The effect of the introduction of the physical bound is shown in Figure 14.

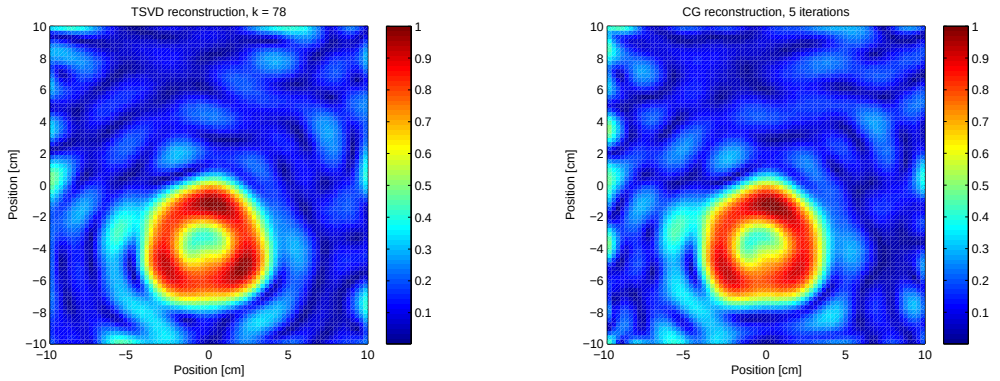

(a) (b)

Figure 13. Reconstruction of an empty PVC pipe from measured data using TSVD (a) and CG (b). For TSVD, 78 singular values have been retained. For CG, the result is obtained after only 5 iterations.

The enforcement of the physical bounds has two effects. On one hand, the image quality gets worse: the shape is not reconstructed correctly and it is hard to infer the shape of the target. On the other hand, the noise which affected Figure 13 is greatly reduced.

As explained previously, the enforcement of the *hard* physical bounds has the undesirable effect of interfering with the progression of the algorithm, because it breaks the property of orthogonality of the residual. Evidence of this is shown in the residual and solution norm plots, which become irregular, as shown in Figure 15. While the norm of the solution remains fairly stable, the norm of the residuals shows a staggering pattern. As a consequence, while the solution could be found in 5 iterations the termination condition is now met only after 21 iterations.

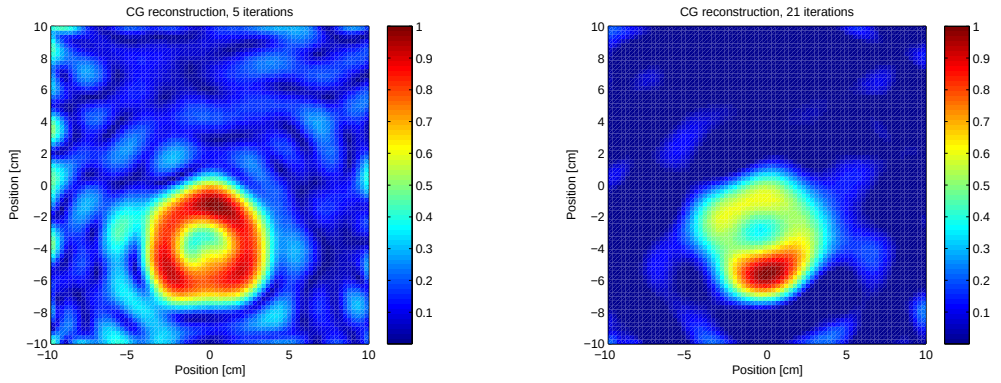

(a) (b)

Figure 14. Comparison between the regular CG algorithm (a) and the same algorithm with the enforcement of physical bounds (b). The image loses quality, but it is also much less noisy. Reorthogonalization can be used to improve the reconstruction.

These issues are solved with the application of the Gram-Schmidt re-orthogonalization procedure.

4.3.4 Effect of re-orthogonalization

Since the simple introduction of the physical bound has been shown to make the image quality worse (although it reduces the noise), a re-orthogonalization technique is used. Before computing the next solution, the residuals are re-orthogonalized, following the Gram-Schmidt process. As a result, the CG algorithm will return a solution which is computed on the basis of a set of orthogonal residual vectors. The benefit of this operation is easy to appreciate.

Figure 16 shows that the image returned is less affected by artifacts than the one of Figure 13b, and the reconstruction of the shape is slightly more accurate. The residuals

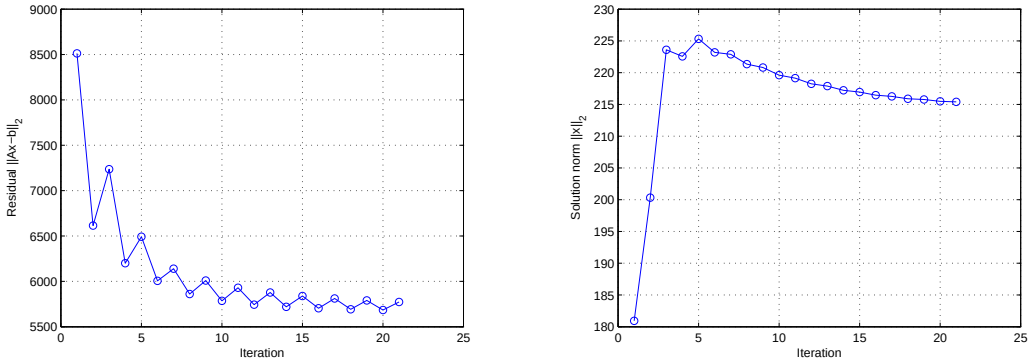

(a) (b)

Figure 15. Residual (a) and solution norm (b) as functions of the iteration step. As expected, the residuals are very irregular, because of the introduction of the physical bound.

are stable again. In fact, if the iterations continued past this point, the solution would not change at all. The enforcement of the physical bound with the addition of the re-orthogonalization step effectively restricts the space where the solution can be searched for. When the CG algorithm hits the bounds, no better solution can be found and the algorithm stops. This happens after only 0.04 seconds.

As a conclusion, this algorithm is proposed as an alternative to TSVD: it shows similar regularizing properties, it can achieve similar or better quality of the reconstructed image, it limits the noise, and it greatly reduces the computational resources needed to find a solution. Results obtained using this methods were presented in (36; 39; 42).

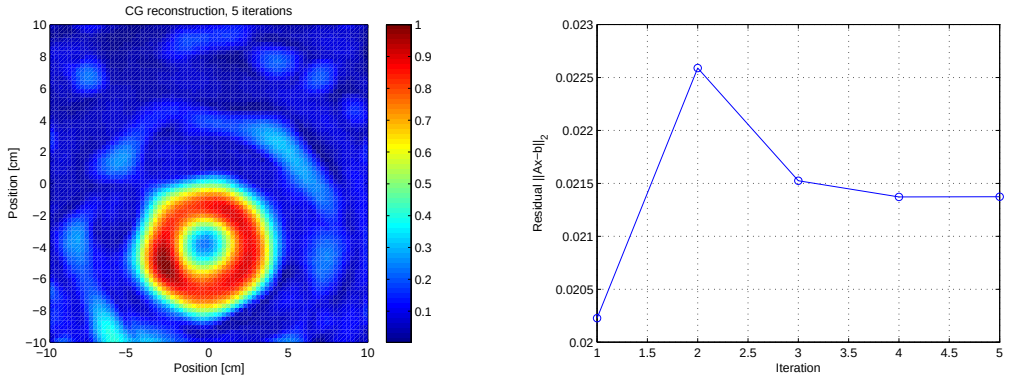

(a) (b)

Figure 16. Solution obtained using CG, enforcing the physical bounds and reorthogonalizing the residuals (a). Convergence is achieved in 5 iterations. Figure (b) shows the corresponding residual at every iteration. ©2013 IEEE, figure (a) from (42)

4.4 Algebraic Reconstruction Technique

The result obtained with CG is an improvement with respect to TSVD mostly in terms of computational resources needed and of noise reduction. However, the overall quality of the image is still affected by poor resolution. Two main factors cause this: first the Born approximation, which was used to derive the forward model in the first place (76), then CG, which is used to invert the data, operate like a low-pass spatial filter (77). Rapid transitions, such as the ones presented by the edges of the PVC object analyzed here, cannot be reconstructed exactly. The limitations given by the Born approximation are described in details in Chapter 6 where a partial solution is also proposed. In this chapter, instead, attention is given to what can be done from the inversion point of view, remaining under the umbrella of the Born approximation. An additional inversion algorithm, alternative to CG, is therefore proposed.

The Algebraic Reconstruction Technique (ART) has been developed in 1937. The original algorithm was devised by Polish mathematician Stefan Kaczmarz (78) to solve linear systems of equations[1]. Like most numerical methods developed before the 60s, it found little application simply because of the lack of powerful computers. In the 70s the method has been re-discovered and used in the field of x-ray tomography (79).

The reason why the ART method has been looked into is because it is employed in biomedical imaging, where it has been shown to be superior in some cases to the filtered

---

[1] an English translation of the original German paper is available at: `http://jasonstockmann.com/Jason_Stockmann/Welcome_files/kaczmarz_english_translation_1937.pdf`

backprojection method (80). In biomedical imaging the variability of the properties of tissue is larger than what is expected in RF Tomography, therefore it is expected that the algorithm can produce good results. In addition, the ART method does not rely on any strong mathematical assumption, but can be applied in principle to any linear system of equations. Considerations about its performance in terms of speed of convergence or other possible computational advantages are not of immediate concern. However, it is important that the algorithm is iterative, which allows to easily introduce physical bounds on the solution returned and to also easily introduce a regularization parameter.

The ART method is based in principle on the pseudo-inverse (see section 2.2). The fundamental difference is that the principle of pseudo-inverse is applied in a double-iterative fashion. In the first, inner iteration, the rows of the matrix $\mathbf{L}$ are scanned one by one to produce an image, starting from a guess solution. In the second, outer iteration, the image is used as the starting point to repeat the inner iteration. The inner iteration is run as many times as the number of rows, the outer iteration is stopped after a certain criterion is met, so as to achieve a regularizing effect, controlled by the number of iterations.

The advantage of ART over pseudo-inverse is twofold. First and foremost, the possibility to obtain a regularized solution. Second, and not less important, is the fact that the inner iteration requires a computational effort that is much smaller than the one needed by the pseudo-inverse, although in practice it realizes the same function.

In detail, ART works as follows. The original pseudo-inverse formulation (see Equation 2.5) is changed so as to operate on one row of the matrix at a time:

$$\mathbf{L}_i^{\dagger,\mathrm{ART}} = \mathbf{L}_i^H \left(\mathbf{L}_i \mathbf{L}_i^H\right)^{-1} \tag{4.7}$$

$$= \mathbf{L}_i^H \left(||\mathbf{L}_i||_2^2\right)^{-1} \tag{4.8}$$

$$= \frac{\mathbf{L}_i^H}{||\mathbf{L}_i||_2^2}, \tag{4.9}$$

where i identifies the i-th row being scanned. Notice that the inverse operation in Equation 4.7 is not a matrix operation, hence it does not involve anymore a very large, complex-valued matrix, but it is simply the reciprocal of a real positive scalar, resulting in a computational advantage.

The row-wise inverse obtained in Equation 4.9 is then used in the outer iteration to compute the solution to the inverse problem. Starting from a guess solution $\mathbf{v}_{old}$ (usually an empty vector), the algorithm computes:

$$\mathbf{v}_{new} = \mathbf{v}_{old} + \frac{\mathbf{L}_i^H}{||\mathbf{L}_i||_2^2} \left(E_i - \mathbf{L}_i \cdot \mathbf{v}_{old}\right) \tag{4.10}$$

To terminate the algorithm, the same procedure used for CG is adopted. At every iteration, the residual $r = ||\mathbf{E}^S - \mathbf{L} \cdot \mathbf{v}||$ is computed. The evolution of the residual over time is observed, and when the variation of the residual is less than 5% of the maximum variation observed, the solution is considered sufficiently stable, and the algorithm is terminated.

The result of this simple algorithm is not very good, as shown in Figure 17. In its original formulation, which is so similar to the pseudo-inverse, ART does not tackle the ill-conditioning. The reconstruction result is very similar to what is obtained in TSVD when too many singular values are retained (compare Figure 17 with Figure 7). In addition, convergence is very slow. After 30 iterations the residual still does not fall below the 5% threshold, so the algorithm is manually stopped.

Two techniques can be used to solve this problem.

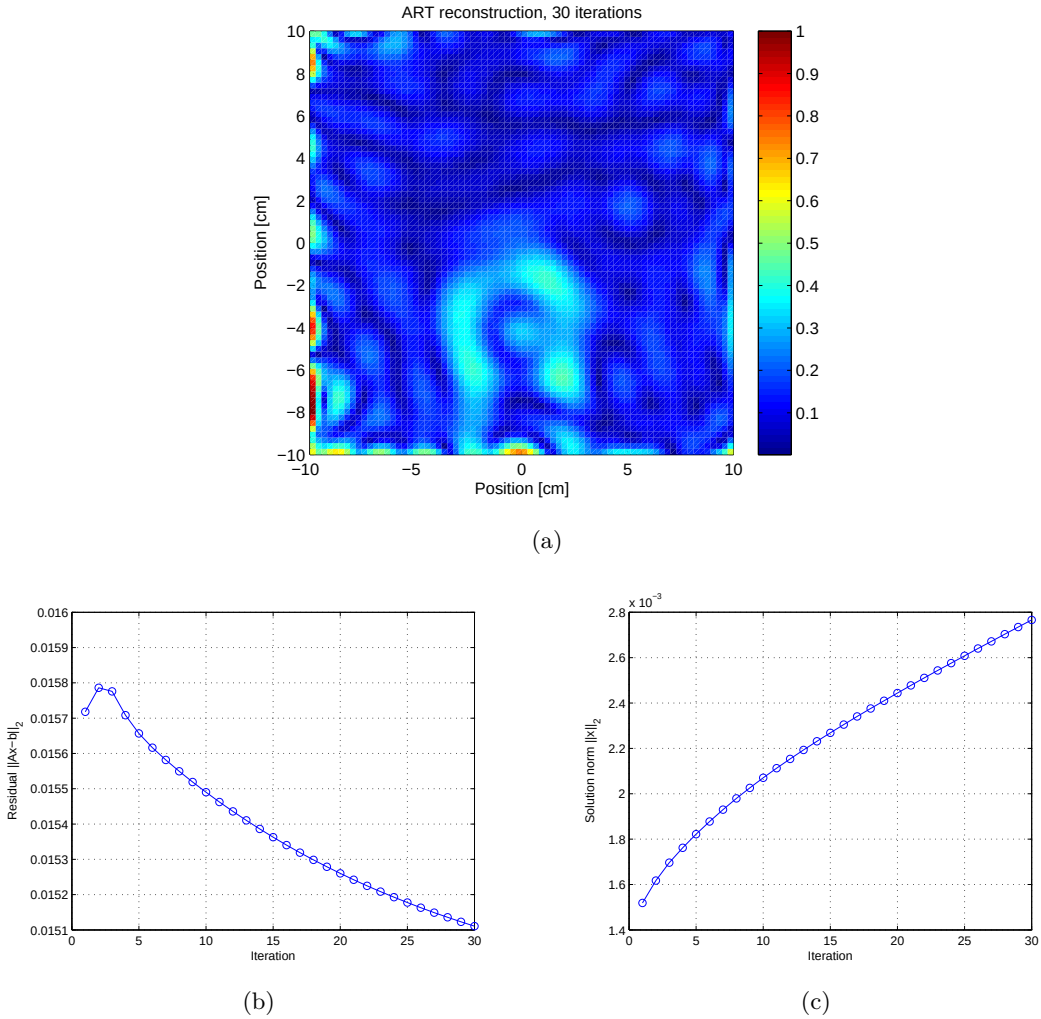

(a)

(b)

(c)

Figure 17. Solution obtained using the basic ART method (a), and corresponding plots of residual (b) and solution norm (c).

4.4.1 Physical bounds and convergence

ART can be modified like CG to include physical bounds in the solution. The procedure applied is the same, i.e. the solution computed at each iteration is forced to have positive real and negative imaginary parts. However, unlike Conjugate Gradient, ART is not based on the orthogonality of the residuals. In CG the next iteration is computed based on the assumption that the next residual must be orthogonal to all the previous residuals. ART is a simpler method: even though it uses the residual to compute the next solution, there is no explicit assumption on the nature of these residuals.

The sole application of the physical bound has incredibly positive effects on the quality of the solution. Figure 18 shows the result.

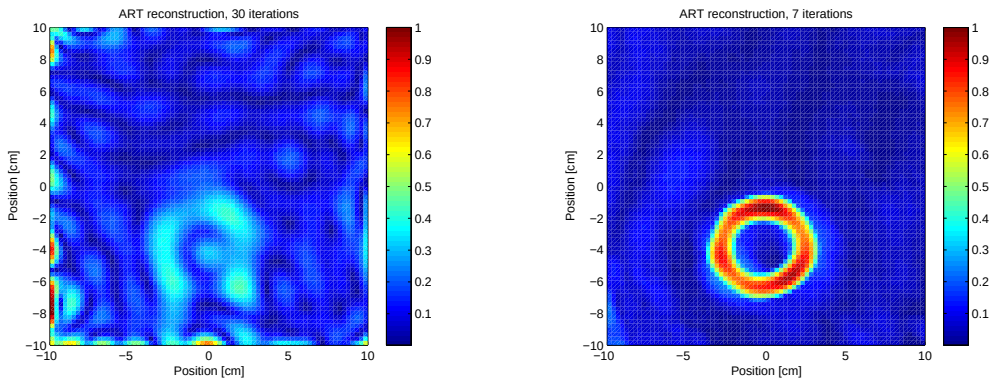

(a) (b)

Figure 18. Solution obtained using ART (a), and solution obtained using ART and enforcing the physical bounds (b). ©2012 IEEE, figure (b) from (37)

The reconstructed image is sharper, more detailed, noise-free, overall more actionable, and is obtained in a shorter time. While the original ART algorithm after 30 iterations still does not converge, after applying the physical bounds the solution is found in 7 steps.

Overall, this method required 0.36 seconds to converge (compared to 4.1 for TSVD and 0.04 for CG), making it still a very fast method. From a computational point of view ART is limited by the fact that it nests two iterations: the inner iteration scans all the rows of **L** as in Equation 4.9, while the outer iteration updates the solution based on the previous solution (Equation 4.10). The inner iteration always runs for as many steps as the number of rows in the matrix, i.e. the number of TX multiplied by the number of RX, in this case 220. The outer iteration is the one that is controlled and stopped upon request (convergence or maximum number of iterations reached). Therefore ART is inherently slower than CG. However, the reconstruction result is by far superior.

The second technique used to improve ART is not needed in all situations. In some cases, often when imaging metallic targets, the solution returned is greatly disturbed by noise.

Equation 4.10 consists of the summation of two terms: the first one is the solution found at the previous iteration, and the second one is an update term which depends on the residual and on the pseudo-inverse term. Instead of summing the two terms directly,

the update term is pre-multiplied by a constant μ. As a result, Equation 4.10 is changed as:

$$\mathbf{v}_{new} = \mathbf{v}_{old} + \mu \frac{\mathbf{L}_i^H}{||\mathbf{L}_i||_2^2} \left(E_i - \mathbf{L}_i \cdot \mathbf{v}_{old}\right) \tag{4.11}$$

The effect of μ is to operate as a regularizing parameter. Small values of μ return smoother solutions (like small values of k do with TSVD), while larger values of μ provide sharper images, but they also introduce noise (as large values of k do with TSVD). Also, small values of μ could make the algorithm converge more slowly, since the solution would be updated by very small amounts at each step. The effect of μ on the usual empty PVC pipe image is shown in Figure 19.

When μ is too large, the solution becomes noisy. However, the solution is also sharper. Therefore, μ should be chosen to be as large as possible before convergence is disrupted (as is the case in Figure 19d).

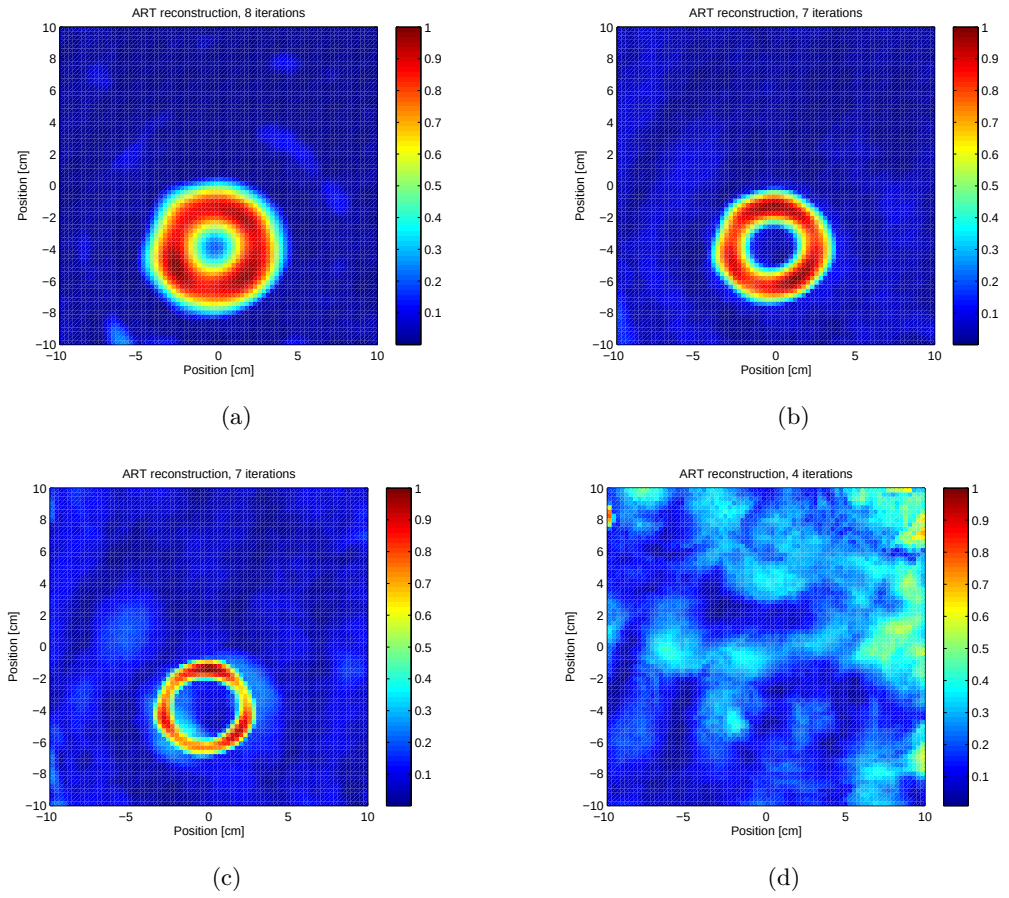

(a) (b) (c) (d)

Figure 19. Reconstruction using ART and enforcing the physical bounds, with $\mu = 0.1$ (a), $\mu = 0.5$ (b), $\mu = 1.5$ (c), and $\mu = 2$ (d). Images are obtained after 8, 7, 7 and 4 iterations, respectively.

4.5 Imaging results: detection of metallic and dielectric targets

A particular feature offered by RF Tomography is the ability to distinguish between metallic and dielectric targets. This possibility is interesting because it can provide additional information, not limited to the shape and location of the target. In many settings, the possibility to tell apart metals and non-metals could make the difference between succeeding or failing in identifying buried targets of interest.

Since the contrast vector $\mathbf{v}$ is complex-valued, separating its real and imaginary components allows to obtain independent images of conducting and insulating objects. This is also enforced by the physical bounds applied to the solution in the iterative methods.

The test used as example has been carried out using 11 transmitters rotating around a circle of radius equal to 38.4 cm and 20 receivers whose radius of rotation was 15.4 cm. Two targets are present in the area under investigation. The first target is a copper cylinder, of diameter 1.8 cm and 2.8 cm tall. The cylinder is hollow and its thickness is equal to 1 mm. The second target is a plastic cylinder (PVC, $\varepsilon_r \approx 2.5$ at 3 GHz), with diameter 7 cm and height 4.3 cm. This cylinder is also hollow, with its side having a thickness of 5 mm. The copper cylinder is located inside the PVC pipe, in a non-concentric position. The geometry is shown in Figure 20.

The first attempt of reconstruction is made with TSVD and the result is presented in Figure 21. The absolute part of the image is due for the most part to the copper cylinder, which represents a stronger scatterer with respect to the PVC pipe. By separating real and imaginary parts this becomes evident. The images are fairly noisy, and, since no physical

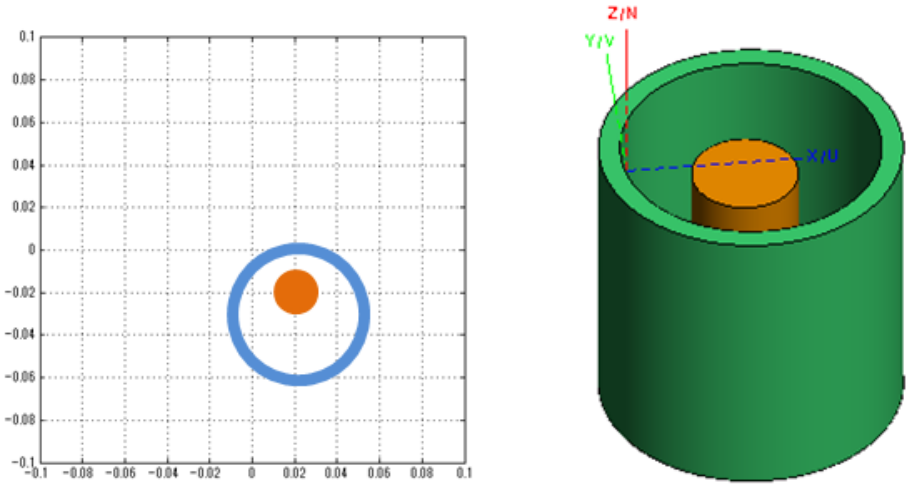

Figure 20. Geometry for the test case.

bounds have been enforced, parts of $\mathrm{Re}(\mathbf{v})$ are negative, while parts of $\mathrm{Im}(\mathbf{v})$ are positive. The image has been partitioned into 101×101 pixels, so that reconstruction is performed in 14.9 seconds. Inversion is performed only once, the real and imaginary parts are extracted from the complex vector resulting from the inversion. The number of singular values to be retained in the inversion is automatically determined by the location of the corner in the L-curve.

The second reconstruction attempt is made with CG without the introduction of any physical bound, and is shown in Figure 22. The quality of the reconstruction is very similar to the one of TSVD, as expected. The advantage is in terms of computational burden, since the inversion requires only 5 iterations to converge, taking 0.08 seconds (about 190 times faster than TSVD).

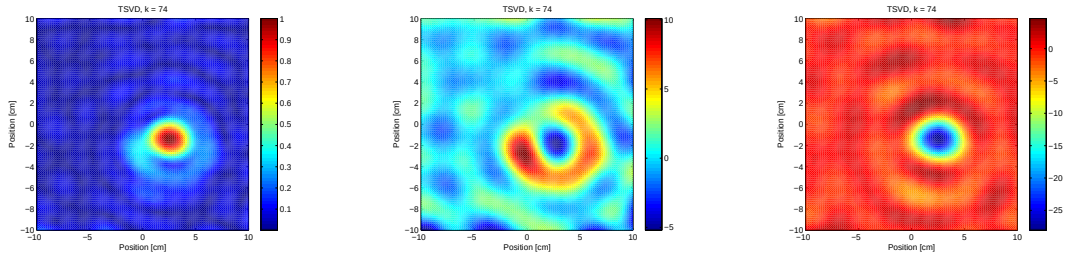

(a) (b) (c)

Figure 21. Reconstruction of a metallic and plastic objects using TSVD. Images are obtained using 74 singular values. Figure (a) shows the absolute value of the contrast vector and is normalized, (b) and (c) show the real and imaginary parts, respectively, and have not been normalized.

The result of Figure 22 can be improved by applying physical bounds to the CG inversion. The result is shown in Figure 23. The reconstruction improves visibly. The sole application of the physical bounds improves the reconstruction of the real part in particular. The shape of the PVC pipe appears now more round and defined, and the images are overall more sharp, due to a reduction of the noise level. The time required to obtain these images is 0.09 seconds, still corresponding to 5 iterations. The application of the physical bound provides no computational burden, and the re-orthogonalization using the Gram-Schmidt technique proves to be extremely quick.

Next, the performance of ART is analyzed. Figure 24 shows the reconstruction produced by the Algebraic Reconstruction Technique without any modification. Quality is comparable to the ones of Figure 21 and Figure 22. The image is obtained in 0.53 seconds, or 8 iterations. The image has been obtained with $\mu = 0.5$, chosen empirically. The problems

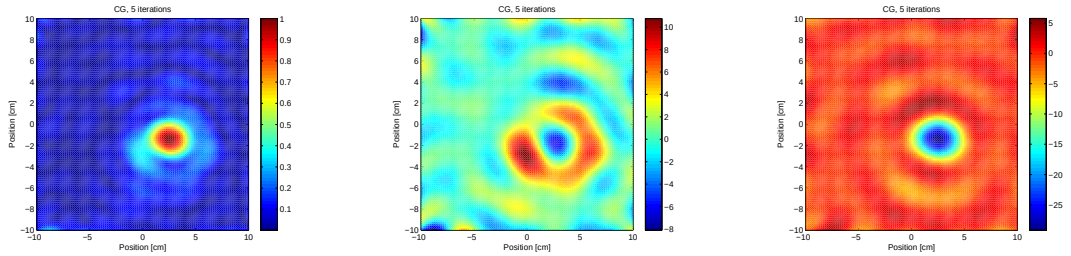

(a) (b) (c)

Figure 22. Reconstruction of a metallic and plastic objects using Conjugate Gradient without enforcing any physical bound.

in the reconstruction are the same as CG and TSVD: the images are noisy, both real and imaginary parts show positive and negative values, and in general it is difficult to distinguish the PVC pipe.

The best result is obtained when the physical bound is applied to ART, as shown in Figure 25. The absolute value is still dominated by the copper cylinder, which represents a strong scatterer. However, both real and imaginary parts of the contrast vector show very little noise, and the real part depicts more clearly the PVC pipe. The images in Figure 25 have been obtained again with $\mu = 0.5$; the application of the physical bounds makes the algorithm converge after 8 iterations instead of 7, taking a total of 0.55 seconds.

Comparing Figure 25 against Figure 23 and Figure 21 it is obvious the big advantage of ART over CG and TSVD. Even though ART is slower than CG, due to the nested iterations, it is still almost 30 times faster than TSVD.

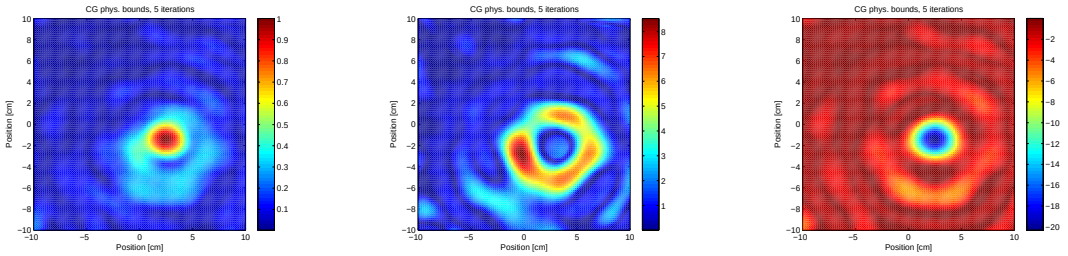

(a) (b) (c)

Figure 23. Reconstruction of a metallic and plastic objects using Conjugate Gradient modified with the introduction of the physical bounds and the reorthogonalization algorithm. Figure (a) shows the absolute value of the contrast vector and is normalized, (b) and (c) show the real and imaginary parts, respectively, and have not been normalized.

Overall, ART, with the addition of the physical bounds and the use of the regularizing parameter μ proves to be a very good inversion algorithm that allows to overcome some of the resolution limitations given by CG; it is therefore proposed as an alternative inversion method.

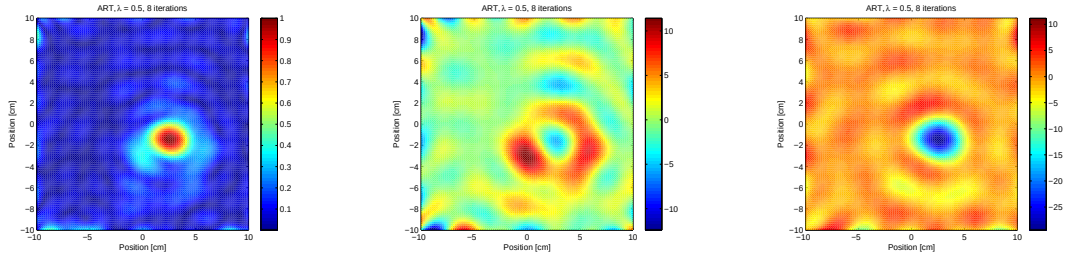

(a) (b) (c)

Figure 24. Reconstruction of a metallic and plastic objects using ART. Figure (a) shows the absolute value of the contrast vector and is normalized, (b) and (c) show the real and imaginary parts, respectively, and have not been normalized.

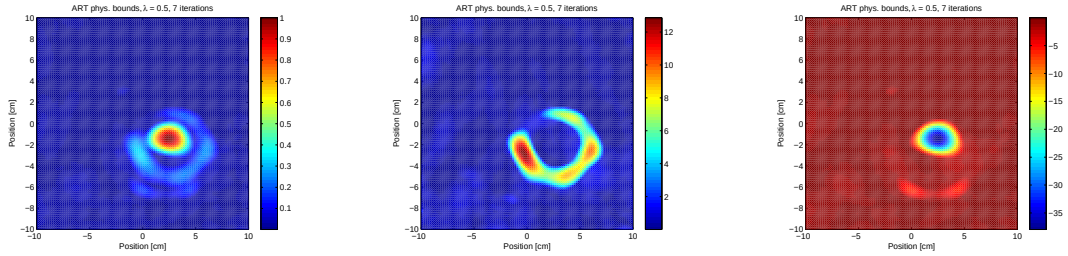

(a) (b) (c)

Figure 25. Reconstruction of a metallic and plastic objects using ART modified with the introduction of the physical bounds. Figure (a) shows the absolute value of the contrast vector and is normalized, (b) and (c) show the real and imaginary parts, respectively, and have not been normalized.

CHAPTER 5

A DYADIC CONTRAST FUNCTION FOR RF TOMOGRAPHY

This chapter introduces a dyadic contrast function in the RF Tomography forward model by applying it to the scattering from thin elongated objects, and describes how there exists a fundamental difference between the scattering originated by metallic versus non-metallic targets. The dyadic contrast function thus introduced allows extracting information previously unavailable without changing the way data are collected. Because of this, it can theoretically be applied to data already available.

As explained in the introduction, RF Tomography generates images of the contrast function, i.e. the difference between the dielectric permittivity constant of the background medium and the one of the target. The space is partitioned in voxels (or pixels) and each one is assigned a (complex) scalar numerical value. An image is obtained by mapping these values to a color scale. The information returned is therefore scalar and the shape of the target is then inferred by simple visual inspection of the resulting image. It would be interesting to have the possibility of reconstructing the shape of an object in terms of actual 3D vectors, pointing in space in a direction corresponding to the orientation of the edges of the target. This would allow to obtain a "wire frame" model of the target, more informative than a simple color plot. Another added benefit would be that this supplemental information could augment the colored image particularly in the presence of clutter, or when limits in the system resolution do not allow to get a good idea of the shape of the target.

This chapter discusses scattering from thin, elongated objects, and describes how there exists a fundamental difference between the scattering originated by metallic versus non-metallic targets. An analytic explanation of this phenomenon can be given using a modal analysis. This finding motivates a change in the RF Tomography forward model so as to include a dyadic (second-order tensor) contrast function. This new contrast function would be able to represent preferred scattering directions and therefore orientation of objects.

Interestingly, a parallel can be drawn between this approach and Diffusion Tensor Imaging (DTI), an imaging technique based on Magnetic Resonance, used to obtain 3D maps of the structure of the brain of a subject (81; 82; 83).

5.1 De-polarization of the scattered field

Consider a canonical scattering problem, depicted in Figure 26.

A plane wave is impinging upon a cylinder of negligible radius ($r \ll \lambda$) and infinite length. The cylinder is aligned with the z axis. The incident plane wave propagates along the x axis and is linearly polarized in the zy plane, with an angle θ with respect to the z axis. The problem can be decomposed as the linear superposition of two orthogonal components: one corresponds to the part of the incident field parallel to the cylinder, the other corresponds to its perpendicular counterpart. In practice the problem is decomposed into a TM^z and a TE^z mode, which can be studied separately. In addition, the analysis is further divided into the cases of Perfect Electric Conductor (PEC) and dielectric (non-conductive) cylinder. Although this derivation is a classical EM procedure, it serves to

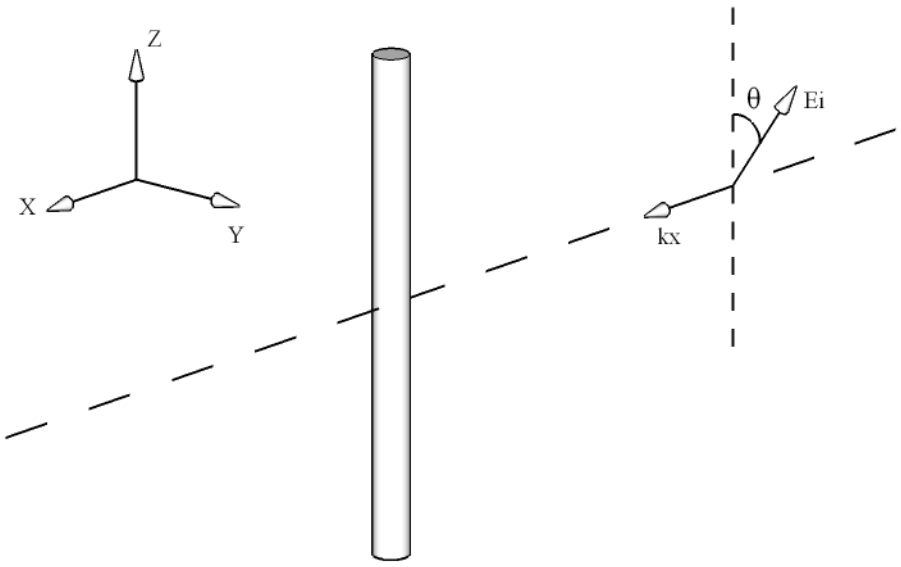

Figure 26. Coordinate system and scattering problem representation.

provide a rigorous analytical explanation for the more extensive simulation results described later on.

5.1.1 Modal analysis: thin PEC cylinder

When the cylinder is made of Perfect Electric Conductor, the analysis is based on a classical Mode Matching technique which is reported here almost in its entirety, to better understand its consequences (84; 85; 86).

TM mode

The TM mode occurs when the incident field is oriented along the z axis, traveling in the positive x direction with wave number $k = 2\pi/\lambda$. The incident field therefore is:

$$\mathbf{E}^{\mathrm{i}} = E_0 e^{-jkx} \hat{\mathbf{z}}. \tag{5.1}$$

This can be expanded in cylindrical coordinates in order to facilitate the imposition of the boundary conditions:

$$\mathbf{E}^{\mathrm{i}} = \hat{\mathbf{z}} E_0 \sum_{n=-\infty}^{+\infty} j^{-n} J_n(k\rho) e^{jn\phi}, \tag{5.2}$$

where J_n represents a Bessel function of the first kind of order n. This wave impinges upon the cylinder and generates a scattered wave. The scattered wave is assumed of the same polarization of the incident field and it travels outwards. Therefore[1]

$$\mathbf{E}^{\mathrm{s}} = \hat{\mathbf{z}} E_0 \sum_{n=-\infty}^{+\infty} c_n H_n^{(2)}(k\rho). \tag{5.3}$$

---

[1]The notation is important. Here the H with the superscript (2) indicates the Bessel function of the second kind, $H_i^{(2)}(x) = J_i(x) + jY_i(x)$ and should not be confused with the magnetic field $\mathbf{H}$.

The application of the boundary conditions on the surface of the cylinder allows to determine the value of the coefficients c_n. Since the object is made of PEC, the total tangential electric field on its surface (of radius a) must be identically zero:

$$\begin{aligned}
&\mathbf{E}^{\mathrm{t}} = \mathbf{E}^{\mathrm{i}} + \mathbf{E}^{\mathrm{s}} = 0|_{\rho=a} \\
&\quad \Rightarrow \hat{\mathbf{z}} E_0 \sum_{n=-\infty}^{+\infty} \left[j^{-n} J_n(ka) e^{jn\phi} + c_n H_n^{(2)}(ka) \right] = 0, \quad \forall \phi, z.
\end{aligned} \tag{5.4}$$

It immediately follows that:

$$c_n = -j^{-n} \frac{J_n(ka) e^{jn\phi}}{H_n^{(2)}(ka)}. \tag{5.5}$$

In conclusion:

$$\mathbf{E}^{\mathrm{s}} = \hat{\mathbf{z}} E_0 \sum_{n=-\infty}^{+\infty} -j^{-n} \frac{J_n(ka) e^{jn\phi}}{H_n^{(2)}(ka)} H_n^{(2)}(k\rho). \tag{5.6}$$

The current impressed on the surface of the cylinder by this wave can be computed by finding the total magnetic field on the surface of the cylinder first:

$$\mathbf{H}^{\mathrm{t}} = -\frac{1}{j\omega\mu_0} \nabla \times \mathbf{E}^{\mathrm{s}}. \tag{5.7}$$

Since the total electric field only has components in the z direction, the total magnetic field will have components in the ρ and ϕ directions only. However, only the tangential ϕ component will contribute to the creation of the induced current density, since:

$$\mathbf{J}_{TM} = \hat{\mathbf{n}} \times \mathbf{H}^t \tag{5.8}$$

$$= \hat{\boldsymbol{\rho}} \times (\hat{\rho} H_\rho^t + \hat{\phi} H_\phi^t) \tag{5.9}$$

$$= \hat{\boldsymbol{\rho}} \times \hat{\phi} H_\phi^t, \quad \rho = a \tag{5.10}$$

$$= \hat{\mathbf{z}} H_\phi^t, \quad \rho = a. \tag{5.11}$$

The resulting impressed current is parallel to both incident and scattered electric fields. After some algebra:

$$\mathbf{J}_{TM} = \hat{\mathbf{z}} \frac{2E_0}{a\pi\omega\mu_0} \sum_{n=-\infty}^{+\infty} j^{-n} \frac{e^{jn\phi}}{H_n^{(2)}(ka)}. \tag{5.12}$$

For a given frequency and radius of the cylinder, the magnitude of the current depends solely on the specific position around the cylinder, i.e. ϕ. In addition, if the cylinder is very small the dominant term of the summation is n equal to zero. The small radius approximation leads to:

$$\mathbf{J}_{TM} \approx \hat{\mathbf{z}} \frac{2E_0}{a\pi\omega\mu_0 H_0^{(2)}(ka)}. \tag{5.13}$$

As a result Equation 5.13 has a constant value for a given radius and frequency.

TE mode

The TE mode corresponds to the part of the incident field that is oriented along the y direction, traveling in the positive x direction with wave number $k = 2\pi/\lambda$. The derivation is very similar to the TM case, but with converse electric and magnetic fields. Briefly, the incident magnetic field is:

$$\mathbf{H}^{\mathrm{i}} = H_0 e^{-jkx}\hat{\mathbf{z}} \tag{5.14}$$

$$= \hat{z}H_0 \sum_{n=-\infty}^{+\infty} j^{-n} J_n(k\rho) e^{jn\phi}, \tag{5.15}$$

which causes a scattered magnetic field:

$$\mathbf{H}^{\mathrm{s}} = \hat{\mathbf{z}}H_0 \sum_{n=-\infty}^{+\infty} c_n H_n^{(2)}(k\rho). \tag{5.16}$$

Application of the boundary conditions to the tangential electric field (thus only E_ϕ^s component, with $\mathbf{E}^{\mathrm{s}} = \frac{1}{j\omega\varepsilon}\nabla \times \mathbf{H}^s$) leads to:

$$c_n = -j^{-n} \frac{J_n'(ka)}{H_n'^{(2)}(ka)} e^{jn\phi}, \tag{5.17}$$

with

$$J_n'(ka) = \frac{\partial J_n(k\rho)}{\partial k\rho}, \quad \rho = a \tag{5.18}$$

$$H_n'^{(2)}(ka) = \frac{\partial H_n^{(2)}(k\rho)}{\partial k\rho}, \quad \rho = a. \tag{5.19}$$

Therefore the total magnetic field on the surface of the cylinder will be:

$$\mathbf{H}^{\mathrm{t}}|_{\rho=a} = \mathbf{H}^{\mathrm{i}} + \mathbf{H}^{\mathrm{s}} \tag{5.20}$$

$$= -\hat{\mathbf{z}} j \frac{2H_0}{\pi ka} \sum_{n=-\infty}^{+\infty} j^{-n} \frac{1}{H_n^{(2)}(ka)} e^{jn\phi}. \tag{5.21}$$

Finally, the impressed current on the surface of the cylinder is:

$$\mathbf{J}_{TE} = \hat{\mathbf{n}} \times \mathbf{H}^t \tag{5.22}$$

$$= \hat{\boldsymbol{\rho}} \times \hat{z} H_z^t \tag{5.23}$$

$$= -\hat{\boldsymbol{\phi}} H_z^t, \quad \rho = a \tag{5.24}$$

$$= \hat{\boldsymbol{\phi}} \frac{2H_0}{\pi ka} \sum_{n=-\infty}^{+\infty} j^{-n} \frac{1}{H_n^{(2)}(ka)} e^{jn\phi}. \tag{5.25}$$

Unlike the TM case, Equation 5.25 has non-negligible terms when $n = -1, 0, +1$. As a result, even in the case of small radius, the impressed current will depend on the position around the cylinder, i.e. ϕ. In any case, Equation 5.25 can be rewritten as

$$\mathbf{J}_{TE} \approx \hat{\boldsymbol{\phi}} \frac{2H_0}{\pi ka} \sum_{n=-1}^{+1} j^{-n} \frac{1}{H_n^{(2)}(ka)} e^{jn\phi} \ , \tag{5.26}$$

which does not involve an infinite summation and is easier to compute.

Comparison

A direct comparison of Equation 5.13 and Equation 5.26 allows understanding that there is a significant difference between the two. From Figure 27 it is clear that the magnitude

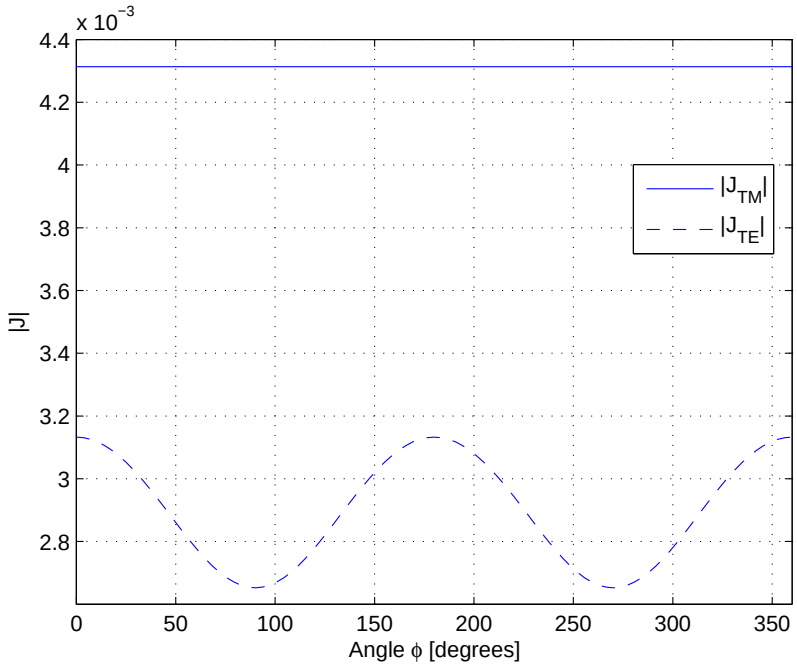

Figure 27. Comparison of the magnitude of the impressed currents for the TM and TE cases.

of the impressed current in the TM case is larger than the magnitude of the impressed current in the TE case. Therefore the TM case is dominant. In turn, this means that when the plane wave impinges on the thin cylinder at an angle with respect to the z axis, the impressed current will be mostly aligned with the thin cylinder itself. As a consequence, the scattered field will also be mostly aligned with the thin cylinder and create a *depolarization* effect.

5.1.2 Modal analysis: thin dielectric cylinder

The same procedure used for a PEC cylinder can be applied to a dielectric cylinder. Also this case is a classical EM problem, which has been studied in the past (87). The derivation follows the same principles of the previous case, but the result is much simpler.

For the TM mode the total electric field inside the cylinder is oriented in the z direction and is equal to[1]

$$\mathbf{E}^{\mathrm{t}} = \hat{\mathbf{z}} E_0 \sum_{n=-\infty}^{+\infty} a_n j^{-n} J_n(k_d \rho) e^{jn\phi}, \quad \rho \leq a, \tag{5.27}$$

where the coefficients a_n are equal to:

$$a_n = j^{-n} \frac{J_n(k_0 a) H_n'^{(2)}(k_0 a) - J_n'(k_0 a) H_n^{(2)}(k_0 a)}{J_n(k_d a) H_n'^{(2)}(k_0 a) - \sqrt{\varepsilon_r/\mu_r} J_n'(k_d a) H_n^{(2)}(k_0 a)}. \tag{5.28}$$

For the TE mode the total magnetic field is equal to

$$\mathbf{H}^{t} = \hat{\mathbf{z}} H_0 \sum_{n=-\infty}^{+\infty} b_n j^{-n} J_n(k_d \rho) e^{jn\phi}, \quad \rho \leq a, \tag{5.29}$$

where the coefficients b_n are equal to:

$$b_n = j^{-n} \frac{J_n(k_0 a) H_n'^{(2)}(k_0 a) - J_n'(k_0 a) H_n^{(2)}(k_0 a)}{J_n(k_d a) H_n'^{(2)}(k_0 a) - \sqrt{\mu_r/\varepsilon_r} J_n'(k_d a) H_n^{(2)}(k_0 a)}. \tag{5.30}$$

---

[1]Everywhere the subscript 0 indicates free space and the subscript d indicates the dielectric inside the cylinder

Comparing Equation 5.27 with Equation 5.29 and Equation 5.28 with Equation 5.30 it can be seen that they are remarkably similar. For a weak scatterer ε_r is small, so the coefficients a_n and b_n will be almost identical. Also, only the coefficients with $n = -1, 0, 1$ will have a significant magnitude for cylinders of small radius. A plot of the coefficients a_n and b_n is shown in Figure 28

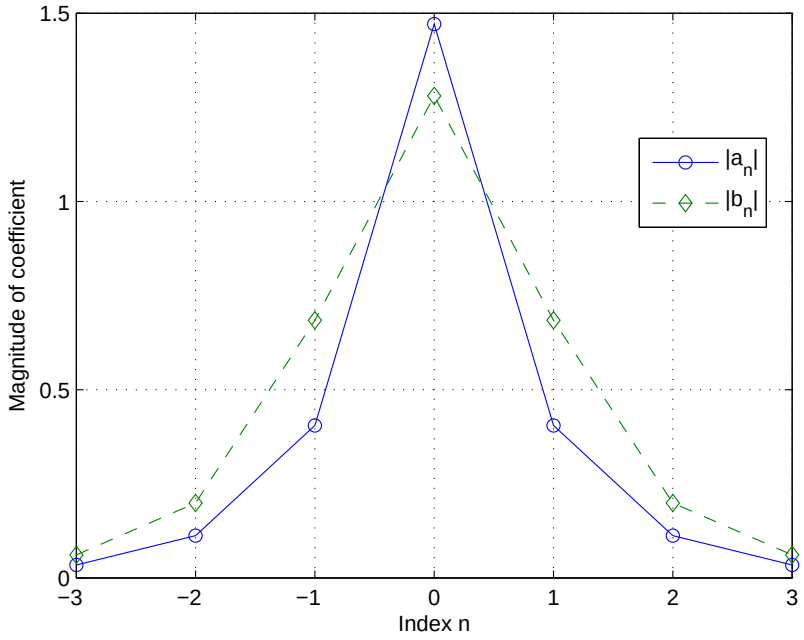

Figure 28. Magnitude of coefficients a_n and b_n of Equation 5.28 and Equation 5.30 as a function of the mode index n.

As a result, the impressed currents for the TM and TE cases will be very similar in magnitude, unlike what happened for a PEC cylinder. In the case of oblique incidence, the overall impressed current will be a combination of the TE and TM case, but since their magnitude is similar, the impressed current will have almost the same direction of the incident field. The weaker the scatterer, the more correct is this conclusion.

Therefore, it exists a fundamental difference between scattering from PEC and dielectric objects, which affects greatly the scattered field, both in magnitude and, this is the main point, in its orientation in space. These simple analytical results can be generalized to encompass a much wider variety of cases, using numerical simulations.

5.1.3 Method of Moments simulation

A Method of Moments simulation allows to analyze cases that are not as simple as the ones for which an analytic description could be derived.

First, consider a $\hat{z}$-polarized plane wave impinging upon a thin cylinder. The cylinder is located in the zy-plane and forms a 45 degrees angle with the $\hat{z}$ axis. The radius of the cylinder is equal to $\lambda/50$ and its length is equal to λ. The distribution of the currents impressed on the surface of the cylinder, for both dielectric and PEC case, is computed with a Method of Moments simulation.

Figure 29 shows the distribution of the currents on a PEC cylinder, while Figure 30 shows the distribution of the impressed currents on a dielectric cylinder with $\varepsilon_r = 5$. For the PEC case the currents are always mostly aligned with the thin cylinder, while for the dielectric case the currents are always mostly aligned with the incident field.

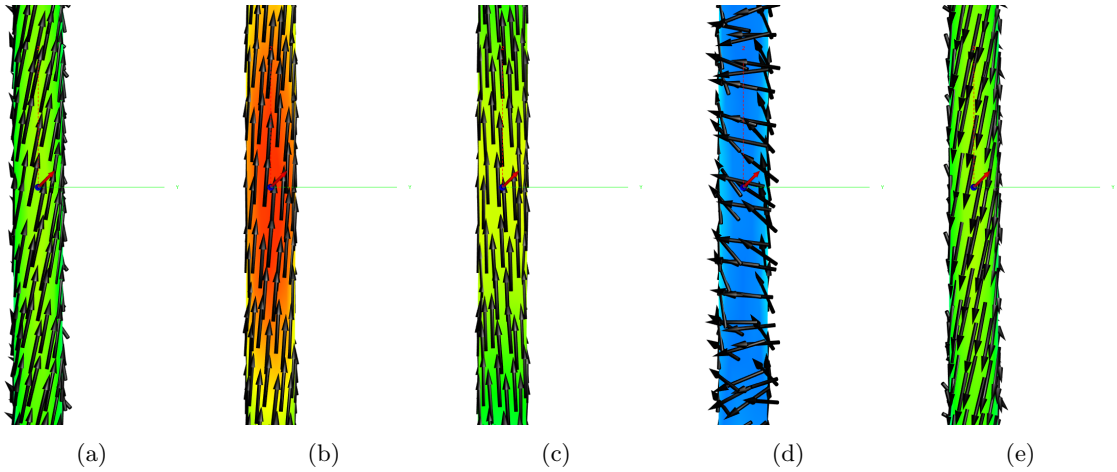

Figure 29. Impressed currents (black arrows) on a PEC cylinder of radius $\lambda/50$ and length $\lambda/2$. The incident field is impinging at a 45° angle with respect to the z axis. The figure shows the instantaneous distribution at phase ωt equal to (a) 0°, (b) 45°, (c) 90°, (d) 135° and (e) 180°.

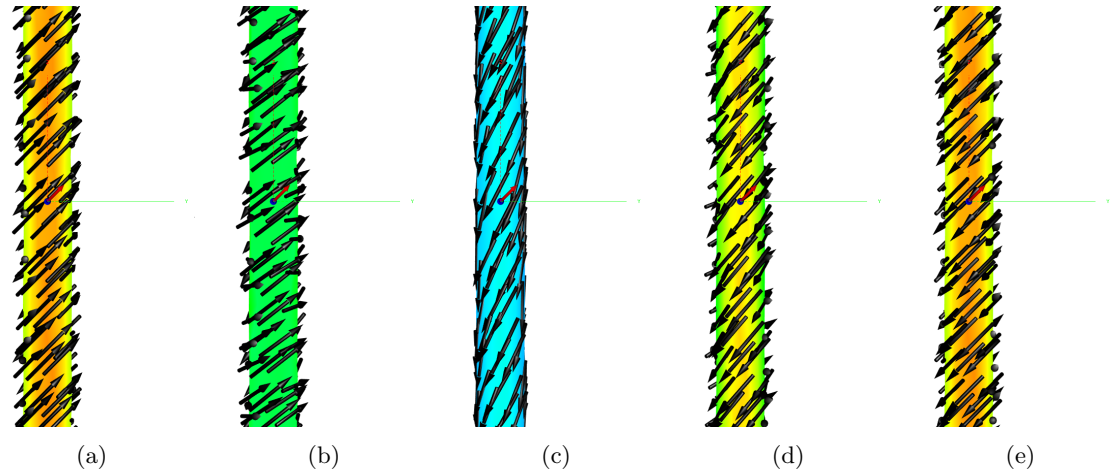

Figure 30. Impressed currents (black arrows) on a dielectric cylinder ($\varepsilon_r = 5$) of radius $\lambda/50$ and length $\lambda/2$. The incident field is impinging at a 45° angle with respect to the z axis. The figure shows the instantaneous distribution at phase ωt equal to (a) 0°, (b) 45°, (c) 90°, (d) 135° and (e) 180°.

A similar effect can be observed when plotting the far field radiation pattern of the scattered-only part of the electric field. This is shown in Figure 31. For a metallic cylinder the scattering pattern is tilted toward the main axis of the cylinder; instead, for the dielectric object the pattern is tilted toward the direction of the incident field.

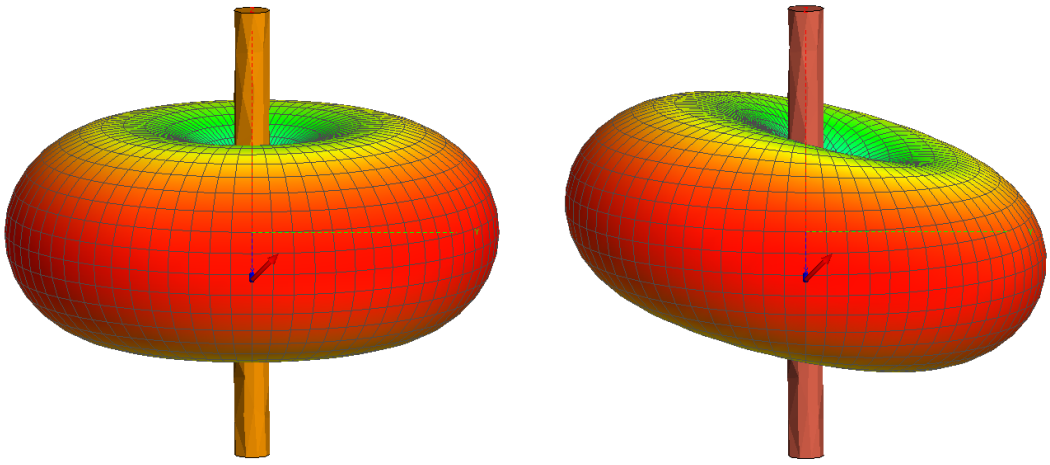

(a) (b)

Figure 31. Far field radiation pattern of the scattered only part of the electric field, for a metallic (a) and dielectric (b) cylinders placed at a 45° angle with respect to the polarization of an incident plane wave.

The same effect can be observed in the near field distribution of the scattered only part of the field, as shown in Figure 32.

Finally, it can be observed that the de-polarization effect occurs also for a generic shape composed of thin cylinders. Figure 34a shows the instantaneous currents impressed on the

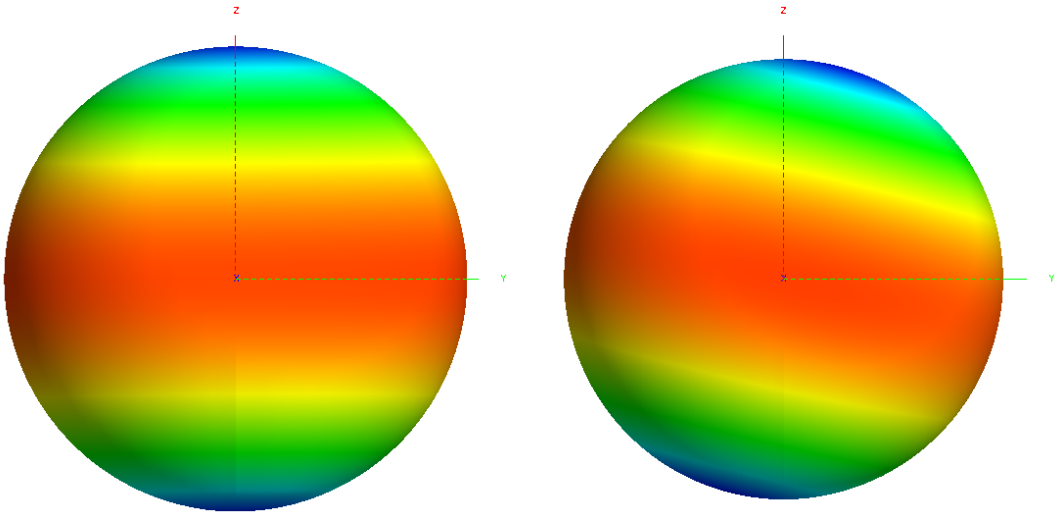

(a) (b)

Figure 32. Near field radiation pattern of scattered only part of the electric field, for a metallic (a) and dielectric (b) cylinders placed at a 45° angle with respect to the polarization of an incident plane wave, at a distance equal to one wavelength from the center of the cylinder.

structure made of PEC at time instants $\omega t = 0°$, while Figure 34b shows the currents at $\omega t = 90°$. A similar result is obtained at all other time instants. The currents are aligned with the cylinders, regardless of their orientation with respect to the incident field.

Furthermore, simulation results seem to suggest that the thin elements composing a complex structure do not interfere very much with each other, even when in close proximity. The current distributions on each thin cylinder is basically independent from the distribution on its neighbor. In the structure, the elements on top are in contact, thus currents are free

to flow: this seems to have an effect on the current distribution only in a region extremely close to the point of contact itself.

Instead, Figure 35a shows the instantaneous currents impressed on the structure made of a dielectric material ($\varepsilon_r = 5$) at time instants $\omega t = 45°$, while Figure 35b shows the currents at $\omega t = 135°$. In this case the currents are aligned with the incident field, regardless of the orientation of the pieces of the structure with respect to the incident field.

In conclusion, it is observed that there is a fundamental difference in the scattering generated by complex structures, depending on the material of which they are made of. This difference could be properly exploited in order to gain additional information on the geometrical structure of metallic objects. The information retrieved would then be integrated with the classic images returned by RF Tomography, and result in an increased situational awareness.

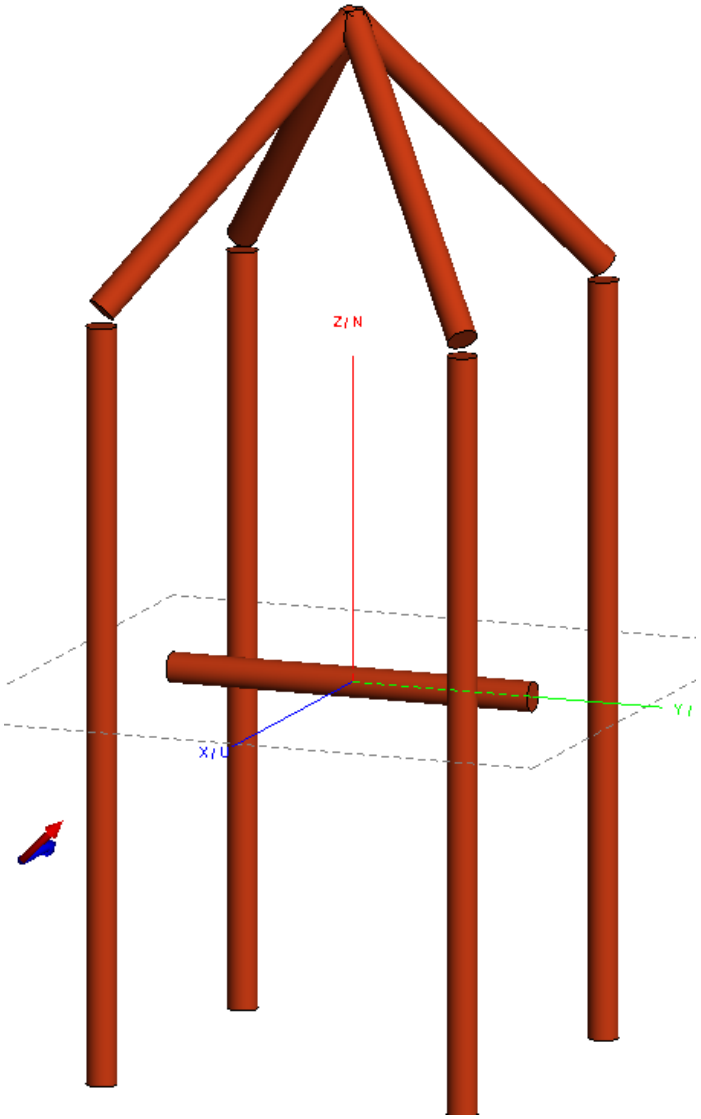

Figure 33. Geometrical shape composed of thin cylinders. The incident field is indicated by the red arrow and is impinging upon the structure at an angle of 45° with respect to the vertical z axis.

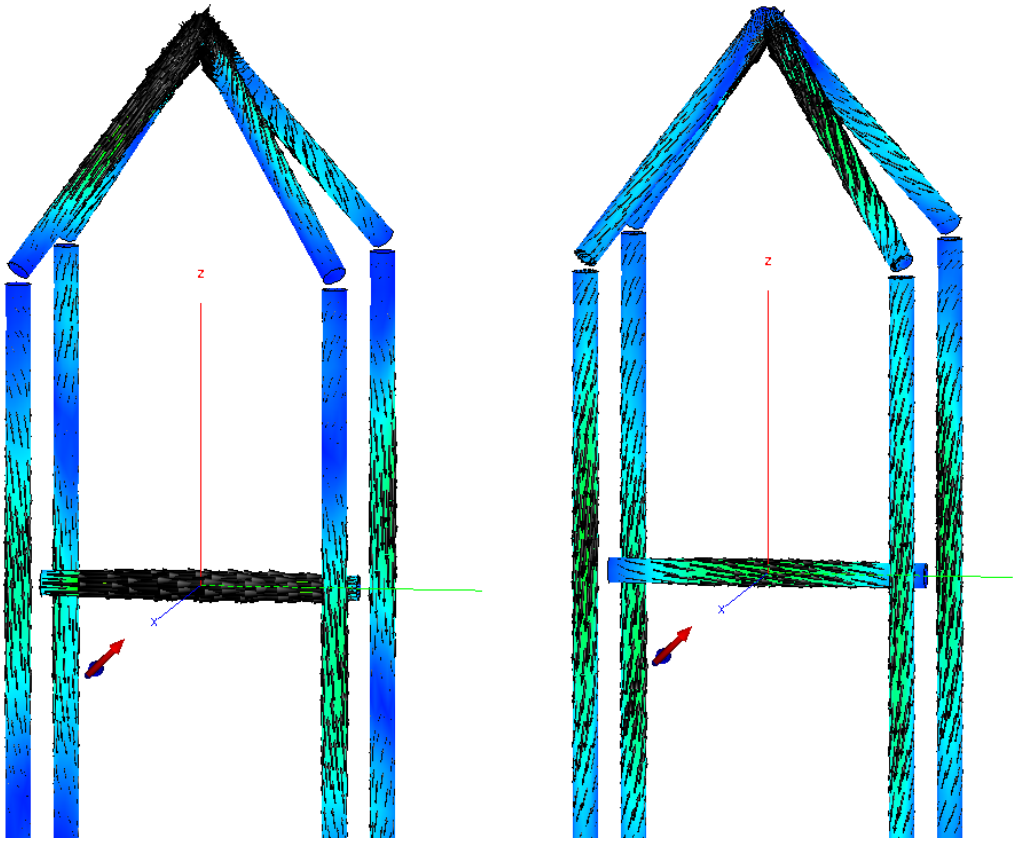

(a) (b)

Figure 34. Instantaneous impressed currents on a geometrical structure made of PEC, at $\omega t = 0°$ (a) and $\omega t = 90°$ (b).

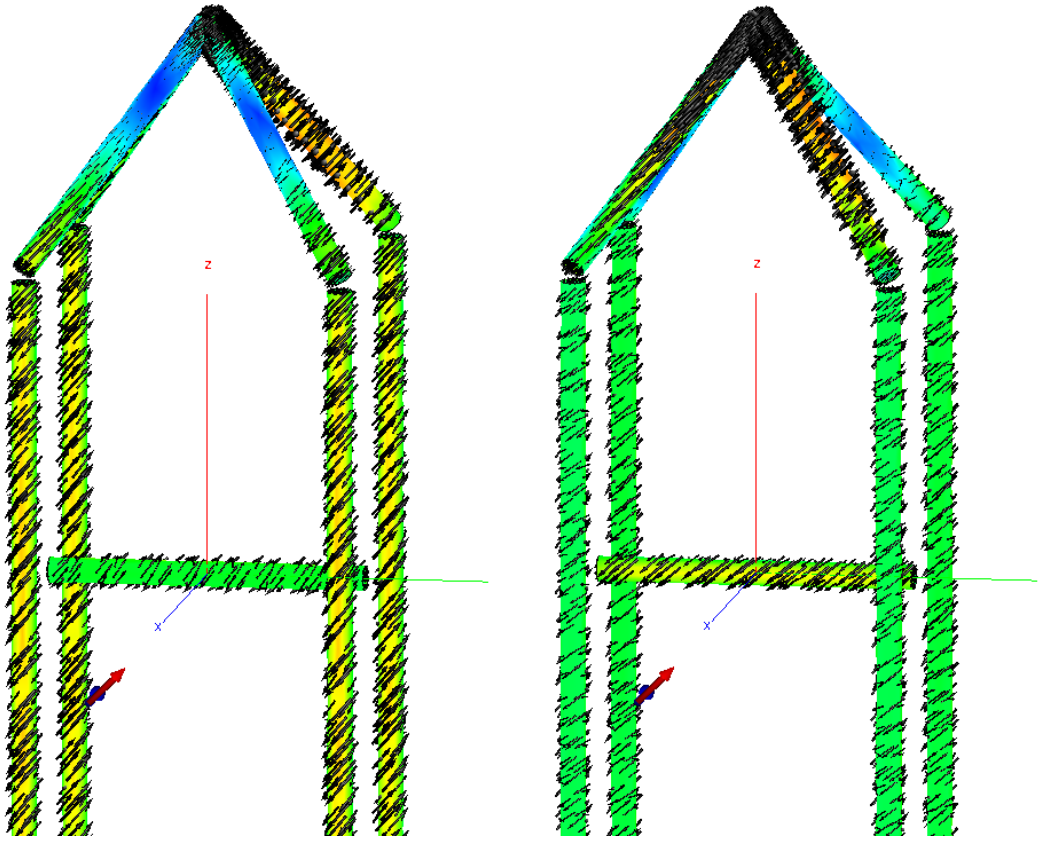

(a) (b)

Figure 35. Instantaneous impressed currents on a geometrical structure made of dielectric material ($\varepsilon_r = 5$), at $\omega t = 45°$ (a) and $\omega t = 135°$ (b).

5.2 Forward model

5.2.1 Derivation of a vectorial forward model with a dyadic contrast function

Consider the basic vectorial RF Tomography formulation, in a 3D homogeneous space:

$$E^{\mathrm{s}}\left(\mathbf{r}^t, \mathbf{r}^r\right) = k_0^2 \iiint_D \mathbf{a}^r \cdot \mathbf{G}\left(\mathbf{r}^r, \mathbf{r}'\right) v\left(\mathbf{r}'\right) \mathbf{G}\left(\mathbf{r}', \mathbf{r}^t\right) \cdot \mathbf{a}^t d\mathbf{r}', \tag{5.31}$$

where:

- $\mathbf{r}^t$ and $\mathbf{r}_n^r$ indicate the location of the transmitting and receiving antenna;
- $\mathbf{a}^t$ and $\mathbf{a}^r$ indicate the spatial orientation of the transmitting and receiving antennas, which are assumed to be small dipoles[1];
- $\mathbf{G}$ is the dyadic Green's function for the homogeneous space;
- $v\left(\mathbf{r}'\right)$ is the scalar contrast function being reconstructed;
- $\mathbf{r}'$ is the variable of integration which spans the domain of investigation D.

The objective is to replace the scalar contrast function $v\left(\mathbf{r}'\right)$ with a vector quantity so as to be able to represent the de-polarization observed in thin, elongated metallic objects.

---

[1] In order to simplify the notation, the transpose operator has been omitted. It is implied that $\mathbf{a}^t$ is a column-vector and that $\mathbf{a}^r$ is a row vector instead.

In order to be able to perform matrix-vector multiplications correctly, the contrast function must be dyadic as well. Equation 5.31 therefore becomes:

$$E^{\mathrm{s}}\left(\mathbf{r}^t,\mathbf{r}^r\right)=k_0^2\iiint_D \mathbf{a}^r\cdot\mathbf{G}\left(\mathbf{r}^r,\mathbf{r}'\right)\cdot\mathbf{V}\left(\mathbf{r}'\right)\cdot\mathbf{G}\left(\mathbf{r}',\mathbf{r}^t\right)\cdot\mathbf{a}^t d\mathbf{r}', \tag{5.32}$$

where

$$\mathbf{V}(\mathbf{r}')=\begin{bmatrix} V_{xx} & V_{xy} & V_{xz} \\ V_{yx} & V_{yy} & V_{yz} \\ V_{zx} & V_{zy} & V_{zz} \end{bmatrix}. \tag{5.33}$$

The elements of Equation 5.32 can be further analyzed individually to understand their physical meaning. This is best done proceeding right to left. The term $\mathbf{G}\left(\mathbf{r}',\mathbf{r}^t\right)\cdot\mathbf{a}^t$ has the meaning of electric field incident in the domain D:

$$\mathbf{E}^{\mathrm{i}}=\mathbf{G}\cdot\mathbf{a}^t=\begin{bmatrix} E_x^{\mathrm{i}} \\ E_y^{\mathrm{i}} \\ E_z^{\mathrm{i}} \end{bmatrix}=\begin{bmatrix} G_{xx}a_x^t+G_{xy}a_y^t+G_{xz}a_z^t \\ G_{yx}a_x^t+G_{yy}a_y^t+G_{yz}a_z^t \\ G_{zx}a_x^t+G_{zy}a_y^t+G_{zz}a_z^t \end{bmatrix}. \tag{5.34}$$

The incident field multiplies the dyadic contrast function, and an equivalent impressed surface current term is obtained.

$$\mathbf{J} = \mathbf{V} \cdot \mathbf{E}^{\mathrm{i}} = \begin{bmatrix} J_x \\ J_y \\ J_z \end{bmatrix} = \begin{bmatrix} V_{xx}E_x^{\mathrm{i}} + V_{xy}E_y^{\mathrm{i}} + V_{xz}E_z^{\mathrm{i}} \\ V_{yx}E_x^{\mathrm{i}} + V_{yy}E_y^{\mathrm{i}} + V_{yz}E_z^{\mathrm{i}} \\ V_{zx}E_x^{\mathrm{i}} + V_{zy}E_y^{\mathrm{i}} + V_{zz}E_z^{\mathrm{i}} \end{bmatrix}. \tag{5.35}$$

It is evident that while a scalar contrast function will produce an induced current $\mathbf{J}$ which is always parallel to $\mathbf{E}^{\mathrm{i}}$, a dyadic contrast function can correctly represent de-polarization effects, thanks to its off-diagonal terms. This equivalent current produces a scattered field through the Green's function, which is projected onto the receiving antenna orientation.

To simplify the notation the auxiliary row vector $\mathbf{p}$ can be introduced, which groups the terms related to the receiver side:

$$\mathbf{p} = \mathbf{a}^r \cdot \mathbf{G} = \begin{bmatrix} p_x, & p_y, & p_z \end{bmatrix} = \begin{bmatrix} a_x^r G_{xx} + a_y^r G_{yx} + a_z^r G_{zx} \\ a_x^r G_{xy} + a_y^r G_{yy} + a_z^r G_{zy} \\ a_x^r G_{xz} + a_y^r G_{yz} + a_z^r G_{zz} \end{bmatrix}^{\mathrm{T}}. \tag{5.36}$$

The scattered field due to the contribution of the infinitesimal scatterer at location $\mathbf{r}'$ can be called $E^{\mathrm{s}}(\mathbf{r}')$, it is a scalar quantity which depends on both illumination and observation, and can be written as:

$$\begin{aligned} E^{\mathrm{s}}(\mathbf{r}') = \mathbf{p}\cdot\mathbf{J} &= p_x J_x + p_y J_y + p_z J_z \\ &= p_x\left(V_{xx}E_x^{\mathrm{i}} + V_{xy}E_y^{\mathrm{i}} + V_{xz}E_z^{\mathrm{i}}\right) \\ &+ p_y\left(V_{yx}E_x^{\mathrm{i}} + V_{yy}E_y^{\mathrm{i}} + V_{yz}E_z^{\mathrm{i}}\right) \\ &+ p_z\left(V_{zx}E_x^{\mathrm{i}} + V_{zy}E_y^{\mathrm{i}} + V_{zz}E_z^{\mathrm{i}}\right). \end{aligned} \tag{5.37}$$

All the known terms in Equation 5.37, which correspond to a given configuration of transmitting and receiving antennas, can now be grouped into a linear operator $\mathbf{l}$, namely:

$$\begin{aligned} \mathbf{l}\left(\mathbf{r}^t, \mathbf{a}^t, \mathbf{r}^r, \mathbf{a}^r\right) &= \left[\begin{array}{cccccccccc} l_{xx}, & l_{xy}, & l_{xz}, & l_{yx}, & l_{yy}, & l_{yz}, & l_{zx}, & l_{zy}, & l_{zz} \end{array}\right] \\ &= \left[\begin{array}{cccccccccc} p_x E_x^{\mathrm{i}}, & p_x E_y^{\mathrm{i}}, & p_x E_z^{\mathrm{i}}, & p_y E_x^{\mathrm{i}}, & p_y E_y^{\mathrm{i}}, & p_y E_z^{\mathrm{i}}, & p_z E_x^{\mathrm{i}}, & p_z E_y^{\mathrm{i}}, & p_z E_z^{\mathrm{i}} \end{array}\right]. \end{aligned} \tag{5.38}$$

Notice that in Equation 5.38 the order in which the terms are arranged into a row is irrelevant, as long as it matches the order used to represent the contrast function, as described in the next section.

Since normally more that one antenna and/or polarization is used, multiple row vectors like the one described in Equation 5.38 can be stacked to form the full matrix $\mathbf{L}$. The number

of transmitting and receiving antennas is arbitrary, indicated by M and N respectively. Theoretically, also the number of polarizations is arbitrary. However, in practice it often makes sense to consider only three orthogonal polarizations for each antenna, for a total number of measurements equal to $M \times N \times 9$.

$$\mathbf{L} = \begin{bmatrix} \mathbf{l}\left(\mathbf{r}_1^t, \mathbf{a}_1^t, \mathbf{r}_1^r, \mathbf{a}_1^r\right) \\ \vdots \\ \mathbf{l}\left(\mathbf{r}_M^t, \mathbf{a}_3^t, \mathbf{r}_N^r, \mathbf{a}_3^r\right) \end{bmatrix}. \tag{5.39}$$

5.2.2 Building the dyadic contrast function

Now, it arises the need to fill out the elements of the matrix $\mathbf{V}$ (Equation 5.33). This matrix can be written as the sum of two terms. The need to use two terms originates from the physics of the problem. If there are no de-polarization effects, $\mathbf{V}$ should show elements different from zero only on its main diagonal. Instead, when de-polarization occurs also off-diagonal elements become different from zero. Ideally, if de-polarization were perfect $\mathbf{V}$ could be represented as a *linear* dyad, i.e. the product of two vectors forming a 3-by-3 matrix of rank 1. However, in reality de-polarization is not perfect and a complete dyad (i.e. full-rank matrix) is expected from the inversion.

As a result, it is expedient to represent $\mathbf{V}$ as the sum of two terms. The first term is a diagonal matrix representing the effects of the target when de-polarization effects are not strong. The second term is obtained as a dyadic product. In conclusion:

$$\mathbf{V}(\mathbf{r}') = \begin{bmatrix} V_{xx} & V_{xy} & V_{xz} \\ V_{yx} & V_{yy} & V_{yz} \\ V_{zx} & V_{zy} & V_{zz} \end{bmatrix} = \epsilon_\delta \mathbf{I} + \begin{bmatrix} v_x \\ v_y \\ v_z \end{bmatrix} \begin{bmatrix} v_x & v_y & v_z \end{bmatrix}. \tag{5.40}$$

The terms of the dyad $\underline{\underline{\mathbf{V}}}$ need to be rearranged to match the same order used in Equation 5.38. To avoid confusion, the rearranged version of $\mathbf{V}$ can be called $\mathbf{t}$.

$$\mathbf{t}(\mathbf{r}') = \begin{bmatrix} v_{xx}, & v_{xy}, & v_{xz}, & v_{yx}, & v_{yy}, & v_{yz}, & v_{zx}, & v_{zy}, & v_{zz} \end{bmatrix}^{\mathrm{T}}. \tag{5.41}$$

The domain of investigation D is then discretized into pixels and one vector $\mathbf{t}$ is created for each pixel. All these vectors are then stacked into a larger column vector $\mathbf{T}$. If the number of pixels is equal to P the vector $\mathbf{T}$ will have size $9P \times 1$ and will be given by:

$$\mathbf{T} = \begin{bmatrix} \mathbf{t}\left(\mathbf{r}'_1\right) \\ \vdots \\ \mathbf{t}\left(\mathbf{r}'_P\right) \end{bmatrix}. \tag{5.42}$$

It is then finally possible to write the forward model equation as a matrix-vector multiplication.

$$\mathbf{E}^{\mathrm{s}} = \mathbf{L} \cdot \mathbf{T}. \tag{5.43}$$

Equation 5.43 is substantially the same as Equation 2.4, with the only difference that the number of unknown pixels is multiplied by 9.

5.3 Inversion

The forward model obtained in Equation 5.43 must be inverted to obtain the dyadic contrast function. The simplest way to do so is to apply any regularized inversion routine, either direct (e.g. Truncated Singular Value Decomposition) or iterative (Conjugate Gradient, Algebraic Reconstruction Technique) to Equation 5.43.

After retrieving the vector $\mathbf{T}$, its elements need to be rearranged so as to create 9 reconstructed images versions, each one corresponding to a different orientation, i.e. xx, xy and so forth. The result can be visualized as a 3-by-3 collection of images.

The following examples show this method at work. In all examples images are obtained using the Conjugate Gradient method described in Chapter 4, without enforcing any physical bound.

5.3.1 Example 1

In the first example a thin, elongated cylinder is placed at a 45-degree angle in the xz plane, as shown in Figure 36. The object crosses the xy plane at $x = 5$ cm and $y = 5$ cm.

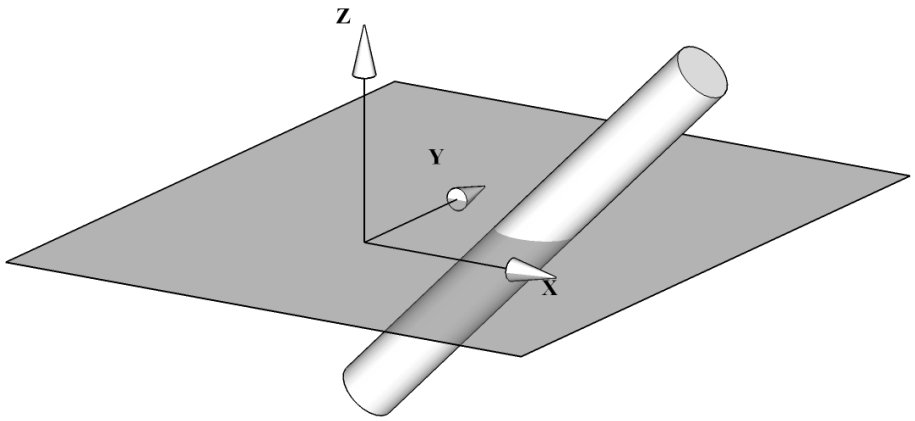

Figure 36. Geometry for Example 1. The imaging target is a thin PEC cylinder which intersects the xy plane at a 45° angle.

Antennas are placed in the xy plane at $z = 0$. In this example 21 transmitters and 40 receivers are employed, all of which transmit and receive in all 3 polarizations ($\hat{x}$, $\hat{y}$ and $\hat{z}$). The antennas are placed along a radius of 44.5 cm for the transmitters and 23.1 cm for the receivers. The frequency of operation is 3.16 GHz ($\lambda \approx 9.5$ cm). Overall, $21 \times 40 \times 9 = 7560$ measurements are collected.

The area under investigation is a square centered in the origin, of side equal to 20 cm, partitioned into pixels of size $\lambda/10$. This corresponds to a total of $21 \times 21 \times 9 = 3969$ unknowns. The problem is therefore over-determined.

Two cases are simulated. In the first one the object is made of Perfect Electric Conductor, in the second it is made of a dielectric material with $\epsilon_r = 3$.

PEC object

The result of the inversion for the PEC object is shown in Figure 37. The image shows that only xx, xz, zx and zz components of the image produce pixels significantly different from zero (the actual value of the pixel is of no importance because of the Born approximation). This means that the object is placed in the xz plane.

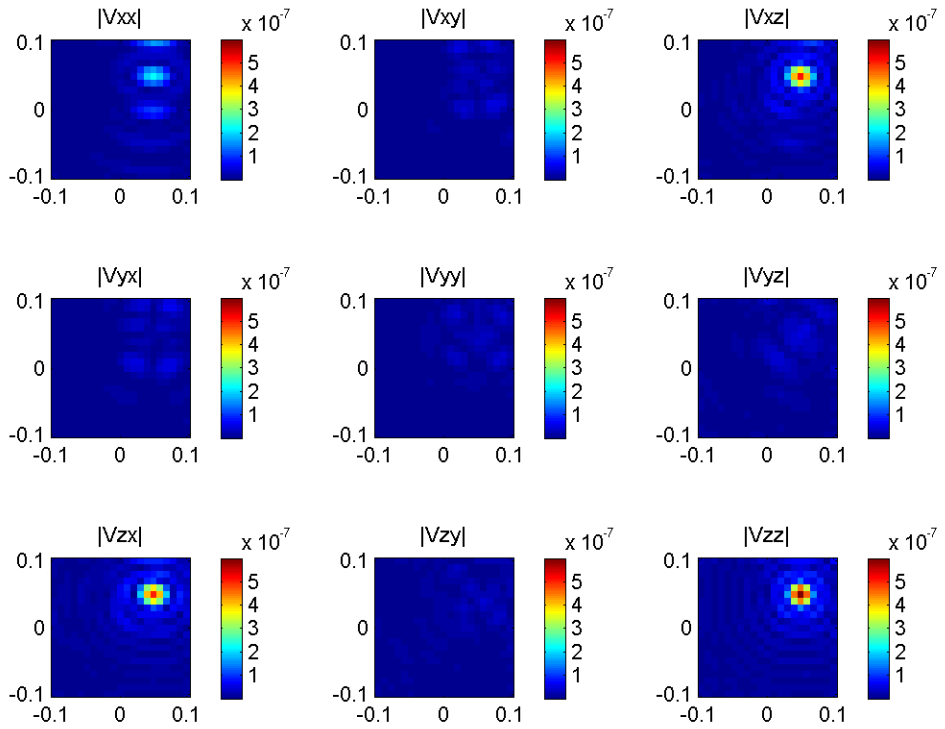

Figure 37. Result of the inversion for a PEC object. The figure shows shows the 9 versions of the image, one per spatial component.

The image also shows that the zz response is stronger than the others. This is because of the pattern of the antennas. Since the small dipole are placed in the xy plane, only when transmitter and receiver are oriented in the $\hat{z}$ direction there are no nulls pointing towards the object. The other polarizations will be affected by nulls and therefore will produce a weaker response.

Dielectric object

The imaging result for the dielectric object is shown in Figure 38. The image shows a clear response only in the zz component, with weaker responses in the xx and yy components. This is because, as expected, the dielectric object does not cause a strong depolarization of the incident field. Only the diagonal terms should be different than zero. However, because of the way the samples are taken, the zz case is predominant and tends to mask the result of the other cases.

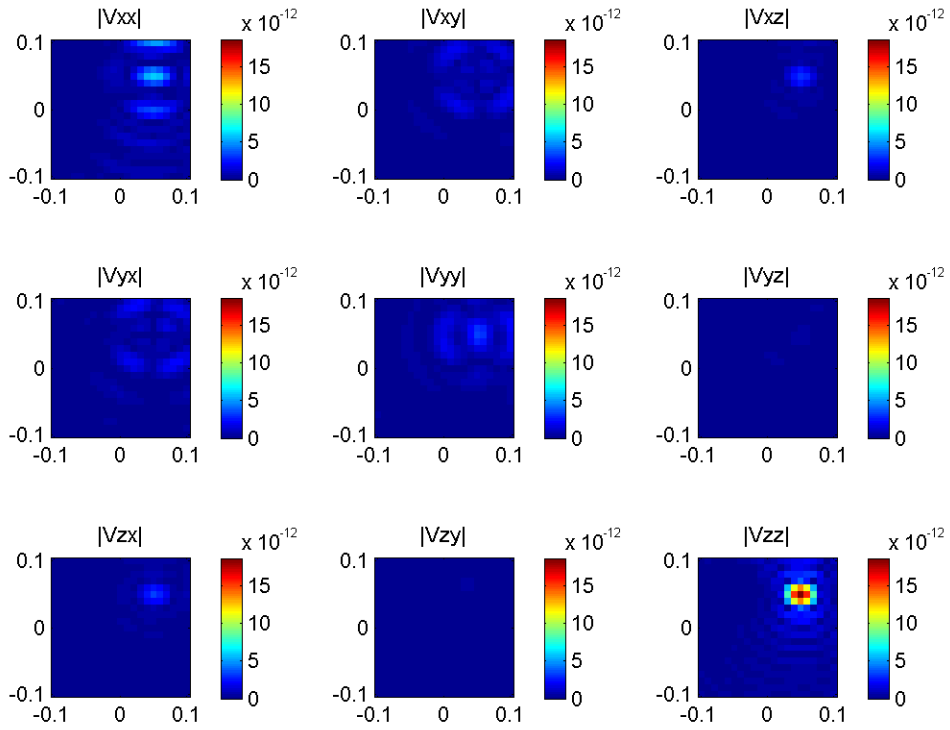

Figure 38. Result of the inversion for a dielectric object. The figure shows shows the 9 versions of the image, one per spatial component.

5.3.2 Example 2

In the second example a thin, elongated cylinder is placed parallel to the $\hat{x}$ axis, lying in the xy plane, as shown in Figure 39. The object stretches in the left semi-plane, at $y = 5cm$.

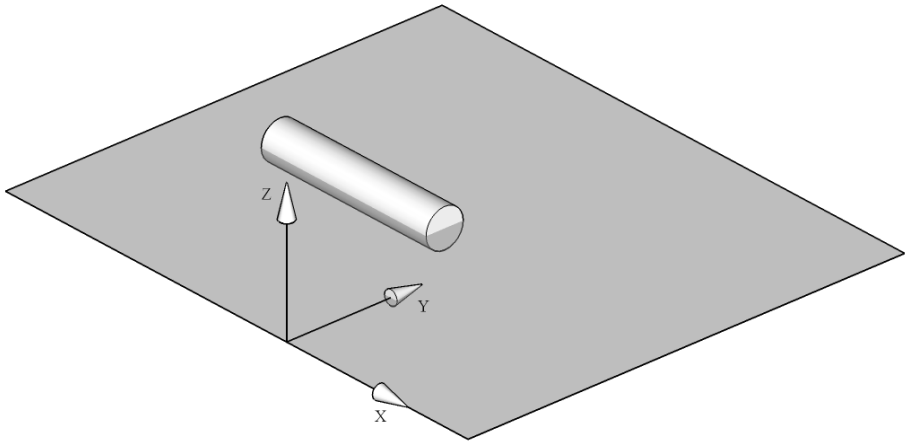

Figure 39. Geometry for Example 2.

This case is more difficult to reconstruct than the previous, due to the orientation of the object, which lies in the plane that gave a weak response in the previous example, due to the pattern of the antennas.

Two cases are simulated. In the first one the object is made of Perfect Electric Conductor, in the second it is made of a dielectric material with $\epsilon_r = 3$. The simulation conditions are the same as before and so is the domain under investigation.

PEC object

The result of the inversion for the PEC object is shown in Figure 40. The image shows that, as expected, only the top-left terms produce an observable response. The xx response is the strongest, although affected by visible artifacts. The artifacts are due to the small size of the object, which is placed in the same plane of measurement, thus offering an incomplete view from the antennas. In addition, the pattern effect is expected to be stronger in this case, because the zz response is almost null.

Dielectric object

The imaging result for the dielectric object is shown in Fig. Figure 41. The dielectric object shows a clear response only in the zz component, with weaker responses in the xx and yy components. The analysis in this case is the same as before. As expected, the dielectric object does not cause a strong depolarization of the incident field. Only the diagonal terms should be different than zero. However, because of the way the samples are taken, the zz case is predominant and tends to mask the result of the other cases.

These results show how a change in the way the contrast function is defined can bring additional information regarding the spatial orientation of the target. However, there is still an interpretation step that must be performed by a user in order to fully understand the results. In the next section it is shown how the images obtained in these examples can be further processed to gain a more direct visualization of the orientation of the objects.

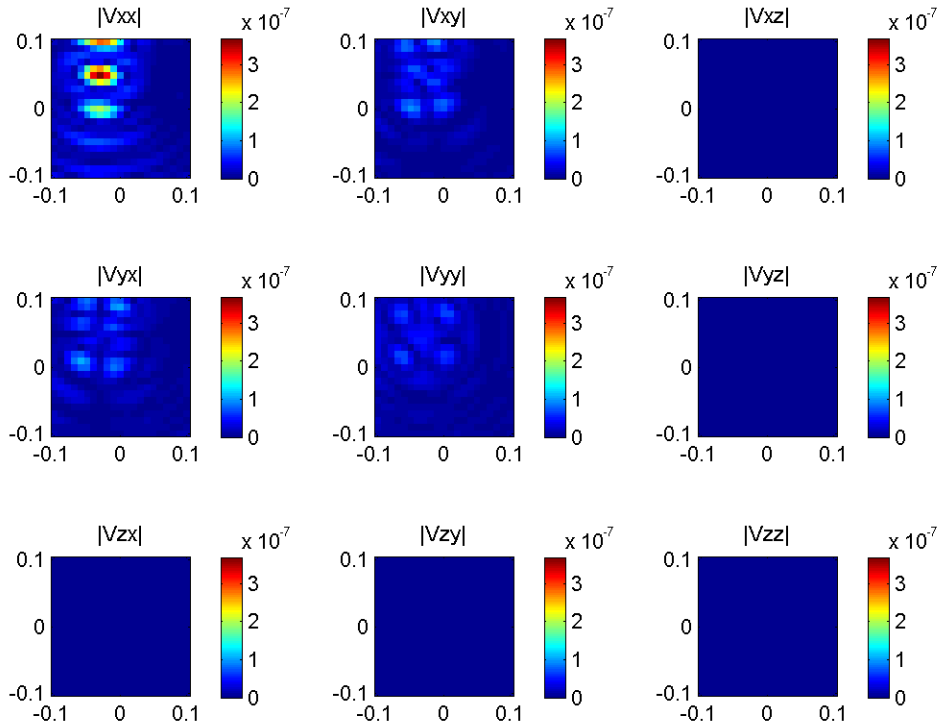

Figure 40. Result of the inversion for a PEC object.

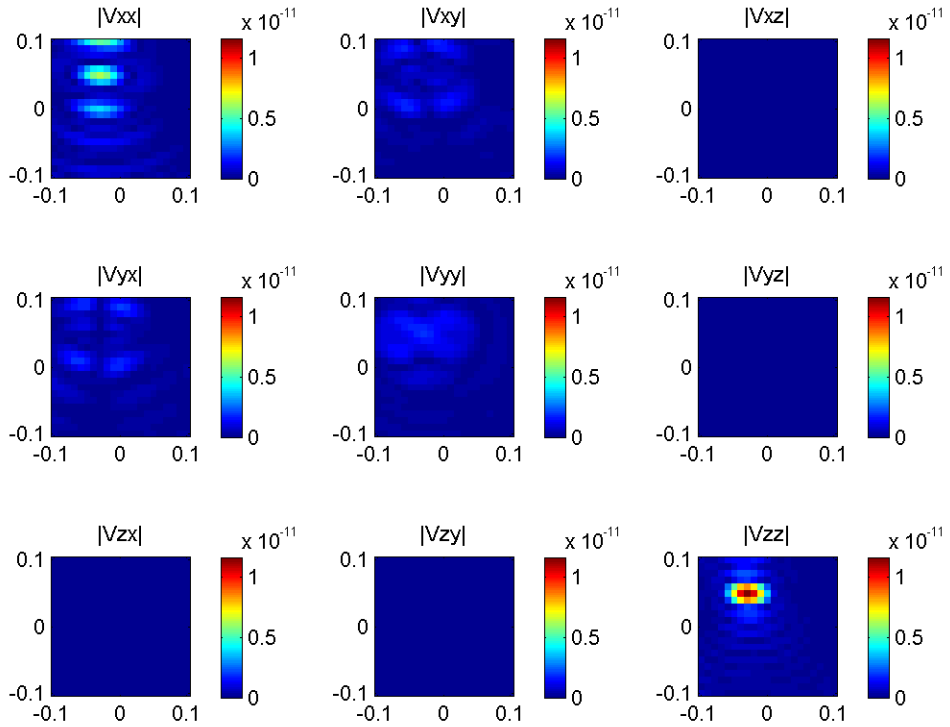

Figure 41. Result of the inversion for a dielectric object.

5.4 Eigenvalues-eigenvectors analysis

The goal of this analysis is to provide a different representation of the results, to complement the set of 9 images generated in the previous examples. This can be done by making a change in the data representation.

Instead of building a set of 3-by-3 images, each one made of P pixels and representing a given orientation in space, P matrices are constructed, each one made up of 3-by-3 elements. The first matrix collects the xx, xy, xz, yx, yy, yz, zx, zy and zz elements of the first pixel in the domain under investigation. The second matrix collects again the xx, xy, etc. elements of the second pixel in the domain under investigation, and so forth until P matrices are obtained.

The eigenvalues and eigenvectors associated with each of the P matrices are found by solving the problem:

$$\mathbf{V} \cdot \mathbf{u} = \lambda \mathbf{u}, \tag{5.44}$$

where $\mathbf{u}$ is an auxiliary vector. The vectors $\mathbf{u}$ satisfying Equation 5.44 are called eigenvectors and their corresponding values of λ are called eigenvalues. For a 3-by-3 matrix there will be at most 3 eigenvalues and 3 eigenvectors.

If de-polarization is strong, because of the way the matrix $\mathbf{V}$ was built, there will be one large eigenvalue (λ_1) and two smaller eigenvalues (λ_2 and λ_3). Therefore, the eigenvector $\mathbf{u}_1$ associated with λ_1 will give $\mathbf{v}$, i.e. the orientation of the pixel in space (see Equation 5.40);

λ_1 will give a measure of the magnitude of the contrast. The other eigenvalues do not provide useful information so they are discarded.

The eigenvalue decomposition can be used to build a *quiver* plot of the contrast function. For each pixel the eigen-decomposition is performed. Then, only the eigenvalue with largest magnitude is kept, along with its corresponding eigenvector. The auxiliary vector $\mathbf{d}$ is built:

$$\mathbf{d} = \lambda_1 \mathbf{u}_1. \tag{5.45}$$

The collection of vectors $\mathbf{d}$ (one per pixel), can be plot as arrows pointing in a 3D space. To make the visualization easier, the quiver plot can be superimposed to the image representing the sum of all 9 components, as used in the previous section. This allows to generate images which are extremely easy to interpret, as can be shown by looking at the result for the same examples showed before.

5.4.1 Single target: example 1

PEC object

The same result obtained in Figure 37 can be processed with the eigen-decomposition just described. The result of this analysis is shown in Figure 42.

The quiver plot provides a very insightful description of the object. The location of the object is indicated by the magnitude of the arrows, which indicate by their direction how the target is oriented in the 3D space.

Dielectric object

For the dielectric object the result of the eigen-decomposition is shown in Figure 43.

In this case the quiver plot indicates that the location of the object is the same, but that the orientation is mostly towards the $\hat{z}$ direction. This is again an effect of the different direction of the currents impressed on the target.

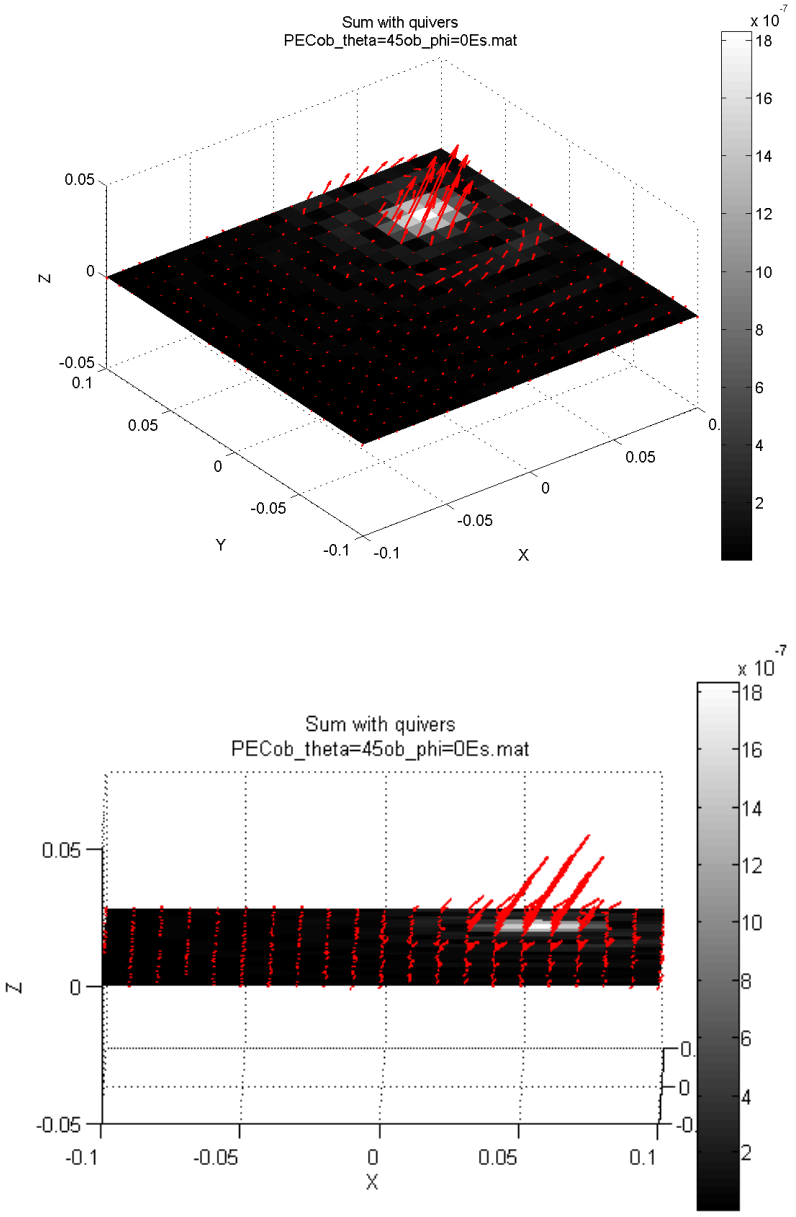

Figure 42. Quiver plot obtained with eigendecomposition for the PEC target. The gray image is the absolute value of the sum of all components of the image. Two views are provided.

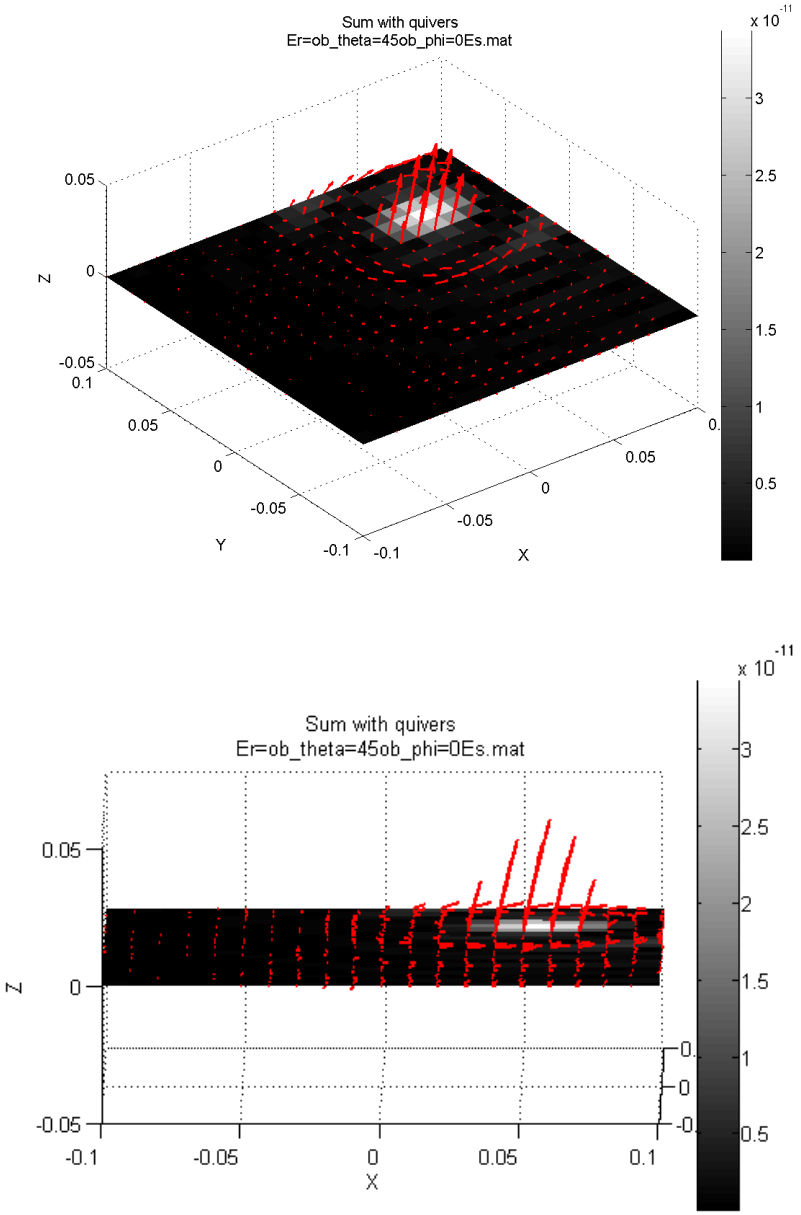

Figure 43. Quiver plot obtained with eigendecomposition for the dielectric target. The gray image is the absolute value of the sum of all components of the image. Two views are provided.

5.4.2 Single target: example 2

PEC object

The results for the second example, in the case of PEC, is shown in Figure 44.

For the PEC target the quiver plot indicates that the object is oriented along the $\hat{x}$ direction. Artifacts are present, and their orientation is nonetheless pointing in the same direction. Because of the artifacts it is difficult to estimate the actual position of the target. This problem cannot be solved unless the spatial sampling is changed.

Dielectric object

The dielectric target provides a more difficult interpretation, as shown in Figure 45. Due to the absence of the depolarization effects, the pixels significantly different from zero provide different clues to the orientation of the object. The strongest pixels are oriented along $\hat{x}$, but the ringing artifacts point to all directions in the xy plane.

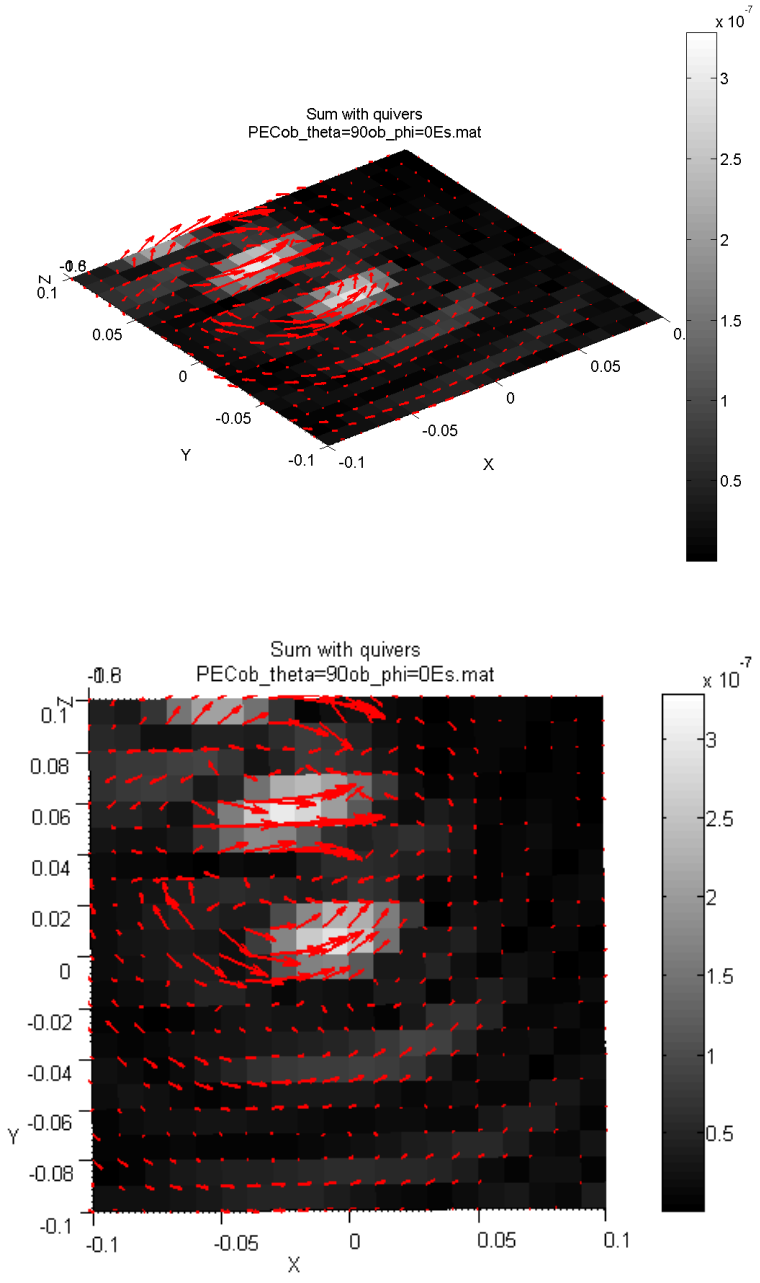

Figure 44. Quiver plot obtained with eigendecomposition for the PEC target. The gray image is the absolute value of the sum of all components of the image.

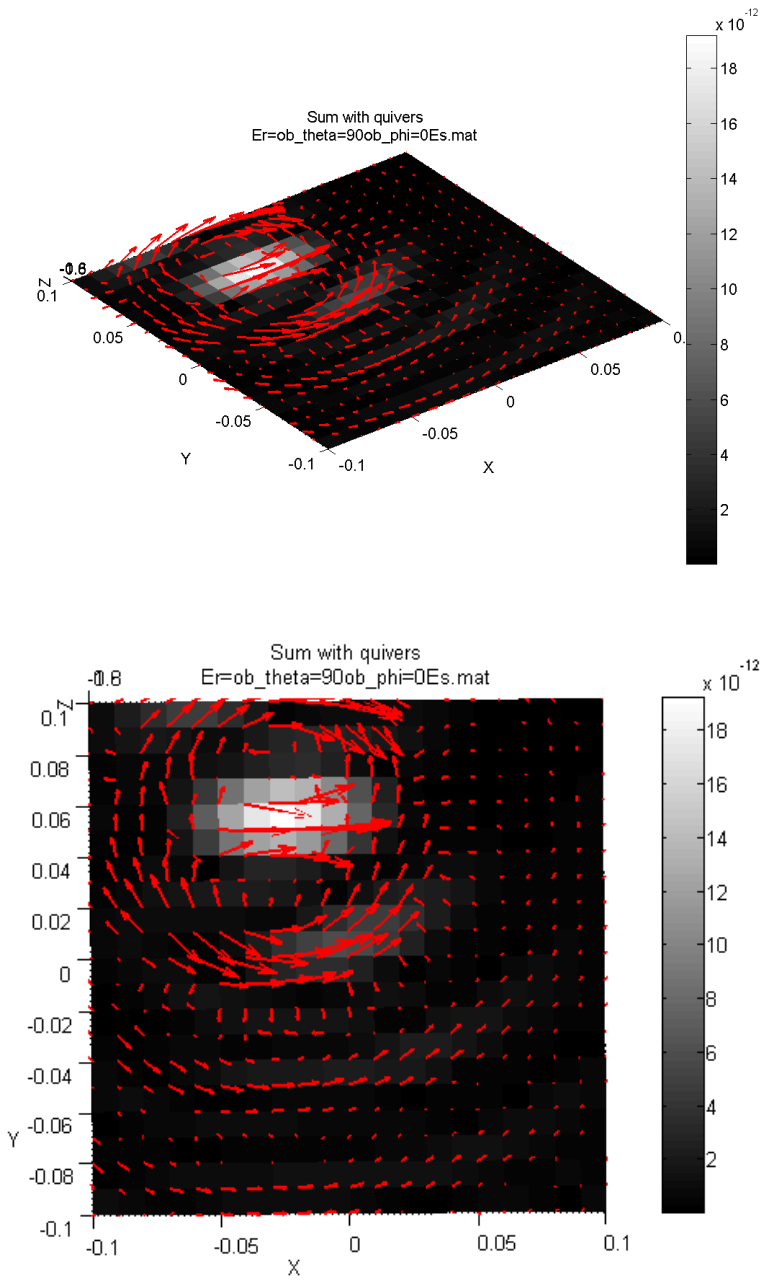

Figure 45. Quiver plot obtained with eigendecomposition for the dielectric target. The gray image is the absolute value of the sum of all components of the image. Two views are provided.

5.4.3 Multiple targets

This last example shows reconstruction results when multiple objects are present in the domain of investigation. The geometry under consideration is depicted in Figure 46.

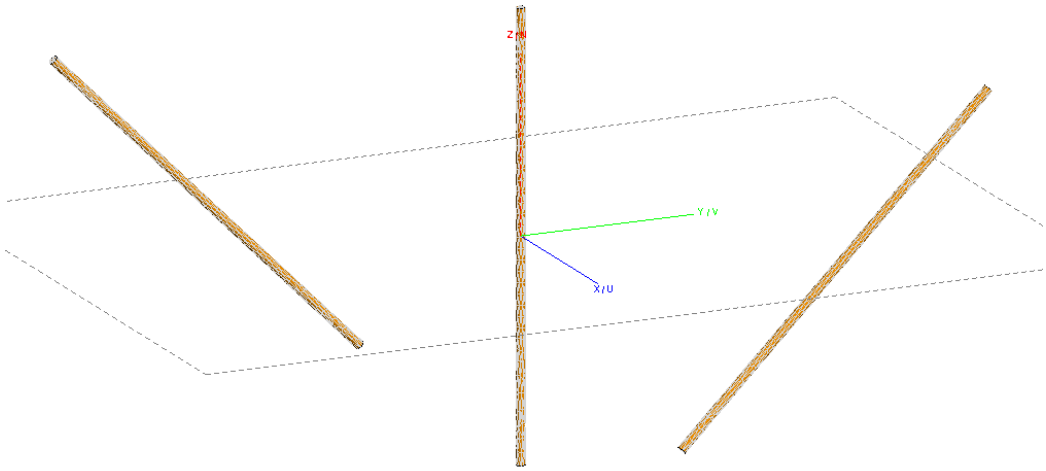

Figure 46. Geometry for testing of the dyadic contrast function. Three metallic thin cylinders are present in the scene, with three different spatial orientations.

Three objects are present in the scene. All cylinders are made of PEC and have radius equal to 0.1 cm and length equal to 10 cm. The first cylinder intersects the $z = 0$ plane at coordinates $x = y = 5$ cm and is oriented at an angle toward the positive y axis, i.e. in a standard spherical coordinates system it is oriented toward $\theta = 45°$ and $\phi = 90°$. The second cylinder intersects the $z = 0$ plane at coordinates $x = y = 0$ cm and is oriented

toward the positive z axis, i.e. in a standard spherical coordinates system it is oriented toward $\theta = 0°$ and $\phi = 0°$. The third cylinder intersects the $z = 0$ plane at coordinates $x = y = -5$ cm and is oriented at an angle toward the negative y axis, i.e. in a standard spherical coordinates system it is oriented toward $\theta = 45°$ and $\phi = -90°$.

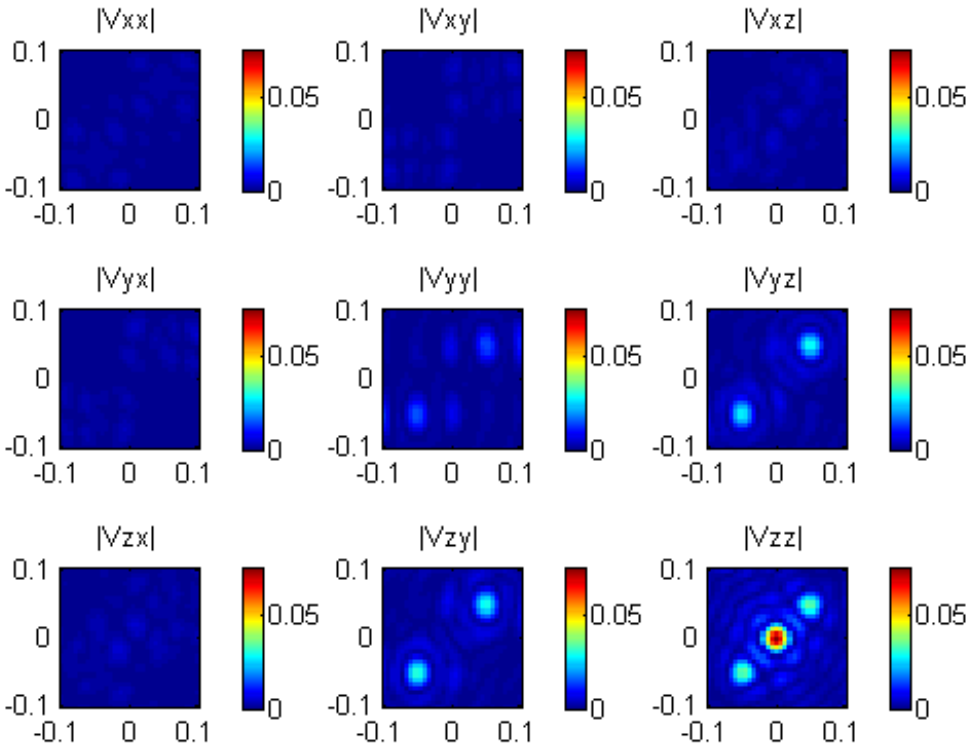

Figure 47. Absolute value of components of dyadic contrast function.

The result of the inversion using the dyadic contrast function is shown in the following figures. Figure 47 shows the absolute value of the 9 components of the dyadic contrast. The strongest response is given by the zz component, for the same reasons explained for the other examples. In the zz image, the object in the center clearly stands out, while ti does not in any other image.

The other significant responses are given by yz, zy and yy, with the latter being weaker again because of the advantage that the antennas orientation give to the z components.

From the reconstruction of the absolute value image it is evident that the objects in the corner positions are oriented in the yz or zy direction, but it is impossible to say which one of the two. The phase plot shown in Figure 48 only partially helps clearing the doubt.

Figure 48 is of difficult interpretation because the phase is shown for all pixels, including the ones whose magnitude is small, so non-interesting. To make the plot easier to read it is possible to plot the phase scaled by the magnitude, i.e.

$$\mathbf{\Omega} = |\mathbf{V}| \cdot \angle\underline{\mathbf{V}} \tag{5.46}$$

The plot of Ω is shown in Figure 49.

Looking at the yz and zy components it can be observed that the phase flips sign for the two objects. In the yz image it is positive for the bottom-left object and negative for the top-right object. For the zy image the situation is the same. Without some sort of prior knowledge, it is hard to understand how the two objects are oriented into space.

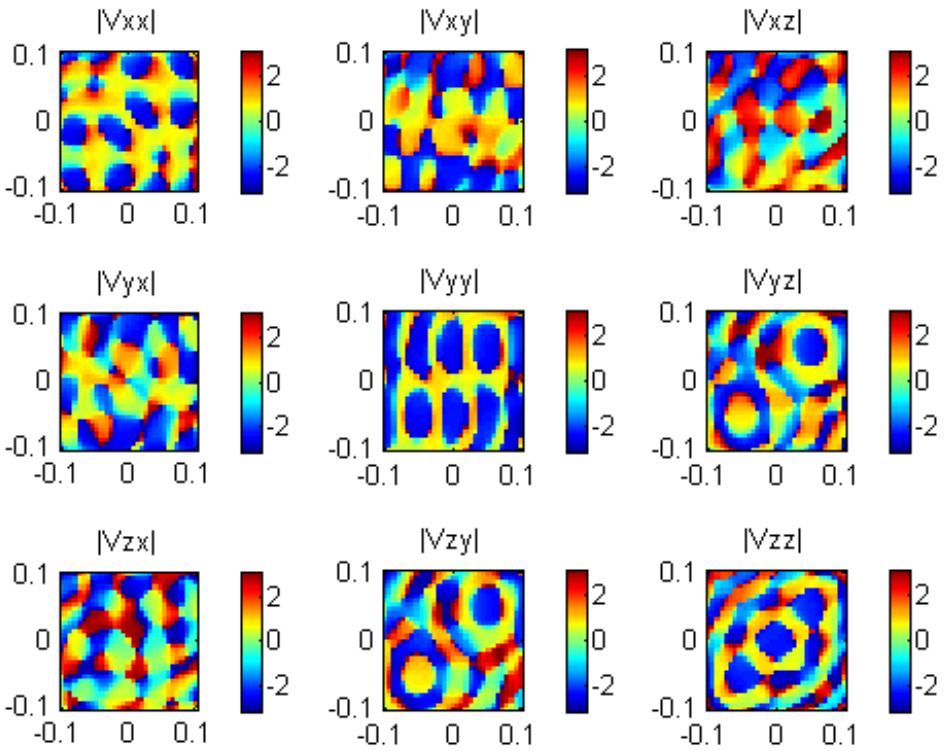

Figure 48. Phase of components of dyadic contrast function.

The quiver plot obtained with the eigen-decomposition clears the dilemma. As shown in Figure 50 the eigenvectors multiplied by their corresponding eigenvalues, correctly point in the direction toward which the object is oriented.

In conclusion, the formulation described in this chapter allows to correctly reconstruct thin metallic objects oriented in different directions in space. A dyadic contrast function is

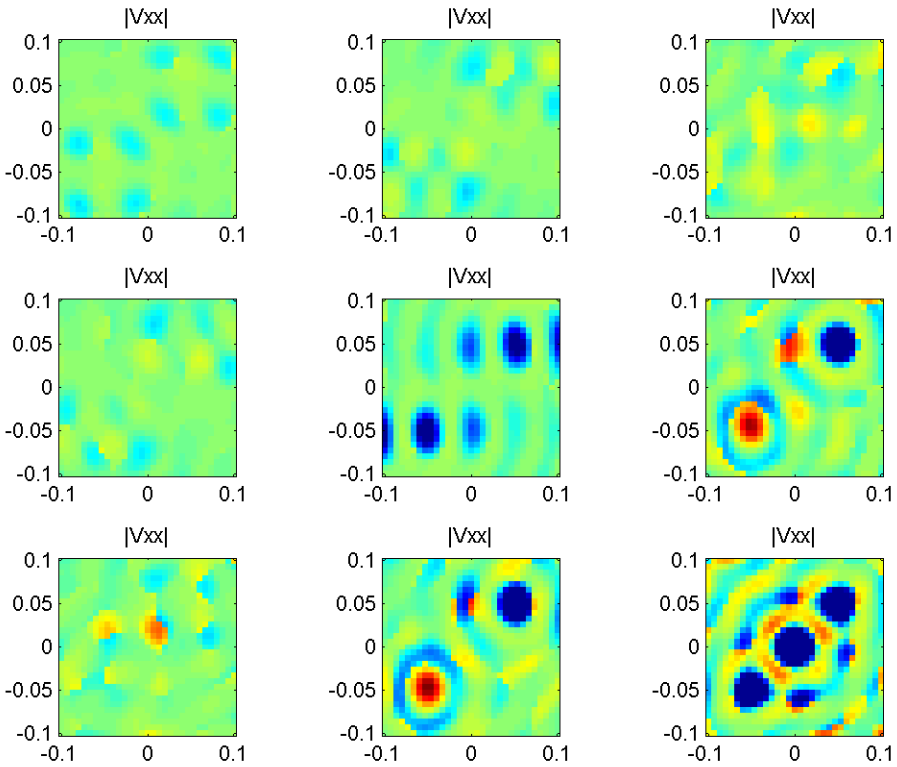

Figure 49. Phase of components of dyadic contrast function scaled by the relative magnitude at each pixel. The plot highlights the phase information only where the magnitude is sufficiently big to represent an actual object instead of noise.

developed and introduced into the classical RF Tomography forward model. Usual inversion routines can be employed to reconstruct the dyadic contrast, thanks to a data organization which makes the problem larger but does not change its structure (linear system of equations). The result of the inversion in the form of 2D color plots is augmented with a

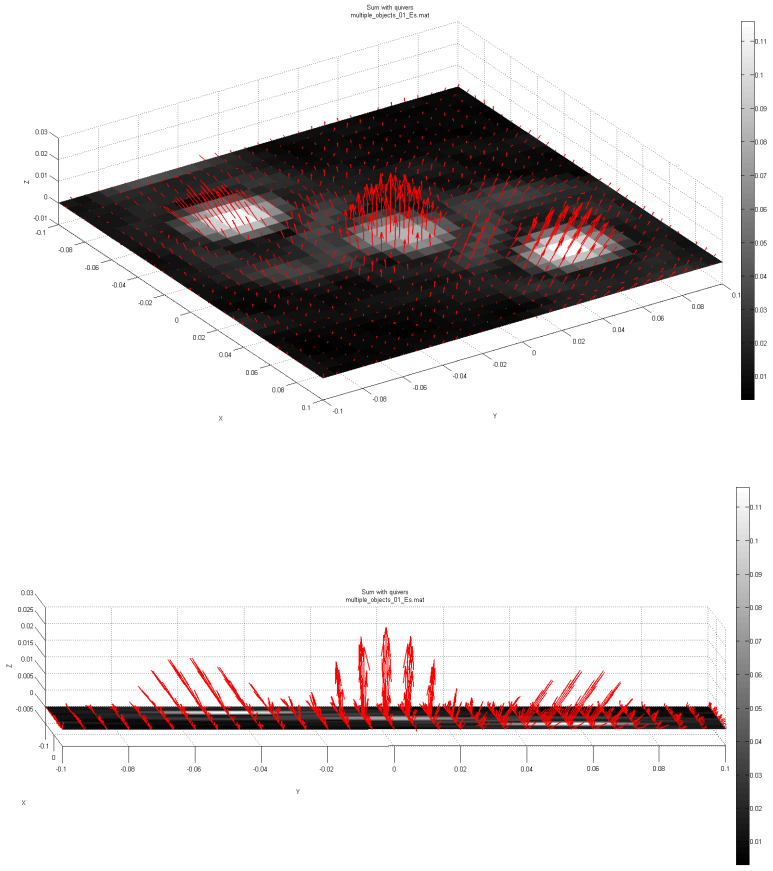

Figure 50. Quiver plots, highlighting the different orientation of the objects being reconstructed.

3D visualization based on an eigen-decomposition, which allows to give a straightforward representation of the orientation of the objects in space, providing overall more actionable results.

CHAPTER 6

QUADRATIC FORWARD MODEL

A quadratic forward model is developed to remove some of the limitations associated with the Born approximation, which was initially introduced to linearize and solve the volume integral equation for the scattered field.

Although this approximation is used extensively in the remote sensing literature and, under certain conditions, it is indeed a valid approximation, there are cases where the Born approximation does not work well. When more than one target is present in the volume under investigation, multiple scattering phenomenon can indeed generate artifacts. Also, when the target is not a weak scatterer, quantitative reconstruction is impossible. This is also why in the study of iterative algorithms as inversion methods alternative to TSVD presented in 4, the physical bounds have been introduced only on the sign of the real and imaginary parts of the contrast vector, and images are always normalized: the Born approximation does not make it possible to achieve good quantitative reconstruction.

In addition, it can be shown that the linear operator $\mathbf{L}$, developed under the Born approximation, acts as a filter on the spatial harmonics of the reconstructed contrast function. As a result, sharp edges cannot be normally imaged correctly. In fact, the Born approximation is one of the biggest obstacles in increasing the resolution of an RFT system.

In the literature, a number of methods have been developed to overcome these limitations. These algorithms are employed particularly in applications where quantitative

reconstruction is necessary in order to consider imaging successful, such as medical imaging. The two most popular methods are the Born Iterative and Distorted Born methods (88; 89).

The Born Iterative method consists in a numerical algorithm which involves the solution of multiple inverse and forward problems. First, the Born approximation is used to obtain an estimation of the contrast function, solving an *inverse* problem; this estimation is then used to calculate the scattered electric field that such a contrast function would cause[1], by solving a *forward* problem, which, incidentally, is usually much more computationally demanding than the inverse one. The field estimated in this method is compared to the one actually measured: if the difference between the two is too large (according to some user-imposed rule) it is used to estimate a new contrast function, and so on.

Although numerically heavy, the Born Iterative method has gained wide popularity, due to its straightforward structure and to the good quantitative results that can be obtained using it (88).

The Distorted Born (or Distorted Born Iterative) method is a further advance on the Born Iterative method (89). In addition to the iterative procedure, at every step the Green's function is updated. This allows for faster convergence, which is beneficial because it reduces, as a side effect, the number of times the forward problem has to be solved, hence, it reduces the computational load.

---

[1]Since these are ill-posed problems, the solution to the inverse problem is never the one that would explain exactly the starting data from which it was obtained, but it is always an approximation.

Like every iterative algorithm, Born and Distorted Born Iterative methods could fail to converge to the right solution, depending on their starting point. Therefore, a different approach can be considered.

This chapter deals with the development of a forward model which overcomes some limitations imposed by the Born approximation. A few papers (90; 91; 92) provide motivation for this work. All of them are based on the development of an analytical solution, based on a quadratic forward model, which promises to overcome the limitations given by the Born approximation, while at the same time avoiding the computational burden given by the Born and Distorted Born Iterative methods.

In order to better understand the origin of this idea, in this chapter the RF Tomography forward model is derived again, to highlight where and how the Born approximation comes into play, and how it can be replaced with a quadratic formulation.

In addition, in order to limit the size of the problem and make the inversion more treatable from a computational point of view, the inversion is recast into an optimization problem involving contrast functions which can be represented with a limited number of spatial harmonics. A detailed description of this method is provided.

In the end, simulation results are present to show advantages and limitations of the quadratic model with respect to the Born approximation.

6.1 Forward model derivation

To understand how to develop a quadratic model, it is convenient to start from the basic Volume Integral Equation around which RF Tomography is based (47). This equation

expresses the scattered field as an integral equation involving the total electric field, the contrast function, and the Green's function appropriate to the environment where sensing is being performed. In order to simplify this derivation as well as the following ones, the model is derived in 2D space, where the objects are assumed to extend to infinity in the z direction. Also, the TX antennas are assumed to be infinite current lines. As a result:

$$E^{\mathrm{s}}(\mathbf{r}^{\mathrm{r}}) = k_0^2 \iint\limits_D \chi(\mathbf{r}')E^{\mathrm{t}}(\mathbf{r}')g_e(\mathbf{r}', \mathbf{r}^{\mathrm{r}})d\mathbf{r}', \tag{6.1}$$

where the contrast function is indicated with the variable χ, in order to highlight the difference between the scalar contrast function in a 3D space (standard RF Tomography formulation) and the dyadic contrast developed in Chapter 5. Also, the scalar Green's function is indicated with g_e, where the symbol e indicates *external*. The need for this will be explained in the following.

Equation 6.1 is *exact*, unlike Equation 2.2 which is an approximation obtained applying the Born approximation. The reason for the introduction of the Born approximation is that the total field inside Equation 6.1 includes also the scattered field, making the problem non-linear.

In Equation 6.1 the term $E^{\mathrm{t}}(\mathbf{r}')$ can be expanded using another Volume Integral Equation inside the same domain of investigation, as

$$E^{\mathrm{t}}(\mathbf{r}') = E^{\mathrm{i}}(\mathbf{r}') + k_0^2 \iint\limits_D \chi(\mathbf{r}'')E^{\mathrm{t}}(\mathbf{r}'')g_i(\mathbf{r}', \mathbf{r}'')d\mathbf{r}'', \tag{6.2}$$

where this time the symbol g_i indicates *internal* Green's function and the auxiliary variable $\mathbf{r}''$ is introduced.

The difference between external and internal Green's functions can be now explained with the help of Figure 51.

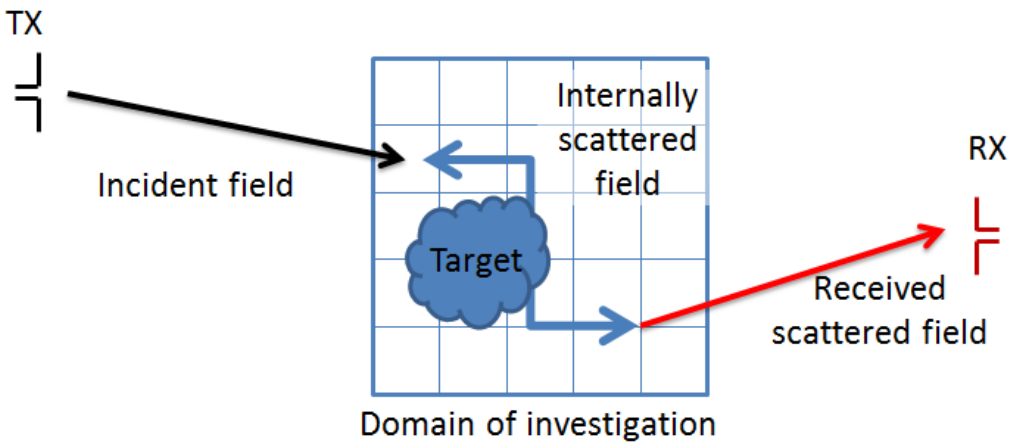

Figure 51. Pictorial representation of the scattering phenomenon.

The transmitter generates the incident field, which travels to the domain D and impinges upon the target(s). The total field is the sum of the incident one plus all the contributions due to interactions inside the domain of investigation. All these interactions (which are non-linear) originate the impressed currents, which in turn will give rise to the scattered field. Therefore, the scattering phenomenon can be divided in two stages. First, the incident field generates the total field inside the domain D; this is represented with the internal Green's

function g_i. Then, the domain can be seen as a "black box": assuming that the total field inside D was somehow generated, the scattered field at the location of the receiving antenna is its consequence, and it is explained with the external Green's function g_e.

If the domain under investigation is partitioned into many pixels, g_i explains the pixel-to-pixel interactions, while g_e explains the pixel-to-RX interactions.

The Born approximation consists in assuming that the second term of Equation 6.2 is so small compared to the incident field that it can be neglected. Therefore, in Equation 6.1 the total field is replaced with the incident field and a linear equation is obtained.

A formulation equivalent and alternative to the one of Equation 6.1 and Equation 6.2 is the one using an operator notation to replace the integrals.

In Equation 6.1 the term $\chi(\mathbf{r}')E^{\mathrm{t}}(\mathbf{r}')$ represents an equivalent impressed current, therefore the volume integral equation is an operator that receives as input an equivalent current, and returns an electric field, by applying the appropriate Green's function. This can be written as:

$$E^{\mathrm{s}}(\mathbf{r}^{\mathrm{r}}) = \mathbf{A}_{\mathrm{e}}\left[\chi(\mathbf{r}')E^{\mathrm{t}}(\mathbf{r}')\right]. \tag{6.3}$$

Similarly, Equation 6.2 can be rewritten using an operator notation as:

$$E^{\mathrm{t}}(\mathbf{r}') = E^{\mathrm{i}}(\mathbf{r}') + \mathbf{A}_{\mathrm{i}}\left[\chi(\mathbf{r}'')E^{\mathrm{t}}(\mathbf{r}'')\right]. \tag{6.4}$$

The domain of investigation is spanned by the vectors $\mathbf{r}'$ and $\mathbf{r}''$. Since the domain does not change, $\mathbf{r}'$ and $\mathbf{r}''$ are pointing in substance to the same pixels. When organizing the data on a computer, it is therefore convenient to organize the pixels pointed by $\mathbf{r}'$ and $\mathbf{r}''$ in the same order, so that in the end $E^{\mathrm{t}}(\mathbf{r}') = E^{\mathrm{t}}(\mathbf{r}'')$. In short, assuming that the pixels are organized in the same way, the position vectors $\mathbf{r}'$ and $\mathbf{r}''$ can be dropped and it is possible to write simply

$$E^{\mathrm{s}} = \mathbf{A}_{\mathrm{e}}(\chi E^{\mathrm{t}}) \tag{6.5}$$

and

$$E^{\mathrm{t}} = E^{\mathrm{i}} + \mathbf{A}_{\mathrm{i}}(\chi E^{\mathrm{t}}). \tag{6.6}$$

Now Equation 6.5 and Equation 6.6 can be combined into a single non-linear equation. Performing the usual division of the domain D into a finite number of pixels, and introducing a matrix-vector notation as in (8), it is possible to write:

$$\begin{aligned} E^{\mathrm{t}} &= E^{\mathrm{i}} \ + \mathbf{A}_{\mathrm{i}}(\chi E^{\mathrm{t}}) \\ E^{\mathrm{t}} - \mathbf{A}_{\mathrm{i}}(\chi E^{\mathrm{t}}) &= E^{\mathrm{i}} \\ (I - \mathbf{A}_{\mathrm{i}}\chi)E^{\mathrm{t}} &= E^{\mathrm{i}} \\ E^{\mathrm{t}} &= (I - \mathbf{A}_{\mathrm{i}}\chi)^{-1}E^{\mathrm{i}}, \end{aligned} \tag{6.7}$$

Then, substituting Equation 6.7 into Equation 6.5:

$$E^{\mathrm{s}}(\mathbf{r}^{\mathrm{r}}) = \mathbf{A}_{\mathrm{e}} \left[\chi (I - \mathbf{A}_{\mathrm{i}} \chi)^{-1} E^{\mathrm{i}} \right], \tag{6.8}$$

which is non-linear in χ.

The important term in Equation 6.8 is the one involving the inverse operation. It is possible to rewrite this term as the result of the summation of a geometrical series of argument $\mathbf{A}_{\mathrm{i}}\chi$. Introducing the auxiliary variable p, the sum of a geometrical series is written as:

$$(1-p)^{-1} = \frac{1}{1-p} = 1 + p + p^2 + \ldots, \ \|p\| < 1. \tag{6.9}$$

Similarly:

$$(\mathbf{1} - \mathbf{A}_{\mathrm{i}}\chi)^{-1} = \mathbf{1} + \mathbf{A}_{\mathrm{i}}\chi + (\mathbf{A}_{\mathrm{i}}\chi)^2 + \ldots, \ \|\mathbf{A}_{\mathrm{i}}\chi\| < 1. \tag{6.10}$$

Therefore an alternative way to explain the Born approximation is obtained. In Equation 6.10 the Born approximation is obtained by keeping only the first term in the summation.

The next logical step is to keep an additional term, thus obtaining a better approximation of the scattered field. Hence:

$$(\mathbf{1} - \mathbf{A}_{\mathrm{i}}\chi)^{-1} \approx \mathbf{1} + \mathbf{A}_{\mathrm{i}}\chi, \ \|\mathbf{A}_{\mathrm{i}}\chi\| < 1 \tag{6.11}$$

which leads to:

$$E^{\mathrm{s}}(\mathbf{r}^{\mathrm{r}}) \approx \mathbf{A}_{\mathrm{e}}\chi E^{\mathrm{i}} + \mathbf{A}_{\mathrm{e}}\left(\chi\mathbf{A}_{\mathrm{i}}\chi E^{\mathrm{i}}\right), \tag{6.12}$$

Equation 6.12 establishes a quadratic relationship between the contrast χ and the scattered field $E^{\mathrm{s}}(\mathbf{r}^{\mathrm{r}})$.

6.1.1 Numerical calculation of the operators

The calculation of the external operator on a computer is substantially equivalent to the calculation of the operator $\mathbf{L}$ in Equation 2.4. The only difference is that $\mathbf{L}$ already includes the incident field, therefore it depends on both transmitters and receivers; on the other hand, $\mathbf{A}_{\mathrm{e}}$ only includes the Green's function between pixels and receivers, therefore it does not depend on the transmitters.

Singular points are normally not a concern, as long as no receivers are located inside the domain of investigation. This is usually easily avoided by choosing an appropriate domain

D. As a result the operator $\mathbf{A}_{\mathrm{e}}$ is simply the collection of the values of the external Green's function in a 2D space:

$$g_e = H_0^{(2)}(\mathbf{r}', \mathbf{r}^{\mathrm{r}}), \tag{6.13}$$

where $H_0^{(2)}$ is the Hankel function of the second kind of order 0.

The derivation of the internal operator $\mathbf{A}_{\mathrm{i}}$, instead, is slightly more complicated. The internal operator describes the pixel-to-pixel iterations, therefore it will surely include singular points, because it is computed for each pixel with respect to every other pixel, including the starting pixel itself.

The numerical calculation of the integral of the Green's function in a 2D geometry in the presence of singularities has been derived in (87). An explicit solution for square pixels is not available, but it can be reasonably approximated with the solution for round pixels of diameter dx equal to the length of the side of the square pixels.

As a result:

$$\mathbf{A}_{\mathrm{i}}(\mathbf{r}'_1, \mathbf{r}'_2) = \begin{cases} -\dfrac{j\pi k_0 dx}{4} H_0^{(2)}(k_0(\mathbf{r}'_1 - \mathbf{r}'_2)) J_1(k_0 dx/2), & \mathbf{r}'_1 \neq \mathbf{r}'_2 \\ -\dfrac{j\pi k_0 dx}{4} H_1^{(2)}(k_0 dx/2) - 2j, & \mathbf{r}'_1 = \mathbf{r}'_2 \end{cases} \tag{6.14}$$

6.2 Harmonic contrast function

The calculation of the contrast function using the quadratic model can be computationally intensive. The numerical load can be made lighter by changing the way the contrast function is defined.

Normally, in RF Tomography, the domain under investigation is partitioned into pixels, which are then organized into a large vector and thus reconstructed. This normally leads to a large under-determined problem, because it is easy to have much fewer measurements than unknowns. Using the linear model (Born approximation) this is not a serious issue, because very efficient algorithms such as Conjugate Gradient can be employed. These can not only return a solution with a reasonable use of time and memory, but can also tackle the ill-conditioning described in Chapter 2.

Using the quadratic forward model the inversion is not so simple. Apart from the larger computational requirements, due to the term involving $\mathbf{A}_{\mathrm{i}}$, the problem is more complicated by the possible presence of local minima. In a linear model this is not a concern, because Ψ^{lin} is convex. Instead, Ψ^{quad} is quartic in χ, thus may have local minima in addition to an absolute minimum.

In order to make the problem easier to solve, one step is to make it over-determined instead of under-determined. One way of doing this is to express the contrast as a finite summation of spatial harmonics, then reconstruct the harmonics rather than the contrast itself.

The contrast χ can be written as a Discrete Fourier Transform:

$$\chi(x,y) = \sum_{m,n\in\mathbf{Z}} c_{m,n} e^{j2\pi mx/L_x} e^{j2\pi ny/L_y}, \tag{6.15}$$

where:

$$c_{m,n} = \frac{1}{L_x L_y} \iint \chi(x,y) e^{-j2\pi mx/L_x} e^{-j2\pi mx/L_x} dx\, dy. \tag{6.16}$$

The problem now is to reconstruct $c_{m,n}$ and then obtain χ in a second step. This can be done in two ways: the first way requires re-writing the whole forward model under the assumption of an harmonic contrast function, changing the definition of the operators and so forth. Alternatively, the second, easier way simply requires to change the optimization problem. In practice one will solve:

$$\begin{aligned} \underset{c_{m,n}}{\text{minimize}} \quad & \Psi^{\text{quad}} = \| E^{\text{s}}(\mathbf{r}^{\text{r}}) - \mathbf{A}_{\text{e}} \left[\chi \mathbf{A}_{\text{i}} \chi E^{\text{i}} \right] \|^2 \\ \text{with} \quad & \chi(x,y) = \sum_{m,n\in\mathbf{Z}} c_{m,n} e^{j2\pi mx/L_x} e^{j2\pi ny/L_y}. \end{aligned} \tag{6.17}$$

which in a modern computational tool such as MATLAB is done very simply by adding the definition of χ in terms of $c_{m,n}$ to the definition of the functional.

Equation 6.17 is solved using a Levenberg-Marquardt minimization algorithm (93; 94; 70). The algorithm has been chosen because it can work with complex numbers and can deal with both under- and over-determined problems. In addition, the algorithm can compute

the gradients necessary to minimize the functional itself, by approximation with the finite-difference method, and does not require user-supplied derivatives in explicit form, which would require cumbersome calculations. The algorithm chosen is implemented in MATLAB as `lsqnonlin`.

The Levenberg-Marquardt minimization algorithm will be given as input an initial guess of the coefficients $c_{m,n}$ (usually the null vector) and will return as output the calculated $c_{m,n}$ which will be translated from Fourier-domain to space-domain using Equation 6.15 for plotting.

Using the harmonic contrast function thus defined, the number of unknown is greatly reduced. In fact, as few as a dozen harmonics can represent sufficiently well real-world objects such as cylinders.

6.2.1 Reconstruction of harmonics by linear and quadratic models

The harmonic representation of the contrast also aids in understanding why the quadratic model can outperform the linear one. The reason lies in the harmonics representation of the linear model itself (76).

The linear model consists in building the operator $\mathbf{A}_{\mathrm{e}}$, which essentially represents a (linear) map from the target space to the scattered electric field space. This mapping operation can be analyzed by looking at the singular value decomposition of $\mathbf{L}$.

In the Truncated Singular Value Decomposition method (described in Section 2.2) generalized eigenvalues with small magnitude have been associated with ill-conditioning, which in turn translates into poor reconstruction quality. To overcome this issue, only k gener-

alized eigenvalues which are larger than a certain user-selected threshold are used, along with the corresponding k columns of the matrices containing left- and right-singular vectors. Therefore, only the k singular vectors which are maintained take part in the image formation. Remembering the definition

$$\mathbf{L} = \mathbf{USV}^H \tag{6.18}$$

it is observed that the matrix $\mathbf{V}$ has as many rows and columns as the number of pixels into which the domain of investigation has been partitioned. This is the matrix of interest, because it spans the target space.

Each column of $\mathbf{V}$ contains as many elements as the number of pixels. Each of these columns can therefore be represented in Fourier space by performing the Discrete Time Fourier Transform, as done when representing the target into Fourier domain.

Since only k columns participate in the process of image formation, an overall Fourier representation of the space spanned by $\mathbf{V}_k$ can be written as

$$\mathbf{S_V}(m,n) = \sum_k |e^{-jk_x X_0} e^{-jk_y Y_0} \mathrm{FFT}(\mathbf{V}_k)(m,n)|, \tag{6.19}$$

where k_x and k_y should not be confused with k and represent the horizontal and vertical spatial frequencies, found as

$$k_x = \frac{2\pi}{dxM}m \tag{6.20}$$

$$k_y = \frac{2\pi}{dyN}n. \tag{6.21}$$

The Fourier representation obtained with Equation 6.19 can be plotted against k_x and k_y. The plot depends on all the variables which affect the linear operator $\mathbf{L}$, i.e. the choice of domain of investigation (through X_0, Y_0, dx and dy), the location of transmitters and receivers, and the frequency of operation (which all affects $\mathbf{L}$ and therefore $\mathbf{V}$ itself).

Increasing the frequency of operation enlarges the domain encompassed by $\mathbf{S_V}$ and the position and number of antennas affect how uniformly and densely the k-space is filled. When imaging a certain target using the linear model, only those harmonics which fall inside the space spanned by $\mathbf{S_V}$ can be correctly reconstructed.

Figure 52 shows two examples of this plot which highlight how $\mathbf{S_V}$ changes when the number and position of antennas is changed. In Figure 52a, 11 transmitters spanning 280° and 20 receivers spanning 360°, operating at 3 GHz are used. In Figure 52b, instead, 15 transmitters spanning 360° and 40 receivers spanning 360°, operating at 6 GHz are used. The image shows that while in the first case spatial frequencies up to $|k_x| = |k_y| = 200$ can be reconstructed, in the second case spatial with $|k_x| = |k_y| > 300$ can be correctly imaged. In addition, the k-space in Figure 52b is a lot fuller than the one in Figure 52a. These

two configurations will be later used in numerical examples which will highlight further this difference.

These plots also explain why the TSVD also has a filtering effect on the reconstructed image: harmonics that are outside the space spanned by $\mathbf{S_V}$ are effectively filtered out, leaving only lower harmonics.

The quadratic model expands the number of harmonics that can be correctly reconstructed. This can be seen from the approximated scattered field equation in the quadratic case. Recalling

$$E^{\mathrm{s}} \approx \mathbf{A}_{\mathrm{e}} \chi E^{\mathrm{i}} + \mathbf{A}_{\mathrm{e}} \left(\chi \mathbf{A}_{\mathrm{i}} \chi E^{\mathrm{i}} \right), \tag{6.22}$$

it is clear that χ contributes to the scattered field not only through $\mathbf{A}_{\mathrm{e}}$ like in the linear model (first term of the equation), but also through the internal operator $\mathbf{A}_{\mathrm{i}}$ (second term of the equation). In practice $\mathbf{A}_{\mathrm{i}}$ operates a transformation to the spatial components of χ before the multiplication by $\mathbf{A}_{\mathrm{e}}$ occurs, i.e. before the spatial components of χ are truncated by $\mathbf{S_V}$.

In the same way as $\mathbf{S_V}$ has been obtained, it is possible to plot a similar k-space, spanned this time by $\mathbf{A}_{\mathrm{i}}$, for the same two scenarios described in Figure 52.

Notice that the internal operator $\mathbf{A}_{\mathrm{i}}$ is only affected by the frequency of operation and not by the position of the antennas. Figure 53 makes it obvious that the k-space spanned

by $\mathbf{A}_\mathrm{i}$ is a lot larger than the one spanned by the linear operator, therefore it affects many more spatial frequencies of χ.

In any case it will be the external operator $\mathbf{A}_\mathrm{e}$ that determines how many spatial frequencies end up actually affecting the scattered electric field. As a result, the fact that $\mathbf{A}_\mathrm{i}$ operates on a larger set of spatial frequencies could have no effect whatsoever, because those would be filtered by $\mathbf{A}_\mathrm{e}$, leading to no advantage. This, however, is not what happens thanks to the specifics of the multiplication of $\mathbf{A}_\mathrm{i}$ and χ.

It can be shown (91; 92) that **the effect of the internal operator is to "beat" high-harmonics of the contrast function into lower harmonics**, much like a modulation effect. This is crucial, because it implies that spatial components that previously were inaccessible now can be reconstructed because they are beat into lower harmonics and therefore are not affected by the filtering effect of the linear operator.

This is the fundamental advantage of the quadratic forward model over the linear model, which has been tested by means of numerical examples.

6.2.2 Method of Moment algorithm to compute the scattered field

Expressing the contrast as a summation of a finite number of harmonics presents a new challenge: the retrieval of the scattered field needed for the inversion. The field can come from two sources: a laboratory measurement or a computer simulation. If the second way is adopted, it is necessary to find a simulator that allows to define smooth, continuous variations of ϵ_r, pixel by pixel. This is not the case in most commercial software. Some educational Finite Difference Time Domain implementation allow complete control over

the domain of investigation, letting the user set the properties of every pixel individually. These routines, however, lack in performance, requiring exceedingly long times to obtain the solution.

Interestingly, a clever solution to this problem lies into the problem itself. The calculation of the scattered electric field from the knowledge of the contrast function is the definition of the forward model. In particular, this very chapter described the exact solution to the forward problem while deriving the formulation of the quadratic model.

Equation 6.5 and Equation 6.6 represent the forward problem in its entirety. The problem is nonlinear when χ must be recovered from the knowledge of E^{s}. However, the problem is much simpler for the computation of E^{s} if χ is known.

The solution is found using the exact same minimization algorithm employed for the retrieval of the contrast function. First, a functional is defined using Equation 6.6:

$$\Psi^{\mathrm{Et}} = \|E^{\mathrm{t}} - E^{\mathrm{i}} - \mathbf{A}_{\mathrm{i}}\chi E^{\mathrm{t}}\|^2. \tag{6.23}$$

Then, Equation 6.23 is minimized with E^{t} as an unknown. The functional defined by Ψ^{Et} is convex in E^{t}, therefore the minimum solution will be found without worrying about local minima.

After E^{t} has been found, the scattered field is given by Equation 6.5.

This method is basically a Method of Moments algorithm. It is therefore accurate when the meshing of the scattering object – in this case, the discretization of the domain under

investigation – is sufficiently small. In virtually all cases, a discretization of $\lambda/15$ or finer proves to be sufficient to obtain the scattered field correctly.

The algorithm just described has been employed to calculate the scattered electric field in all the cases simulated in this chapter.

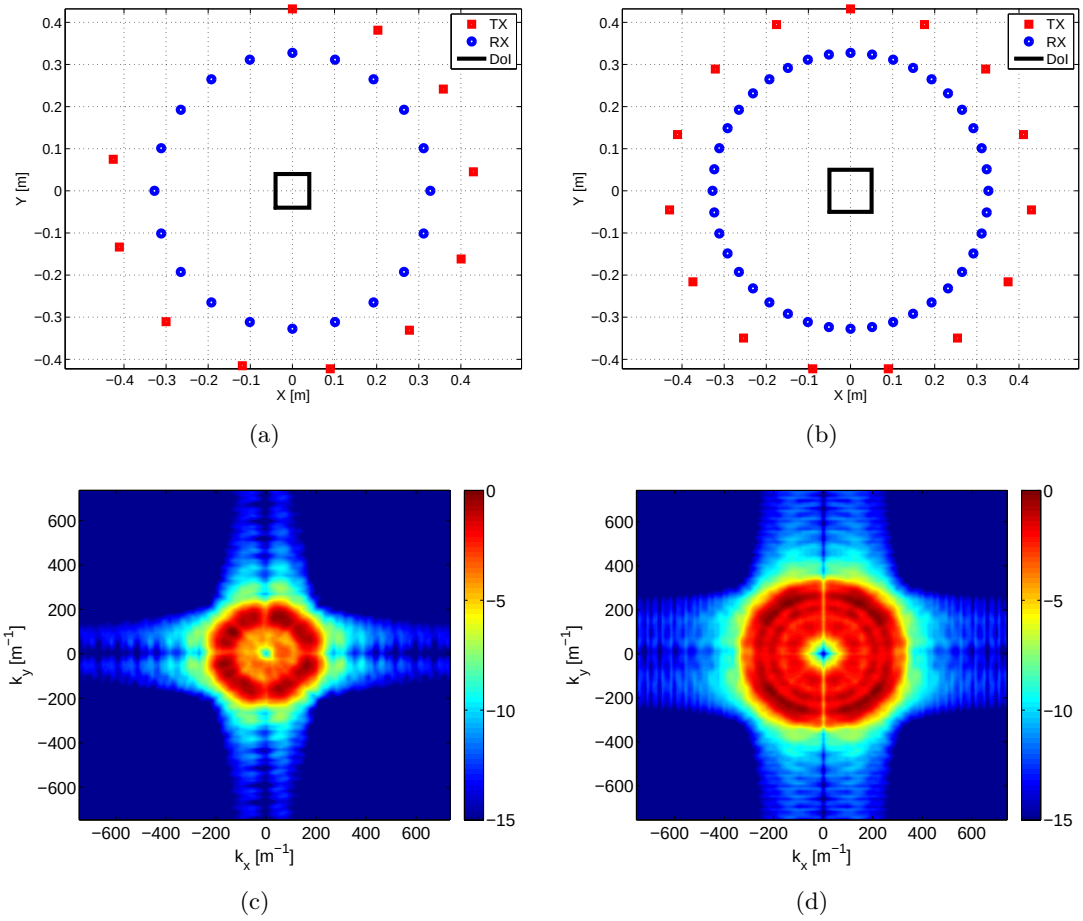

Figure 52. k-space representation of the linear operator $\mathbf{L}$ for two different antennas configurations. (a) 11 TX $(0-280°)$, 20 RX $(0-360°)$ at 3 GHz lead to the k-space shown in (c); (b) 15 TX $(0-360°)$, 20 RX $(0-360°)$ at 6 GHz lead to the k-space shown in (d).

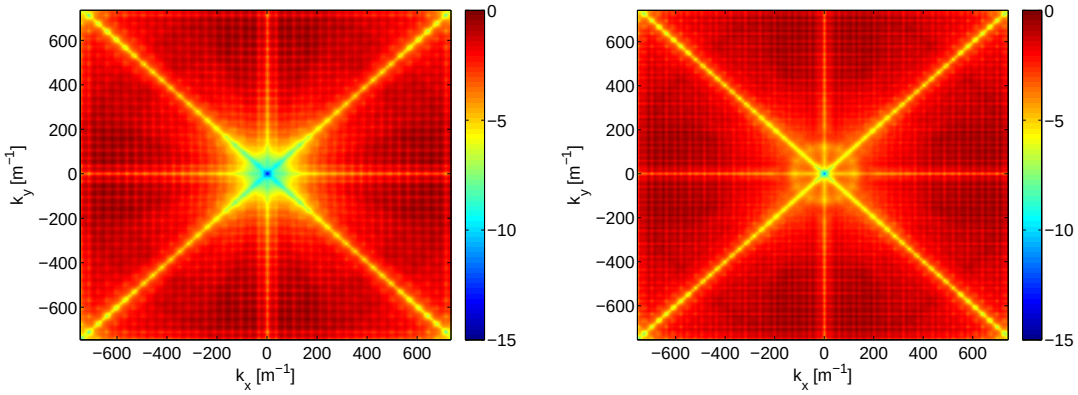

Figure 53. k-space representation of the internal operator $\mathbf{A}_\mathrm{i}$ for two different frequencies: (a) 3 GHz and (b) 6 GHz.

6.3 Inversion

Due to the quadratic nature of the forward model, the inversion has to be thought from scratch. All the methods described in the previous chapters assume to work with a linear system of equations that is expressed as a matrix-vector multiplication. This is not the case anymore.

The most straightforward way to tackle the inversion is to recast it as an optimization problem. Doing that, a variety of tools for solving both linear and non-linear optimization problems becomes available.

First, the problem is expressed as a functional. In this case the functional is immediately written starting from Equation 6.12 as:

$$\Psi^{\text{quad}} = \| E^{\text{s}}(\mathbf{r}^{\text{r}}) - \mathbf{A}_{\text{e}} \left[\chi \mathbf{A}_{\text{i}} \chi E^{\text{i}} \right] \|^2. \tag{6.24}$$

Equation 6.24 is solved using the same Levenberg-Marquardt minimization algorithm employed earlier to calculate the scattered field.

In order to compare the results obtained with the quadratic forward model to the ones obtained with the linear forward model, it is important that the inversion algorithm be the same for both cases. Therefore another functional is defined for the linear problem, and it is

then inverted using the same algorithm and the same parameters adopted for the quadratic model. Namely:

$$\Psi^{\text{lin}} = \|E^{\text{s}}(\mathbf{r}^{\text{r}}) - \mathbf{A}_{\text{e}}\chi E^{\text{i}}\|^2. \tag{6.25}$$

When expressed in matrix form $\mathbf{A}_{\text{i}}$ is much larger than $\mathbf{A}_{\text{e}}$. While $\mathbf{A}_{\text{e}}$, just like $\mathbf{L}$, has as many rows as the number of measurements and as many columns as the number of unknowns, $\mathbf{A}_{\text{i}}$ is square and has as many rows and columns as the number of unknowns (i.e. pixels); it is therefore expected that the minimization of Ψ^{quad} be heavier than the minimization of Ψ^{lin}.

6.4 Numerical results

The procedure detailed in this chapter has been applied to numerical data. In the following, a few examples are used to demonstrate the differences between linear and quadratic forward model in solving the same inversion problem.

6.4.1 Imaging of a dielectric cylinder

In the first test imaging of a dielectric cylinder is attempted. The simulation setup is visualized in Figure 54.

The target is illuminated by 11 transmitters, placed along a circumference of radius $r_t = 43.2$ cm; the transmitters span 280°. The resulting scattered field is sampled by a set of receivers, placed along a circle of radius $r_r = 32.8$ cm; the receivers span all 360°. The target is sampled with a sinusoidal signal of frequency equal to 3 GHz. The

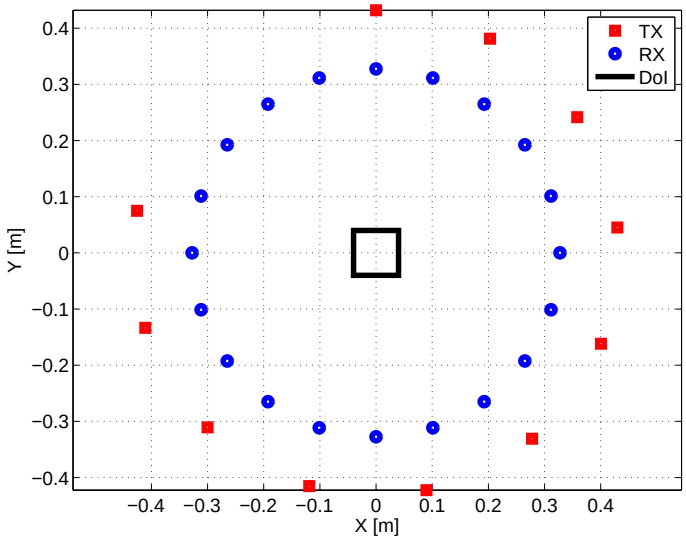

Figure 54. Simulation setup.

number and positions of the antennas simulates a scenario which can be reproduced with the measurement system described in Chapter 3 and Appendix A.

The Domain of Investigation (DoI) is a square of side equal to 8 cm, divided into square pixels of side equal to 4.2 mm, or approximately $\lambda/24$. The total number of pixels is therefore 400.

The target is a cylinder of radius equal to 1.27 cm (1/2 in), and its contrast value is initially set to 0.5 (Figure 55a). The cylinder is located at the origin of the coordinate system. The target is represented using a finite set of harmonics, with $M = N = 9$ (Figure 55b). The finite number of harmonics chosen represents the target with substantially no distortion (Figure 55c). Notice that by choosing a representation with a finite number

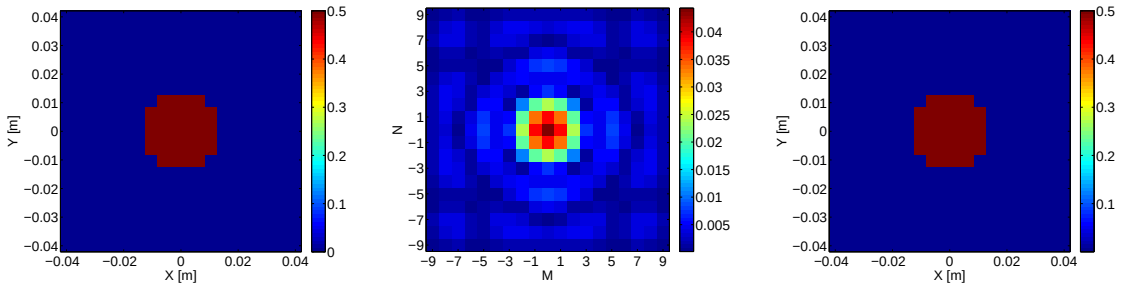

(a) (b) (c)

Figure 55. Target representation: (a) pixel-based, (b) Fourier coefficients, $|c_{m,n}|$ and (c) corresponding pixel representation with only the finite number of coefficients shown in (b).

of coefficients the total number of unknowns of the problem decreases significantly: from 400 pixels to $(2M+1) \times (2N+1)$ in the harmonic representation, where M and N usually are smaller than 7.

From the knowledge of the domain of investigation both external and internal operators can be computed. In addition, the incident field is calculated analytically since the source is the well-known infinite current line in a 2D geometry. Lastly, after creating the target and the domain of investigation, the scattered electric field is computed using the algorithm described in Section 6.2.2.

The scattered field thus calculated is used for the inversion. The main variable when performing the inversion is the number of unknowns (i.e. harmonics) that want to be reconstructed. Due to ill-conditioning and to the approximations given by both the linear and the quadratic models, it is unrealistic to reconstruct all the 10 components which fully represent the target. Therefore, the desired number of harmonics to reconstruct is given as

input to the inversion. The larger the number of Fourier coefficients required, the larger is the size of the problem, and the more both models are put to the test.

As a first test, only $M = N = 2$ harmonics are reconstructed. The result is shown in Figure 56. Since only three harmonics are reconstructed, both the linear and the quadratic model provide good reconstruction results. Due to the very small differences in the reconstruction of the Fourier coefficients, the pixel representation obtained from them is almost identical in the two cases.

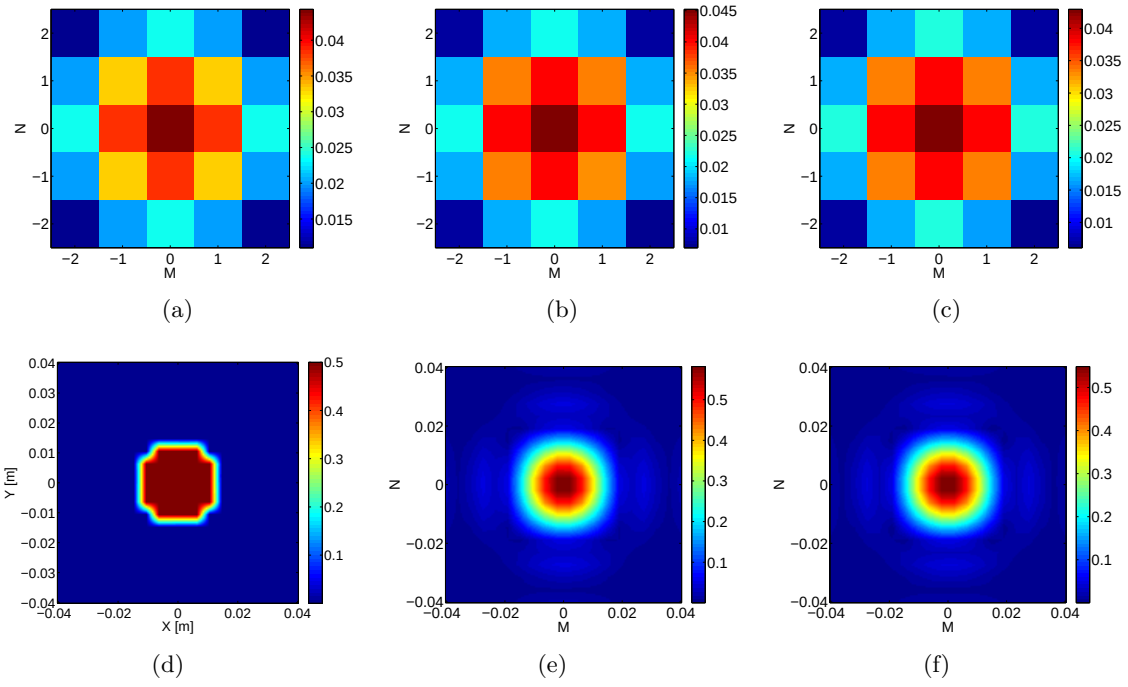

Figure 56. Reconstruction result for $M = N = 2$. (a) True Fourier coefficients $|c_{m,n}|$, (d) True contrast function, (b) and (e) Linear model reconstruction, (c) and (f) Quadratic model reconstruction. The resolution of (d)–(f) has been increased through linear interpolation.

In order to give a quantitative measurement of the differences between the reconstruction obtained using the linear and the quadratic models, the Mean Squared Error (MSE) is computed as:

$$\mathrm{MSE} = \sqrt{\frac{\sum |\chi^{\mathrm{rec}} - \chi^{\mathrm{true}}|^2}{\sum |\chi^{\mathrm{rec}}|^2}}, \tag{6.26}$$

where χ^{rec} and χ^{true} represent the pixel representation of the reconstructed and true contrasts, respectively.

In this first test, the linear model produces an MSE= 0.51838 and the quadratic model an MSE= 0.50058, which represents an improvement of 3.4%.

Additional insight on the quality of the reconstruction can be gained by taking section cut plots of the target, as shown in Figure 57.

The section cuts shows that the absolute value of the contrast is more closely reconstructed by the quadratic model; the linear model tends to over-estimate the peak value. Linear and quadratic models show almost identical side-lobe artifacts.

Increasing the number of Fourier coefficients to reconstruct is possible to stress the differences between linear and quadratic models. In order to give a detailed description of the inversion, the results corresponding to values of M and N ranging from 3 to 7 are shown in Figure 58 through Figure 65

When $M = N = 3$ the performance gap between linear and quadratic models widens, although both models performs overall better than the previous case. The linear models

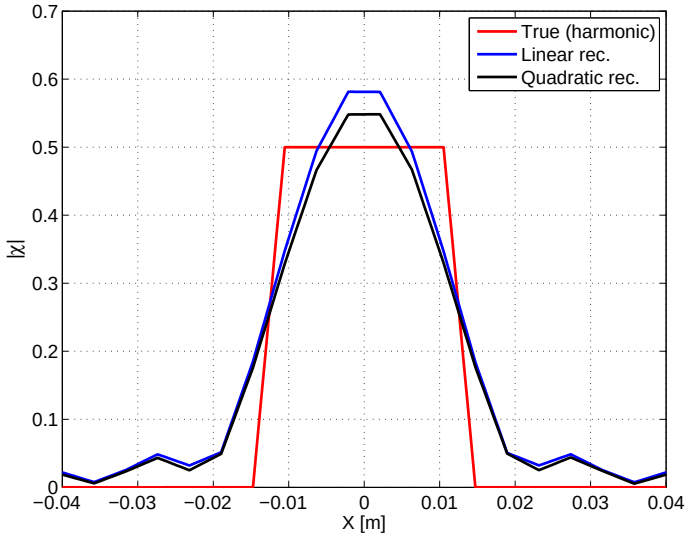

Figure 57. Section cuts of the true and reconstructed targets at $y = 0$ for $M = N = 2$.

produces an MSE= 0.48637, while the quadratic model returns an MSE= 0.43695 (10.2% improvement). Figure 58 summarizes the results. Looking at the plot of the absolute values of the coefficients $c_{m,n}$ for both models there is not a significant difference from the true values. The same applies to the pixel representation.

Figure 59 shows the section cuts. In this case both quadratic and linear models visibly over-estimate the peak value of the contrast function, with the linear model producing the least accurate reconstruction.

When $M = N = 4$ the linear model performs better than the quadratic model. Figure 60 shows that the quadratic model produces high-frequency artifacts that interfere with the true components. In this case MSE= 0.49485 for the linear model. The quadratic model

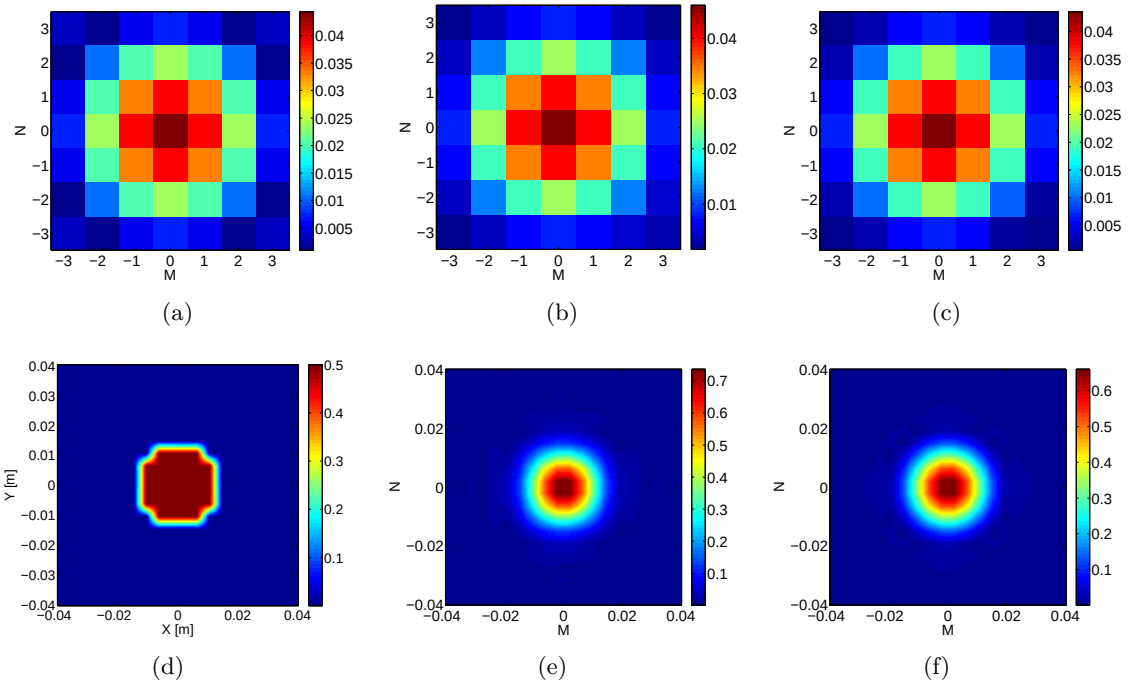

Figure 58. Reconstruction result for $M = N = 3$. (a) True Fourier coefficients $|c_{m,n}|$, (d) True contrast function, (b) and (e) Linear model reconstruction, (c) and (f) Quadratic model reconstruction. The resolution of (d)–(f) has been increased through linear interpolation.

performs worse, with MSE= 0.6793, 37% worse) because the reconstruction is affected by high-frequency components. Looking at the Fourier coefficients plot (Figure 60) it is clear that strong high-frequency artifacts alter the reconstruction, but that the true information contained in the lower spatial frequencies is still preserved.

The section cuts plot (Figure 61) highlights the side-lobe artifacts which affect the quadratic model.

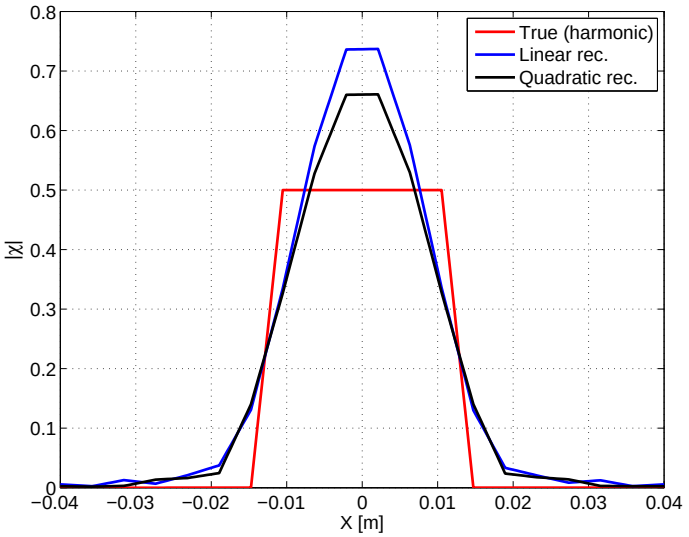

Figure 59. Section cuts of the true and reconstructed targets at $y = 0$ for $M = N = 3$.

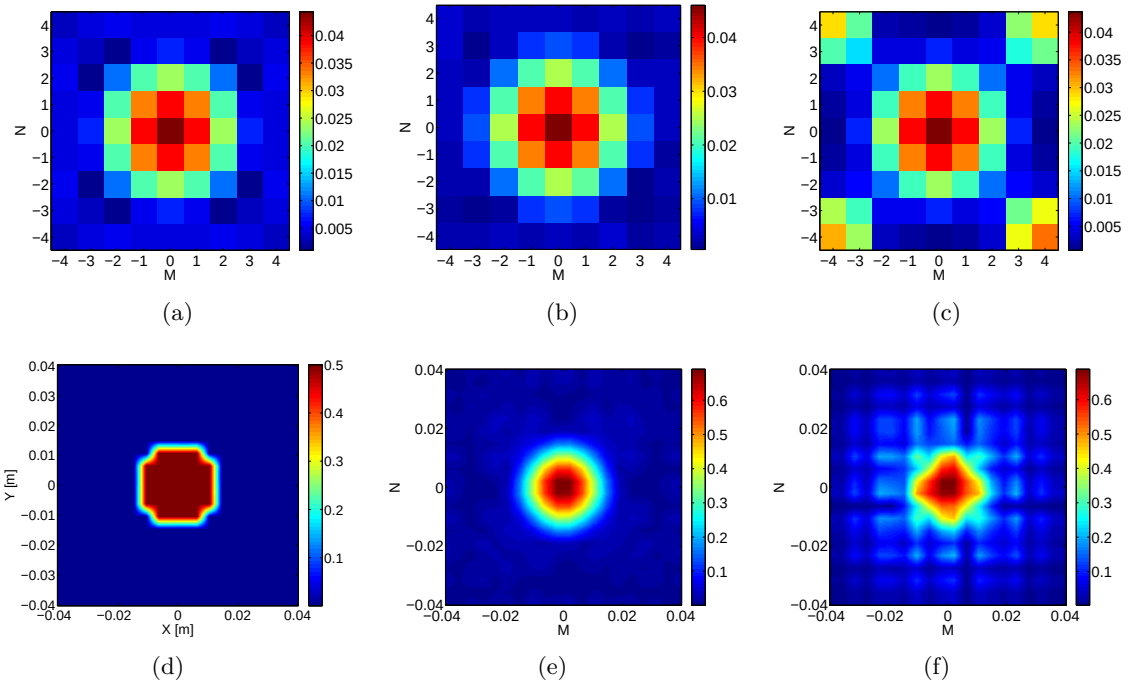

Figure 60. Reconstruction result for $M = N = 4$. (a) True Fourier coefficients $|c_{m,n}|$, (d) True contrast function, (b) and (e) Linear model reconstruction, (c) and (f) Quadratic model reconstruction. The resolution of (d)–(f) has been increased through linear interpolation.

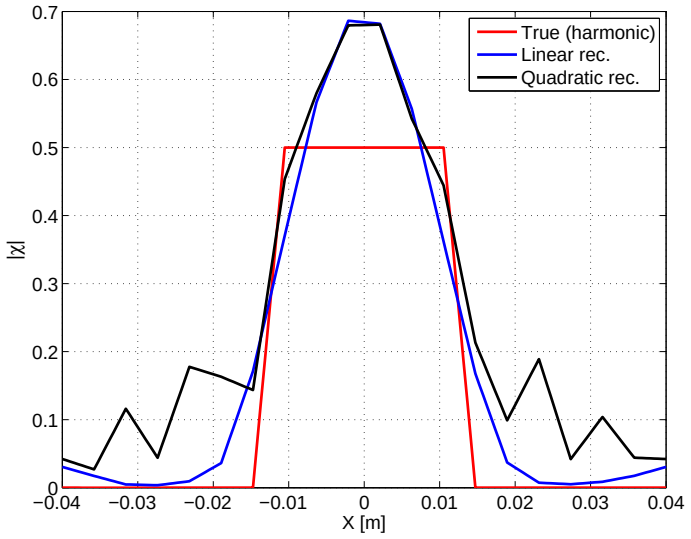

Figure 61. Section cuts of the true and reconstructed targets at $y = 0$ for $M = N = 4$.

The reconstruction with $M = N = 5$ is shown in Figure 62.

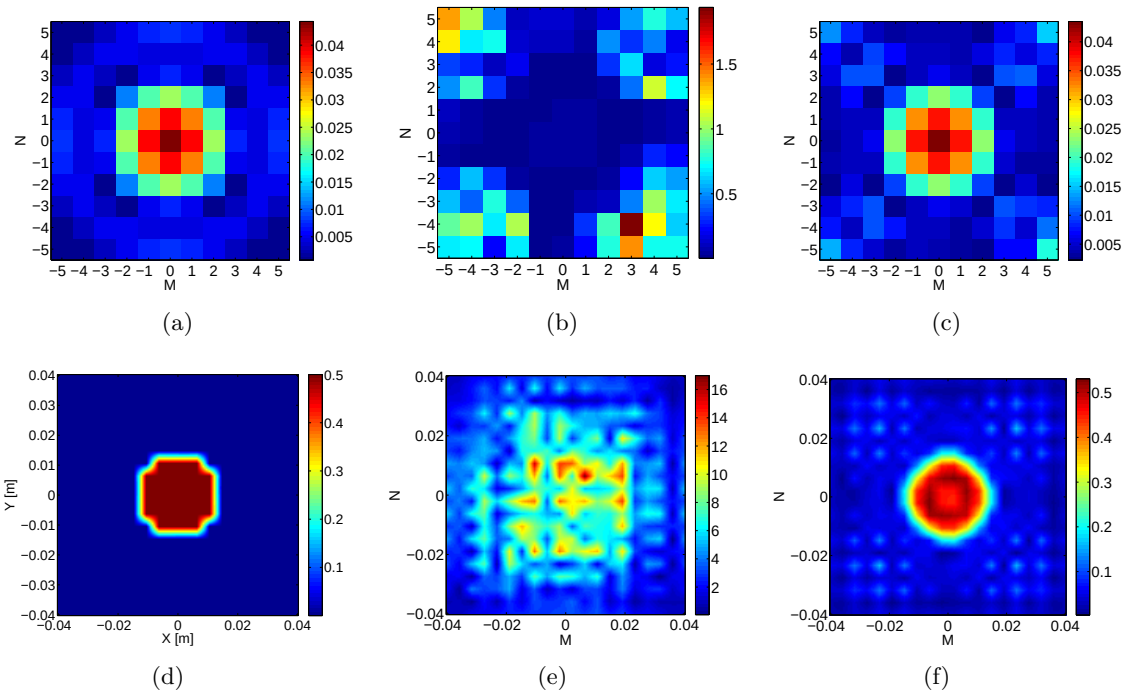

Figure 62. Reconstruction result for $M = N = 5$. (a) True Fourier coefficients $|c_{m,n}|$, (d) True contrast function, (b) and (e) Linear model reconstruction, (c) and (f) Quadratic model reconstruction. The resolution of (d)–(f) has been increased through linear interpolation.

The linear reconstruction is completely disrupted by noise, with the high spatial frequency artifacts completely ruining the reconstruction. The value of MSE= 1.0006 is not very informative, since it is obtained as an overall sum, therefore cannot correctly represent the type of noise observed in the image. The quadratic case, instead, performs better

than the previous case. The high frequency noise is spread over a larger number of pixels, making the reconstruction of the meaningful components more accurate. The MSE for the quadratic case is equal to 0.47866, i.e. improved with respect to the case with $M = N = 4$, but still not as low as when $M = N = 3$. Also in this case, though, the MSE indicator can be misleading, because it hides the fact that the edge of the cylinder is reconstructed with much greater accuracy in this case than in the case with $M = N = 3$.

The section cuts plot (Figure 63a) is not very informative, since the linear model produces artifacts so large that a change of scale would be needed in order to compare linear and quadratic reconstructions. When the scale is adjusted (Figure 63b) it is possible to appreciate the good quality of reconstruction offered by the quadratic model. The comparison of Figure 63b and Figure 59 makes it clear that in this case the cylinder edge is reconstructed with superior accuracy.

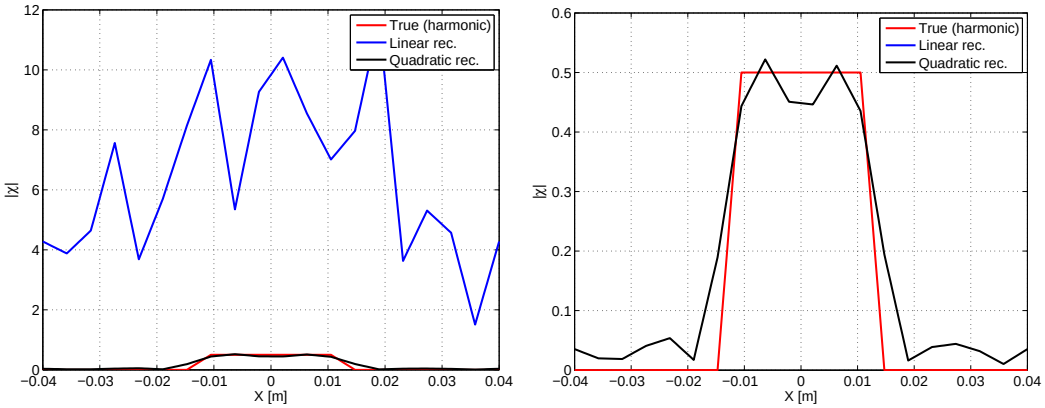

Figure 63. Section cuts of the true and reconstructed targets at $y = 0$ for $M = N = 5$.

Further increasing the number of reconstructed harmonics confirms this trend. The linear model performs extremely poorly for both $M = N = 6$ and $M = N = 7$, while the quadratic model, although more noisy, still produces very good images. The accuracy of reconstruction is evident in the coefficient plots of both Figure 64 and Figure 65, which translate in noisy but substantially accurate pixel representations in both cases. For the quadratic models the MSE is equal to 0.55254 when $M = N = 6$ and 0.55642 when $M = N = 7$.

Importantly, for the quadratic model in all cases the absolute value of the reconstructed contrast is never higher than 0.7 (compared to 0.5 for the representation of the true contrast using 9 harmonics, which has been used to compute the scattered electric field), providing an estimation of the relative dielectric permittivity of the cylinder with sufficiently good approximation.

In the next section the effect of changing the value of the contrast is shown.

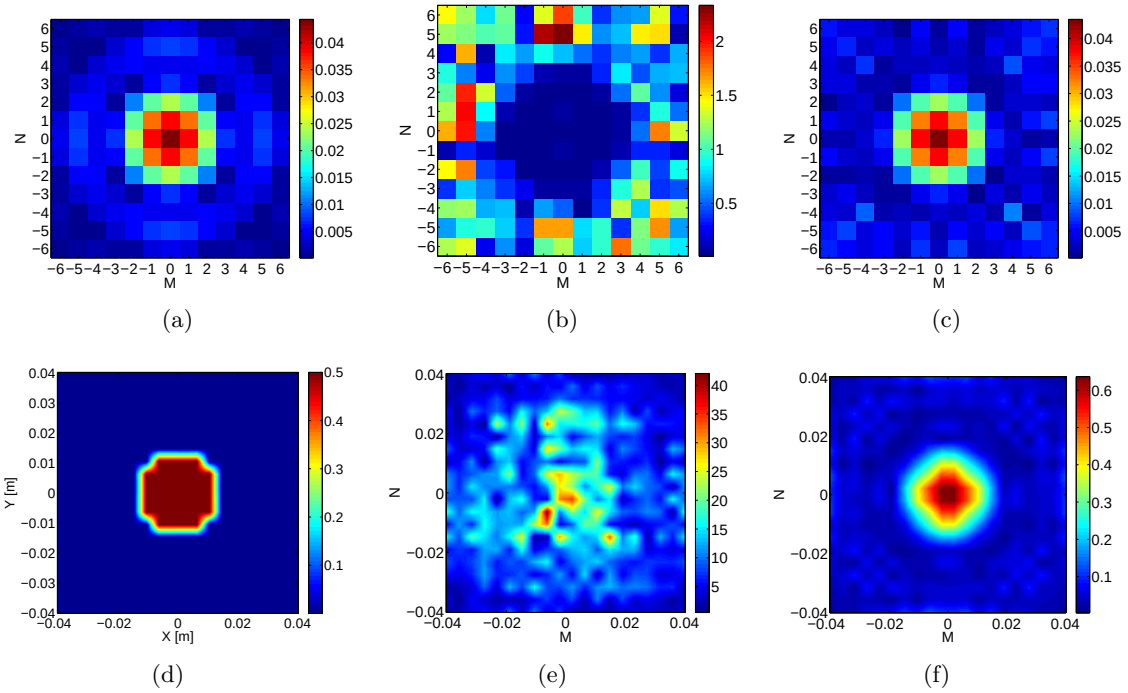

Figure 64. Reconstruction result for $M = N = 6$. (a) True Fourier coefficients $|c_{m,n}|$, (d) True contrast function, (b) and (e) Linear model reconstruction, (c) and (f) Quadratic model reconstruction. The resolution of (d)–(f) has been increased through linear interpolation.

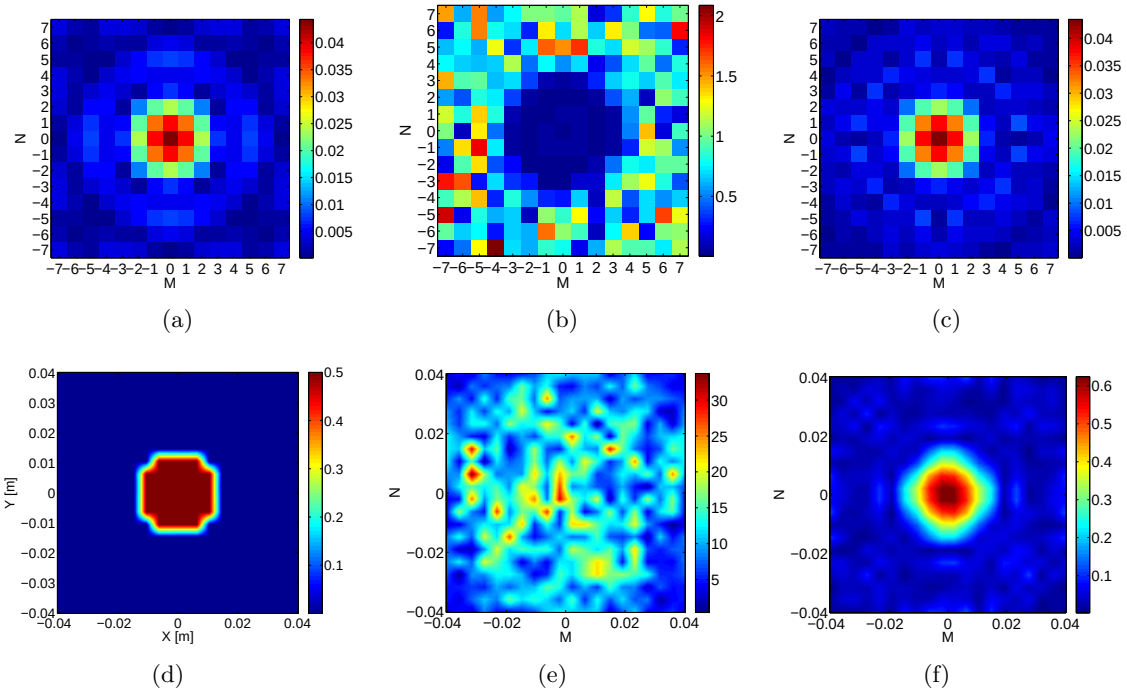

Figure 65. Reconstruction result for $M = N = 7$. (a) True Fourier coefficients $|c_{m,n}|$, (d) True contrast function, (b) and (e) Linear model reconstruction, (c) and (f) Quadratic model reconstruction. The resolution of (d)–(f) has been increased through linear interpolation.

6.4.2 Effect of increasing the contrast value

When the value of the contrast is increased, it is more difficult for the forward model to correctly represent the physics of the problem. In fact, it has been described how both the linear and the quadratic model derive from the assumption that $\|\mathbf{A}_{\mathrm{i}}\chi\| < 1$. While in practice even when this condition is not met, it is often possible to obtain images, there is no guarantee of performance.

Increasing the contrast is important because in real-world conditions a value of dielectric permittivity equal to 1.5, as simulated in the previous section, is not common. Most materials have ϵ_r significantly larger.

In a laboratory environment, under controlled conditions, it is important to operate with well-known materials as targets. This excludes for example wood, whose dielectric permittivity is a function of a large number of variables: tree of origin, water content, age, humidity of the laboratory, local anisotropy due to the grain all play important roles in determining the actual value of permittivity, and are not easily estimated. Most plastics, instead, due to their regular molecular structures, show values of ϵ_r which is well contained between certain known ranges. In addition, most plastics do not show large variations with the frequency of operation, or with local conditions such as humidity. Many plastics found for retail have values of ϵ_r smaller than 3 (95; 96). The values of ϵ_r for some easily acquirable plastics are shown in Table I.

Molecule	**Common Name**	ϵ_r **at 1 GHz**
Fluorinated ethylene-propylene	Teflon FEP	2.05
Polytetrafluoroethylene	Teflon PFA	2.1
Polycaprolactam	Nylon-6	3.0 @ 1 MHz
Polyethyleneterephthalate	PET, Mylar	2.8
Low-Density Polyethylene	LDPE	2.2
High-Density Polyethylene	HDPE	2.3
Polypropylene	PP	2.2
Polyvinylchloride	PVC	2.8

TABLE I

DIELECTRIC PROPERTIES OF SOME PLASTICS.

The actual values for material acquired through retail distributors can show differences, but these are usually not large, due to the very regular nature of these molecules and their well-standardized manufacturing techniques.

After these considerations, it is likely that in most cases a value of ϵ_r no larger than 2.5, corresponding to a contrast of 1.5 in free-space, can be expected. Therefore, the imaging case used in the previous section has been replicated, with the only difference of changing the value of contrast, this time equal to 1.5.

For this case, only the results for some representative values of M and N are chosen, in order to shorten the description.

The imaging result with $M = N = 3$ is represented in Figure 66 and shows that increasing the contrast from 0.5 to 1.5 did not severely affects the reconstruction quality. The linear model performs worse than the quadratic model; both images are not affected

by noise, but they lack resolution due to the low number of harmonics reconstructed. The linear model returns MSE= 0.87711, while the quadratic produces an MSE= 0.61539, which is almost 30% lower (hence better).

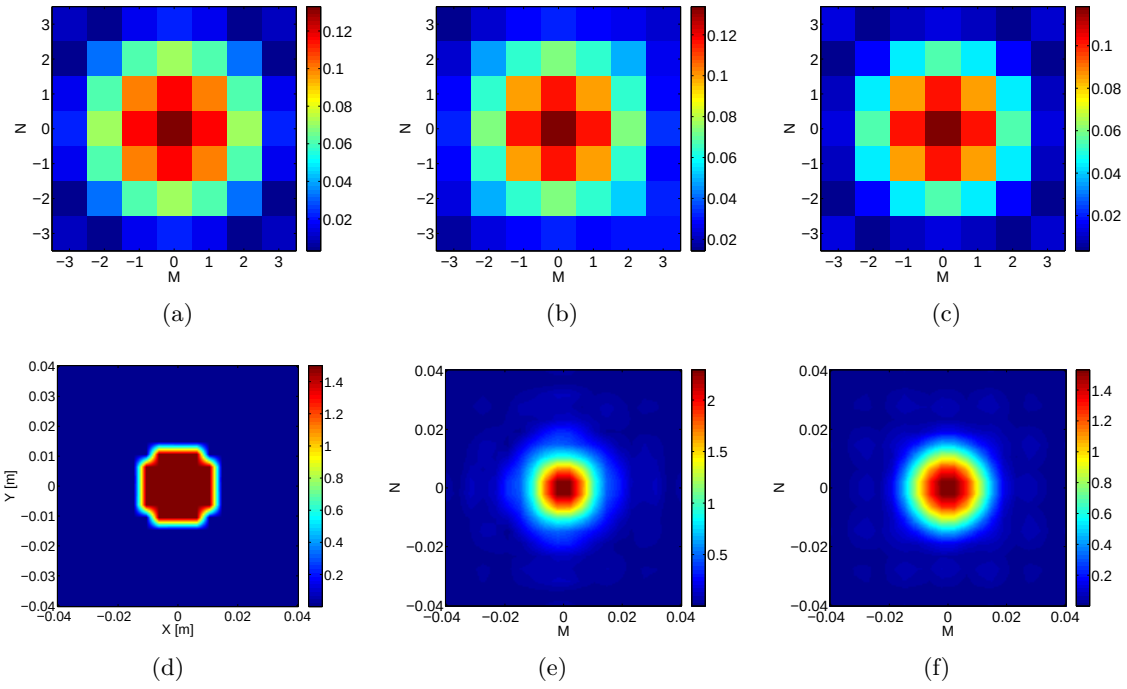

Figure 66. Reconstruction result for $M = N = 3$. (a) True Fourier coefficients $|c_{m,n}|$, (d) True contrast function, (b) and (e) Linear model reconstruction, (c) and (f) Quadratic model reconstruction. The resolution of (d)–(f) has been increased through linear interpolation.

The section cut plot shown in Figure 67 confirms that the quadratic reconstruction, although closer to the peak value of the contrast shows larger side-lobes artifacts.

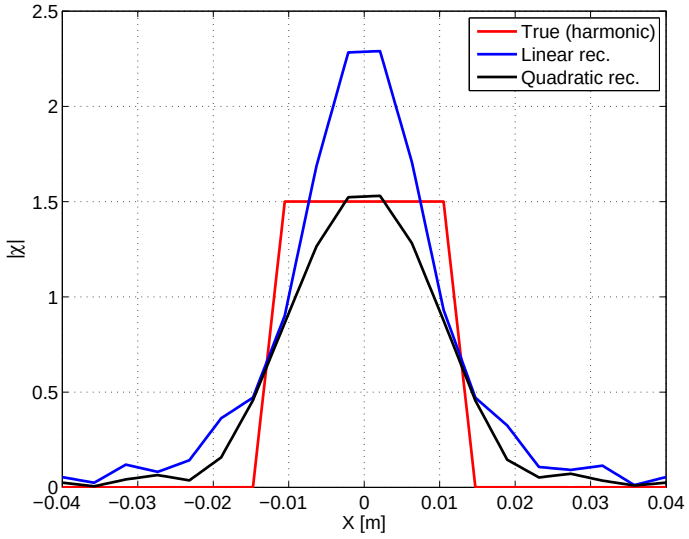

Figure 67. Section cuts of the true and reconstructed targets at $y = 0$ for $M = N = 3$.

Increasing the number of harmonics to $M = N = 5$ makes the linear model fail completely as shown in Figure 68. The quadratic model instead returns a fair image, significantly better than the one produced with the linear model. For the quadratic model MSE= 0.6354 or about 5% worse than the previous case.

The section cut plot is provided in Figure 69. In the figure the linear reconstruction is not visible because it is off-scale by a large amount. The quadratic reconstruction is noisy but correctly follows the outline of the true contrast.

Figure 70 shows the result of the inversion when $M = N = 7$. The linear model still completely fails. The quadratic reconstruction instead does not significantly change. The MSE for the quadratic case is worse, equal to 0.7539. Looking at the reconstruction of the

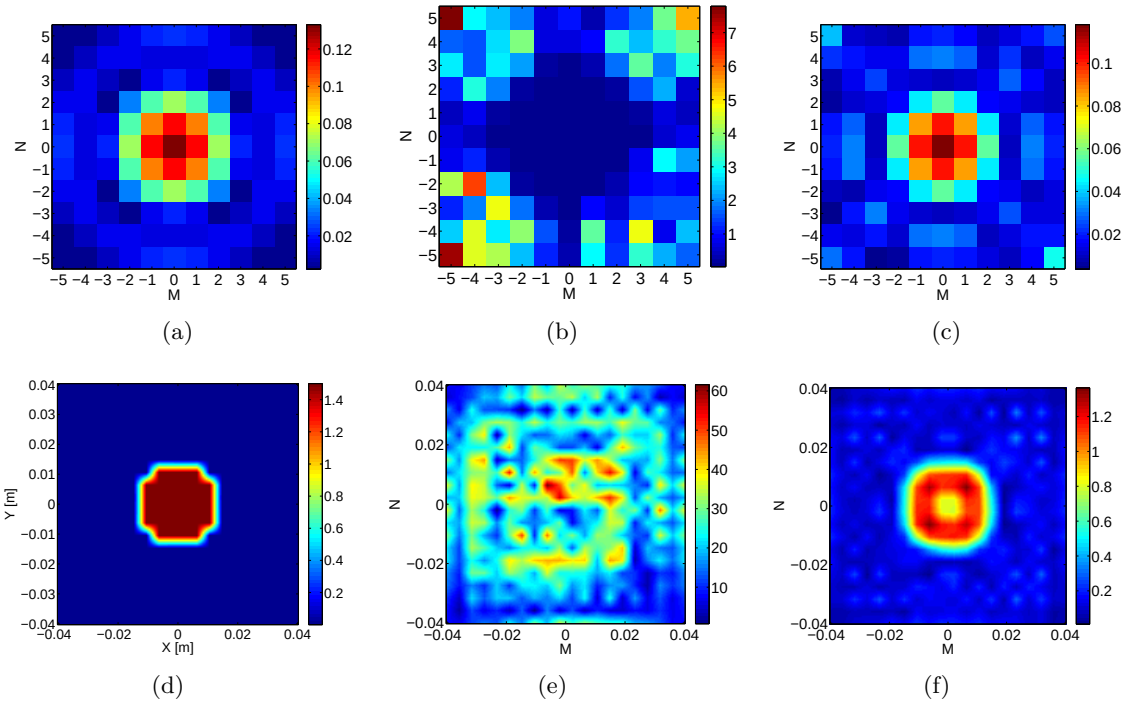

Figure 68. Reconstruction result for $M = N = 5$. (a) True Fourier coefficients $|c_{m,n}|$, (d) True contrast function, (b) and (e) Linear model reconstruction, (c) and (f) Quadratic model reconstruction. The resolution of (d)–(f) has been increased through linear interpolation.

Fourier coefficients (Figure 70c) is is evident that there is some high-frequency noise, but that the main components in the Fourier space are reconstructed correctly.

The section cut shown in Figure 71 has been adjusted by rescaling the vertical axis. The linear reconstruction is not visible because it is much larger than the plot scale. The quadratic reconstruction is very noisy but fairly close to the actual numerical value of the contrast.

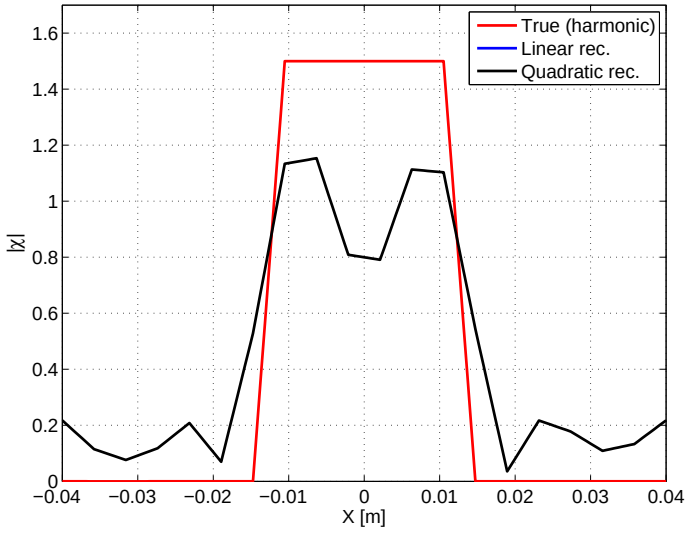

Figure 69. Section cuts of the true and reconstructed targets at $y = 0$ for $M = N = 5$.

In conclusion, increasing the value of the contrast has detrimental effects on the reconstruction. However, even under these difficult conditions, without changing at all the experiment conditions the quadratic model is able to return a solution that is close to the true contrast in terms of absolute of χ, and with fair reconstruction of the Fourier coefficients, which are affected by noise, but not to the point of rendering the reconstruction useless. The linear model instead fails as soon as more than 3 harmonics are requested.

This reconstruction example can be complicated by adding more objects in the domain of investigation, changing significantly the Fourier coefficients that need to be reconstructed.

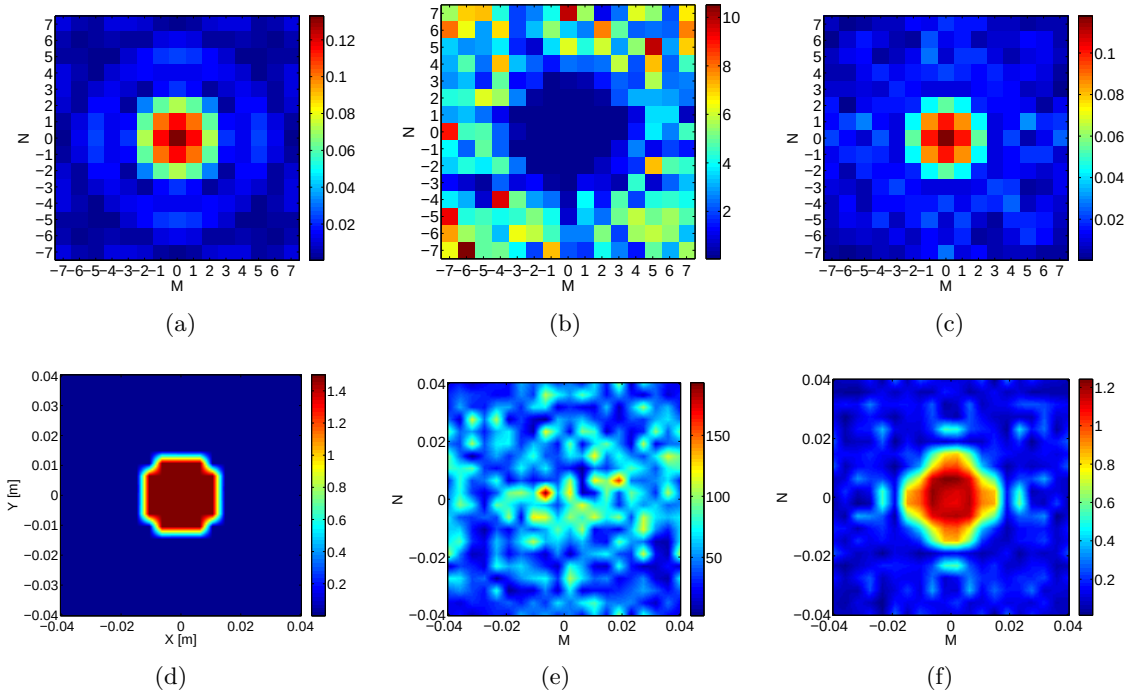

Figure 70. Reconstruction result for $M = N = 7$. (a) True Fourier coefficients $|c_{m,n}|$, (d) True contrast function, (b) and (e) Linear model reconstruction, (c) and (f) Quadratic model reconstruction. The resolution of (d)–(f) has been increased through linear interpolation.

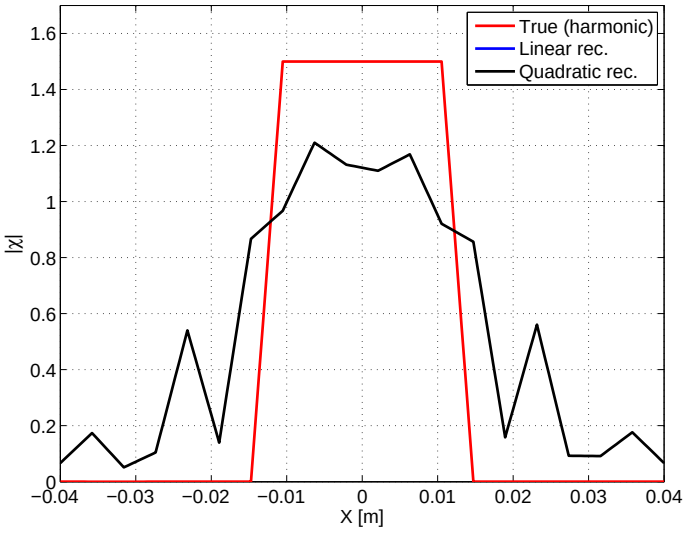

Figure 71. Section cuts of the true and reconstructed targets at $y = 0$ for $M = N = 7$.

6.4.3 Imaging of two dielectric cylinders

In this section imaging of two dielectric cylinders is studied. Two cylinders of radius 0.95 cm (diameter 3/4 in) are placed at a distance of 3.4 cm from each other along the x axis. The distance is measured with respect to the centers of the two cylinders and corresponds to a separation of 1.5 cm measured from edge to edge of the cylinders. The targets are represents with $M = N = 24$ and their dielectric constant is set to 2.5 (i.e. $\chi = 1.5$) as in the latest example. The targets are shown in Figure 72.

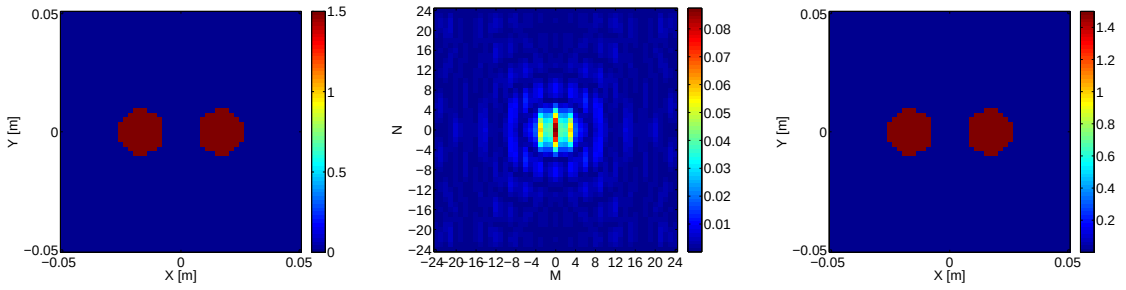

(a) (b) (c)

Figure 72. Target representation: (a) pixel-based, (b) Fourier coefficients, $|c_{m,n}|$ and (c) corresponding pixel representation with only the finite number of coefficients shown in (b).

This setup is more difficult to image than the previous one. The smaller targets mean that more harmonics are significantly different from zero and the presence of two targets

close to each other causes mutual interaction phenomena. For this reason, the antenna setup has been changed.

The antenna setup is shown in Figure 73. 15 TX and 40 RX are employed, operating at 4.5 GHz ($\lambda \approx 6.7$ cm). The domain of investigation is a square of side 10 cm. The pixel size has been decreased to 2 mm ($\approx \lambda/33$). The reason for a smaller pixel size has been dictated by simple visual reasons: the targets employed in this case are small, so that large pixels would have made cylinders appear as squares. From an electromagnetic point of view, however, there is no need to choose such a small pixel size; the electric field can be computed with reasonable accuracy using pixels of side equal to 6 mm as before.

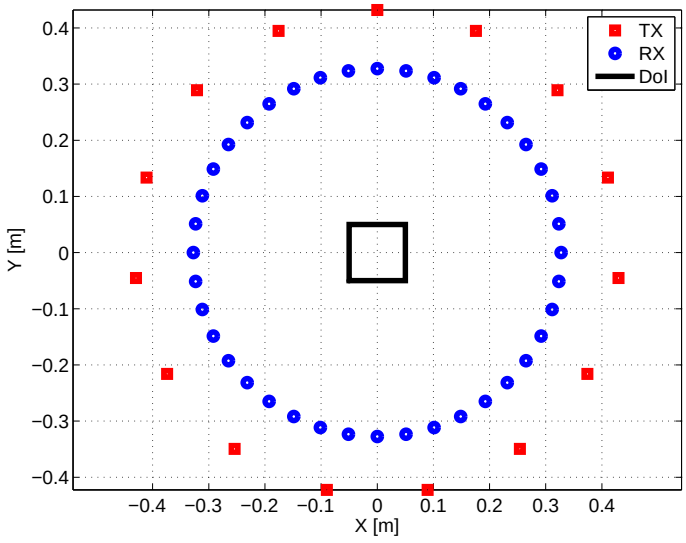

Figure 73. Simulation setup.

The result of the reconstruction setting $M = N = 3$ is shown in Figure 74. The result shows that the quadratic model is superior to the linear one. The image is less noisy and shows no artifact between the two cylinders. For the linear model the MSE is equal to 1.1735, while for the quadratic model MSE= 0.87538, a 24% improvement.

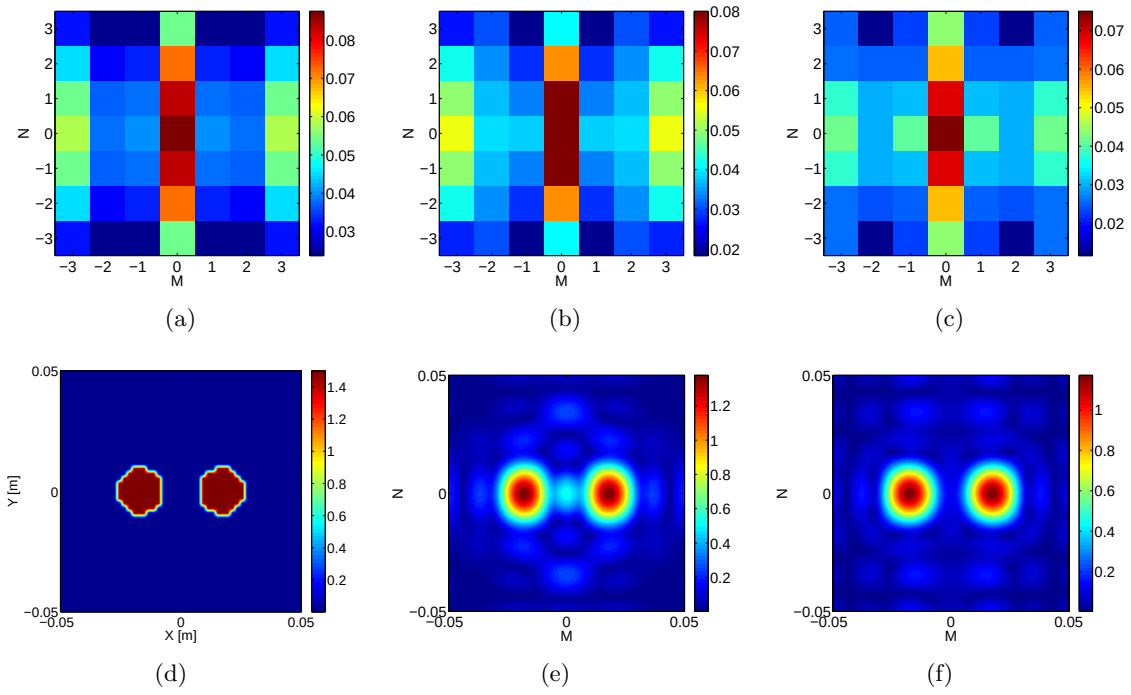

Figure 74. Reconstruction result for $M = N = 3$. (a) True Fourier coefficients $|c_{m,n}|$, (d) True contrast function, (b) and (e) Linear model reconstruction, (c) and (f) Quadratic model reconstruction. The resolution of (d)–(f) has been increased through linear interpolation.

The section cut shown in Figure 75 highlights this difference. Although the linear model approximates more closely the peak value of the contrast, the quadratic model produces reduced side-lobes artifacts as well as no artifact between the two targets.

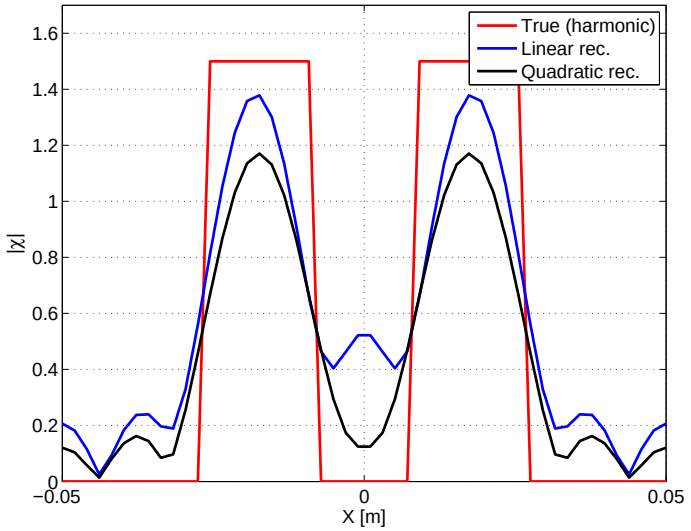

Figure 75. Section cuts of the true and reconstructed targets at $y = 0$ for $M = N = 3$ at 4.5 GHz.

The fact that imaging is more difficult is highlighted by the fact that both methods fail when reconstruction of just one more harmonic ($M = N = 4$) is attempted. Figure 76 shows that both methods introduce very large noise in high-frequency components that completely disrupt the final reconstruction.

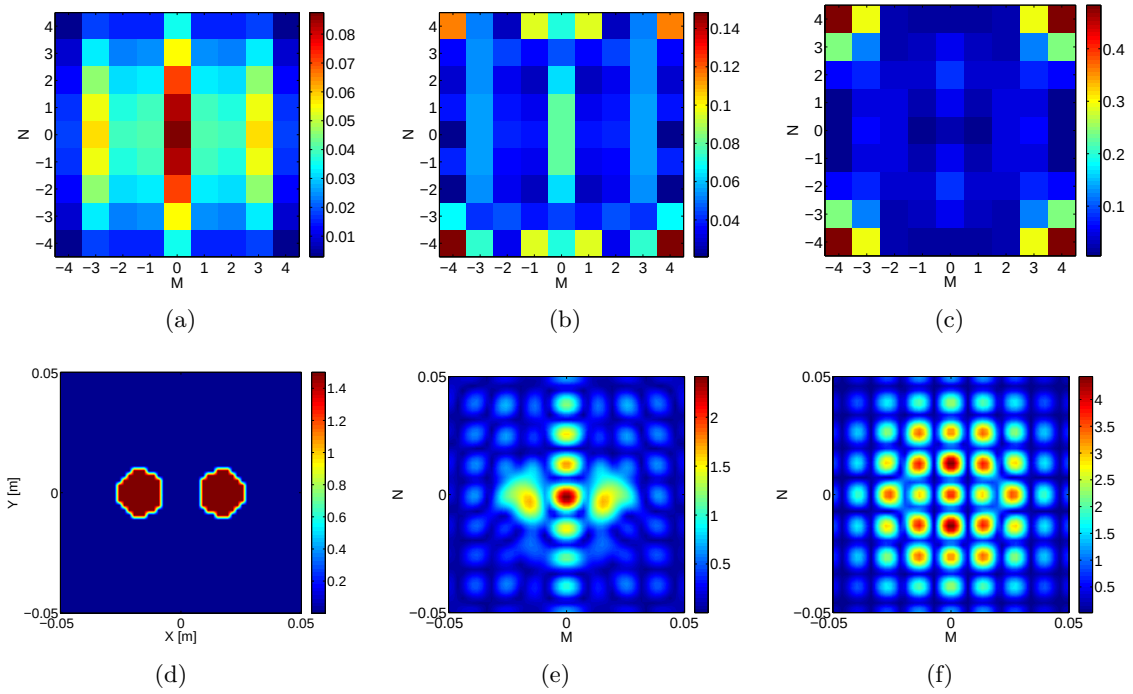

Figure 76. Reconstruction result for $M = N = 4$. (a) True Fourier coefficients $|c_{m,n}|$, (d) True contrast function, (b) and (e) Linear model reconstruction, (c) and (f) Quadratic model reconstruction. The resolution of (d)–(f) has been increased through linear interpolation.

In order to overcome this difficulty the frequency of operation is increased. This means that for both linear and quadratic models the set of spatial frequencies that fall into the reconstructible domain is enlarged. However, the quadratic model is still expected to outperform the linear model, because of its superior ability to reconstruct higher spatial harmonics.

The simulation is performed again, with the only change of increasing the frequency from 4.5 GHz to 6 GHz. The result of the inversion is shown in Figure 77.

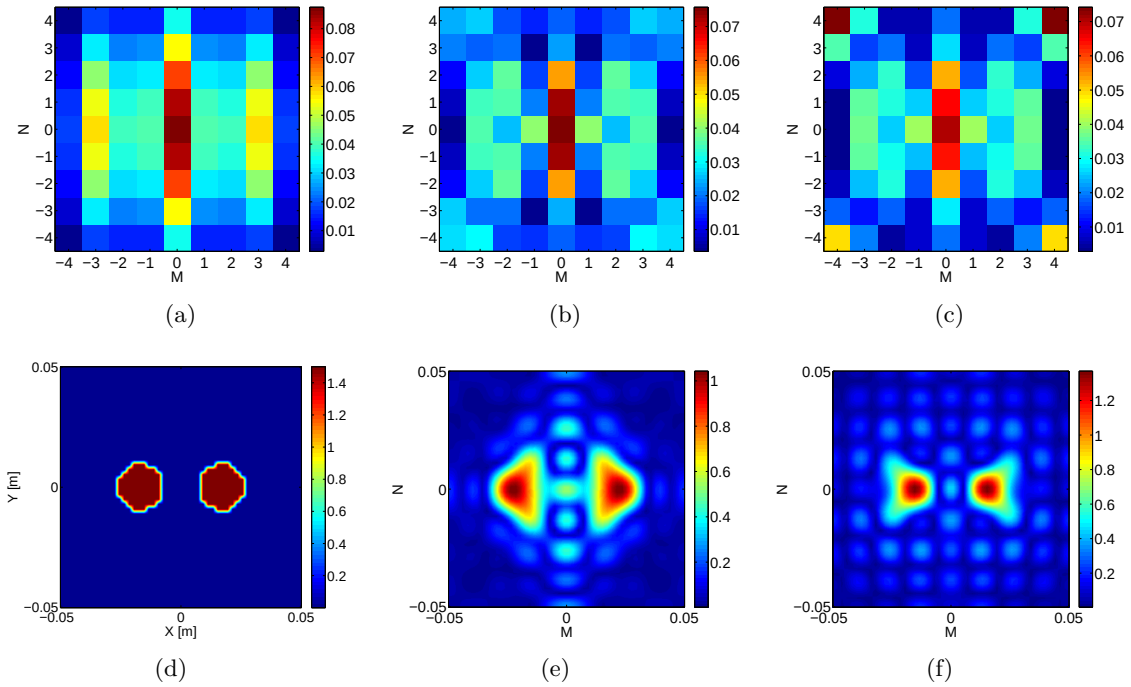

Figure 77. Reconstruction result for $M = N = 4$ at 6 GHz. (a) True Fourier coefficients $|c_{m,n}|$, (d) True contrast function, (b) and (e) Linear model reconstruction, (c) and (f) Quadratic model reconstruction. The resolution of (d)–(f) has been increased through linear interpolation.

In this case, although both models are noisy, the quadratic model clearly outperforms the linear one. For the linear model periodic artifacts are created between the two objects and the shape of the targets is not correctly reconstructed. In this case MSE= 1.3636 and the peak value of the contrast is estimated to be around 1, instead of the expected 1.5.

For the quadratic model, instead, MSE= 0.91725, i.e. almost 33% better. Periodic noise still affects the reconstruction, but the shape and size of the targets can be more correctly inferred. In addition, the peak value of the contrast is estimated to be around 1.4, a significantly better estimation than the linear case. These considerations are all made very clear in the section cuts depicted in Figure 78.

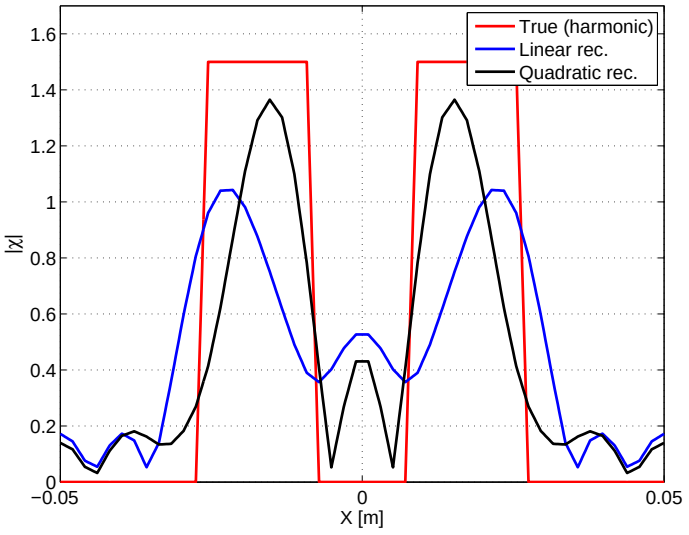

Figure 78. Section cuts of the true and reconstructed targets at $y = 0$ for $M = N = 4$ at 6 GHz.

CHAPTER 7

CONCLUSION

This dissertation presented numerous results related to Radio Frequency Tomography.

Chapter 1 introduced the imaging problem and then focused on electromagnetic methods to provide the foundation for the following chapters.

Chapter 2 described in more detail RF Tomography: it presented its forward model and current inversion algorithms commonly used, as well as discussed some of their limitations. In particular, it was discussed how RF Tomography is based on a linear forward model, which is used to reconstruct a scalar contrast function by using regularized direct inversion methods.

In **Chapter 3** a system used for the experimental validation of RF Tomography has been presented. The system has been entirely designed and built at the University of Illinois at Chicago, in the Andrew Electromagnetics Laboratory. The system has been used to collect all the data presented in the dissertation. The mechanical and electrical characteristics of the systems were described, along with data collection and processing methods.

Chapter 4 proposes two iterative algorithms to perform the inversion, as an alternative to the direct regularization methods typically used and described in Chapter 2. The first method is an implementation of the Conjugate Gradient algorithm, modified so as to introduce physical bounds on the solution and with a customized stopping rule. The developed algorithm performs as well as the Truncated Singular Value Decomposition (TSVD) in

terms of quality of reconstruction, but drastically reduces the memory and computational requirements for the inversion. When used to reconstruct dielectric and metallic targets it performs better than TSVD.

The second algorithm described is based on the Algebraic Reconstruction Technique. This iterative method also provides the ability to introduce physical bounds as well as using a customized stopping rule. In addition to this, the introduction of a regularization parameter for better controlling the algorithm output has been discussed. The algorithm is particularly efficient in reducing noise and in differentiating between metallic and dielectric targets. Its computational cost has been found to be much lower than TSVD but higher than the Conjugate Gradient-based method.

Chapter 5 introduced a modification to the forward model, by replacing the scalar contrast function with a dyadic one. The goal of this modification is to retrieve additional information from the data collected by simulation or measurement pertaining to thin and elongated scatterers. The approach is backed up by a rigorous analytical explanation. The additional information retrieved by using the dyadic contrast function is used to reconstruct the orientation of the thin cylindrical scatterers in a three-dimensional space. The modification of the forward model increases the size of the inversion problem by a factor of 9, which translates into higher memory usage. However, using the Conjugate Gradient-based algorithm developed in Chapter 4, the inversion remains extremely quick.

The data obtained from the inversion can be displayed in two ways. In the first method a set of 3-by-3 plots of the magnitude and phase of the dyadic contrast function is adopted.

The method is successful in presenting the result and in understanding the spatial orientation of the targets, but it is prone to ambiguity in certain particular situations. To solve the ambiguity a second method, based on the eigen-decomposition of the dyadic contrast function is developed. This method allows to display the contrast as a three-dimensional quiver plot, removing any ambiguity in the data interpretation.

Lastly, **Chapter 6** is concerned with a different modification of the forward model, which involves again a scalar contrast function. Retracing the steps that led to the derivation of the formulation of RF Tomography, the approximation which resulted in a linear formulation of the forward model is analyzed. Under favorable conditions, this approximation can be improved, by addition of a quadratic term. The new forward model thus obtained is significantly more complex than its linear counterpart but can provide advantages in terms of quality of reconstruction.

It is shown that the linear model works as a low-pass filter on the data, limiting the number of spatial frequencies of the contrast function which can be reconstructed. The quadratic formulation is showed to perform better than the linear one because it allows reconstruction of additional spatial harmonics. In addition, the scalar contrast function has been changed from a pixel-based to a Fourier-based representation. This allowed on the one hand to reduce the unknowns of the inversion problem and on the other hand to more closely control the number of spatial harmonics being reconstructed. In order to produce scattered electric field data from harmonic contrasts a custom Method of Moment method has been employed.

A Levenberg-Marquardt optimization algorithm has been employed to invert the quadratic model and reconstruct the contrast function. To provide unbiased comparison of the results, the same algorithm has been applied on the linear model as well. The quadratic model is shown to outperform the linear model in a set of test cases involving different targets and measurement conditions.

APPENDICES

Appendix A

DETAILS OF ANTENNA POSITIONING SYSTEM

This postioner was designed to mount 2 dipole antennas and allows for automated movement of the antennas to speed up network analyzer measurements of objects used in Radio Frequency Tomography. It was decided for ease of construction to have the antennas placed on swing arms which would move about a central point that will hold an object to be measured. In addition, the antennas were mounted far enough above the swing arms to minimize reflections and far enough from one another to prevent mutual coupling. The last major design consideration was material. Plexiglas was chosen for its strength, durability, easy of construction, and low dielectric constant ($\varepsilon_r \approx 2.6$). Ideally, a dielectric constant equal to the one of air is preferable.

Figure 79 illustrates the initial design of the positioner; the motors, timing belts, and antennas are not shown. The unit is mounted on a wooden platform with adjustable feet to level the unit. The swing arms allow for adjustable distance from the center of the unit. As well, the antennas (not shown) have the ability to change height. Located around the central shaft and below each swing arm is a timing pulley operated by a DC stepper motor controlled via computer and a LabVIEW program. Once all details of the initial design were finalized, construction began.

Plexiglas with a thickness of 0.354 inches was chosen as a strong enough and inexpensive material. Cutting, milling or machining of the material is somewhat difficult and was done

Appendix A (Continued)

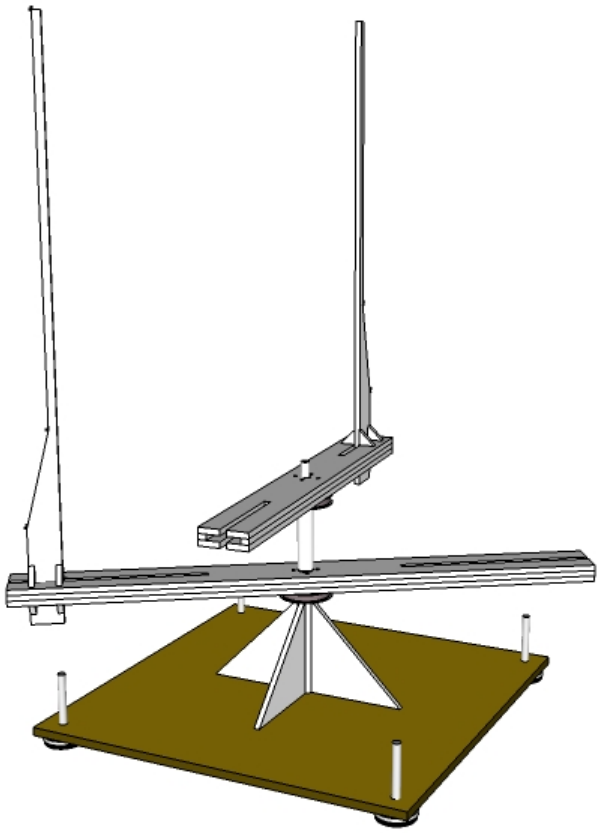

Figure 79. 3D model of antennas positioner

by the University of Illinois at Chicago skilled machinists. Once all parts and materials were available and present, the next step was construction. Unlike metal or wood, Plexiglas can be glued together and form a bond that is equal in strength to the material itself. This further cuts down on connection hardware like screws, nuts, and bolts. The one drawback is time as the glue takes 2 days to reach full strength in bonding. As well, when gluing pieces

Appendix A (Continued)

together time was taken to ensure proper alignment of crucial pieces. The construction went nicely, without any major set backs, but a lot of minor problems to overcome. Figure 80 is a picture of the finished project.

Figure 80. Photo of finished antenna positioner

Appendix A (Continued)

Some problems were noted during construction. The swing arms were initially designed to be longer to allow for counter balancing. This was believed to be an issue when the strength of the Plexiglas and design were in question. Once everything was assembled and weight testing of the swing arms conducted, the design proved to be strong enough to eliminate the need for a counter balance. This allows for a greater range of movement as the lower swing arms movement is limited by the upper swing arm's motor and placement. The movement range was increased by using a longer timing belt. In the end the lower swing arm has a range of 285 degrees and the upper swing arm of 360 degrees. Figure 81 shows the system installed in the anechoic chamber.

After installation of the system, care was taken to connect the antennas and the network analyzer cabling. Because the positioner moves, so does the cabling. The cables were ran in such a way as to allow for maximum movement while not binding up in the mechanics or due to the motion of the system. This is an issue which needs to be noted and remembered before moving the system. It is recommended that the user checks for any material (cable or otherwise) which may obstruct the systems motion prior to and/or after making any large number of movements. This is not a grave or system failure issue. If the positioner is obstructed while attempting a computer controlled movement, the timing belts may become damaged. As well, all data will be unusable as the exact angular position will not be known. To eliminate this issue, an encoder may be installed (in the future) on each swing arm pulley to provide some haptic feedback to the user.

Appendix A (Continued)

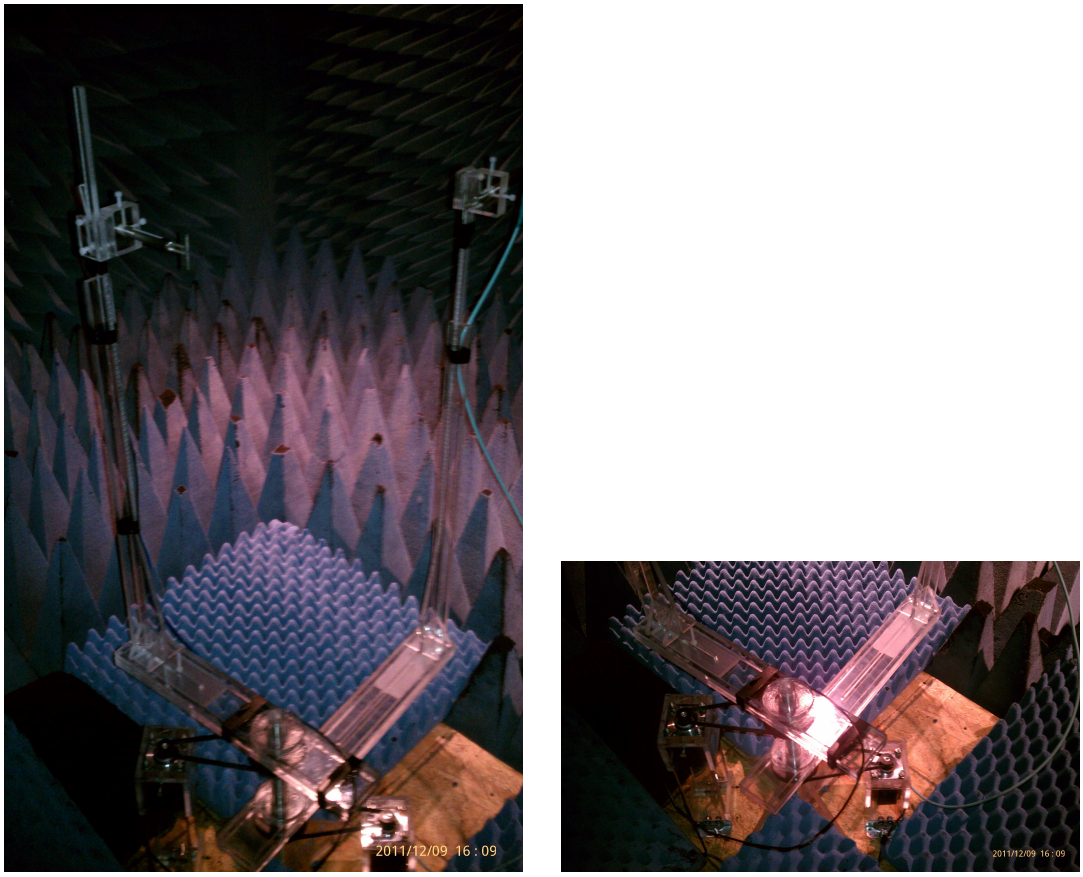

(a) (b)

Figure 81. Photos of finished antenna positioner in the anechoic chamber

Appendix A (Continued)

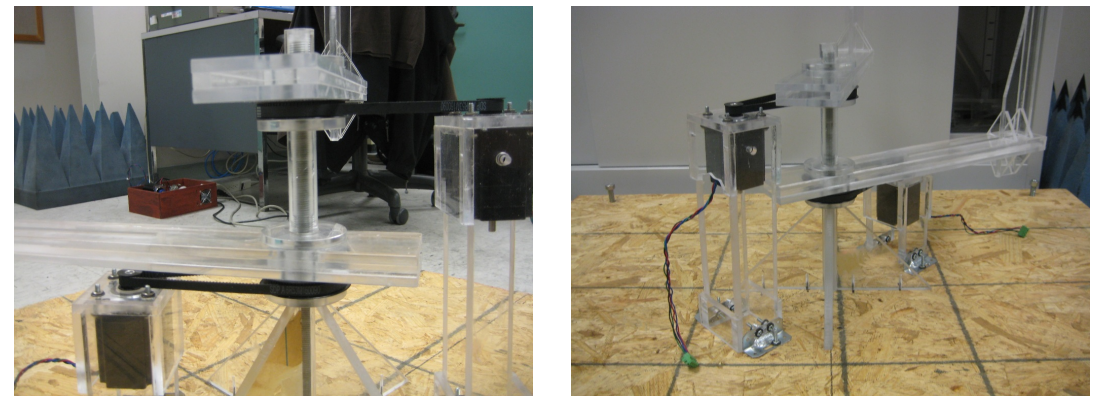

(a) (b)

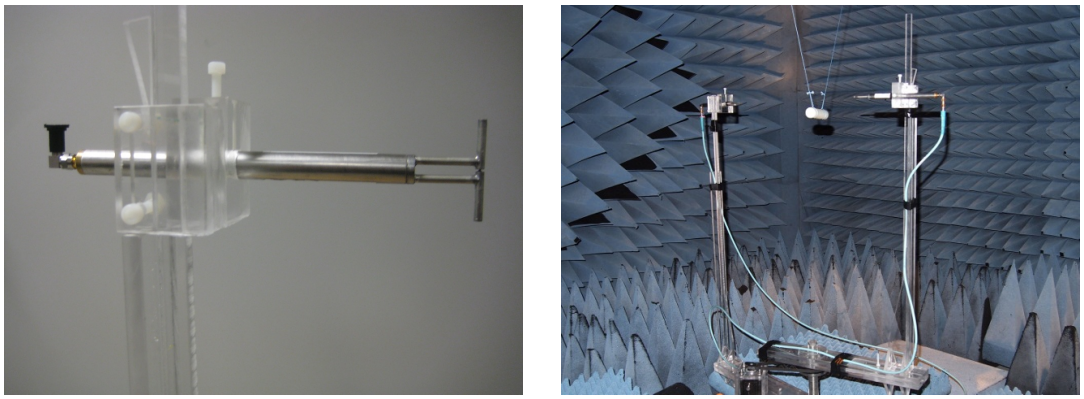

(c) (d)

Figure 82. Details of the positioner showing (a) the motors, pulleys and belt system, (b) motor mounts, (c) dipole antenna in its holder adjustable in height, and (d) overview of the final system in action, with a target in the scene.

Appendix B

CONCISE DERIVATION OF THE RF TOMOGRAPHY FORWARD MODEL

The derivation follows the procedure described in (10).

Consider the vector wave equation in a source-free medium:

$$\nabla \times \nabla \times \mathbf{E}^{\mathrm{i}}(\mathbf{r}') = \nabla\nabla \cdot \mathbf{E}^{\mathrm{i}}(\mathbf{r}') - \nabla^2 \mathbf{E}^{\mathrm{i}}(\mathbf{r}') = k_0^2 . \mathbf{E}^{\mathrm{i}}(\mathbf{r}') \tag{B.1}$$

Since in a source-free medium $\nabla \cdot \mathbf{E}^{\mathrm{i}} = 0$, the Helmholtz equation is obtained:

$$\left(\nabla^2 + k_0^2\right) \mathbf{E}^{\mathrm{i}}(\mathbf{r}') = 0. \tag{B.2}$$

If the incident field $\mathbf{E}^{\mathrm{i}}$ encounters an obstacle v, a scattered field is generated. The total field in the space will be given by the summation of incident and scattered fields. The scattered components can be ideally thought of as if it were generated by an equivalent current source $\mathbf{J}$ on the surface of the scatterer, found as:

$$\mathbf{J} = \mathbf{E}^{\mathrm{t}} v, \tag{B.3}$$

Appendix B (Continued)

with

$$v = [\varepsilon - \varepsilon_b] - j\left[\frac{\sigma - \sigma_b}{2\pi f \varepsilon_0}\right]. \tag{B.4}$$

where the symbols with the subscript b identify the properties of the background medium, and the symbols without subscript the ones of the scatterer.

To know the scattered field the Green's function can be introduced. In a 3D geometry, the dyadic Green's function for the system is defined by placing a Dirac's delta current distribution at location $\mathbf{r}''$:

$$\nabla \times \nabla \times \mathbf{G}(\mathbf{r}', \mathbf{r}'') - k_0^2 \mathbf{G}(\mathbf{r}', \mathbf{r}'') = \mathbf{I}\delta(\mathbf{r}' - \mathbf{r}''). \tag{B.5}$$

If the Green's function is known, the scattered field at $\mathbf{r}'$ can be written as a spatial convolution of the equivalent scattering source and of the Green's function:

$$\mathbf{E}^{\mathrm{s}}(\mathbf{r}') = k_0^2 \iiint_D \mathbf{G}(\mathbf{r}', \mathbf{r}'') \cdot \left[\mathbf{E}^{\mathrm{t}}(\mathbf{r}'') v(\mathbf{r}'')\right] d\mathbf{r}'', \tag{B.6}$$

where the dyadic Green's function for an unbounded homogeneous space is

$$\mathbf{G}(\mathbf{r}', \mathbf{r}'') = \left(\mathbf{I} + \frac{1}{k_0^2}\nabla\nabla\cdot\right)\left(\frac{e^{jk_0|\mathbf{r}' - \mathbf{r}''|}}{4\pi|\mathbf{r}' - \mathbf{r}''|}\right). \tag{B.7}$$

Next, the Born approximation is introduced, which consists in replacing the total field on the right-hand side of Equation B.7 with the incident field only, thus assuming that the

Appendix B (Continued)

scattered field is weak with respect to the incident field or, in other words, that the scatterer is weak (small and/or with low contrast with respect to the background):

$$\mathbf{E}^{\mathrm{s}}(\mathbf{r}') \approx k_0^2 \iiint_D \mathbf{G}(\mathbf{r}', \mathbf{r}'') \cdot \left[\mathbf{E}^{\mathrm{i}}(\mathbf{r}'') v(\mathbf{r}'')\right] d\mathbf{r}''. \tag{B.8}$$

The now linear volume integral equation can be discretized into pixels at whose locations the Green's function and the incident field is evaluated and stored, obtaining the linear-algebra formulation:

$$\mathbf{E}^{\mathrm{s}} = \mathbf{L}v. \tag{B.9}$$

Appendix C

PERMISSION TO REPRODUCE CONTENT

Parts of this dissertation have been previously published in both conference and journal articles. In most cases the content of the dissertation represents a more in-depth description and analysis of the results summarized in journal or conference articles, which may include unpublished figures and/or text. In these cases the citations to the corresponding articles have been provided where appropriate even though it was not possible to refer to precise figures and/or parts of text.

However, a few paragraphs as well as some figures appear unchanged in conference and journal articles. In these cases proper references to the article and the copyright holders have been clearly indicated in the text. The permission to reproduce content has been granted by both publishers, the Institute of Electrical and Electronics Engineers (IEEE) and Hindawi Publishing Corporation.

IEEE holds the copyright to text and figures published in conference articles. Permission for reusing the material is granted from the policy which can be found at the following URL: `http://www.ieee.org/publications_standards/publications/rights/permissions_faq.pdf`. The policy states the following:

> "The IEEE does not require individuals working on a thesis to obtain a formal reuse license, however, you must follow the requirements listed below:

Appendix C (Continued)

Textual Material

Using short quotes or referring to the work within these papers) users must give full credit to the original source (author, paper, publication) followed by the IEEE copyright line ©2011 IEEE.

In the case of illustrations or tabular material, we require that the copyright line ©[Year of original publication] IEEE appear prominently with each reprinted figure and/or table.

If a substantial portion of the original paper is to be used, and if you are not the senior author, also obtain the senior author's approval."

On the other hand, the material published in the International Journal of Antennas and Propagation, published by Hindawi Publishing Corporation is available as an Open Access article. The reuse policy is available at `http://www.hindawi.com/journals/ijap/guidelines/` and states the following:

"Open Access authors retain the copyrights of their papers, and all open access articles are distributed under the terms of the Creative Commons Attribution License, which permits unrestricted use, distribution and reproduction in any medium, provided that the original work is properly cited."

CITED LITERATURE

1. Radon, J.: On the determination of functions from their integral values along certain manifolds. Medical Imaging, IEEE Transactions on, 5(4):170–176, Dec 1986.

2. Kak, A. C. and Slaney, M.: Principles of computerized tomographic imaging. Society for Industrial and Applied Mathematics, 2001.

3. Devaney, A.: Geophysical diffraction tomography. Geoscience and Remote Sensing, IEEE Transactions on, (1):3–13, 1984.

4. Akiyama, I.: Acoustical imaging.. Acoustical Imaging. Springer London, Limited, 2009.

5. Sanches, J., Laine, A., and Suri, J.: Ultrasound Imaging: Advances and Applications. SpringerLink : Bücher. Springer New York, 2012.

6. Bushberg, J., Seibert, J., Leidholdt, E., and Boone, J.: The Essential Physics of Medical Imaging. Wolters Kluwer Health, 2011.

7. Boccacci, P.: Introduction to Inverse Problems in Imaging. Taylor & Francis, 2010.

8. Turk, A., Hocaoglu, K., and Vertiy, A.: Subsurface Sensing. Wiley Series in Microwave and Optical Engineering. Wiley, 2011.

9. Planck, M.: The theory of heat radiation. Courier Dover Publications, 1959.

10. Lo Monte, L.: Radio frequency tomography for underground void detection. University of Illinois at Chicago, 2009.

11. Lo Monte, L., Erricolo, D., Soldovieri, F., and Wicks, M. C.: Radio frequency tomography for tunnel detection. IEEE Trans. Geosci. Remote Sensing, 48(3):1128–1137, Mar 2010.

12. Lo Monte, L., Erricolo, D., Soldovieri, F., and Wicks, M. C.: Rf tomography for below-ground imaging of extended areas and close-in sensing. IEEE Geoscience and Remote Sensing Letters, 7(3):496–500, Jul 2010.

CITED LITERATURE (Continued)

13. Monte, L. L., Soldovieri, F., Erricolo, D., and Wicks, M.: Radio frequency tomography for below ground imaging and surveillance of targets under cover. In Effective Surveillance for Homeland Security: Balancing Technology and Social Issues, eds. F. Flammini, R. Setola, and G. Franceschetti. Taylor & Francis/CRC Press, 2013.

14. Lo Monte, L., Soldovieri, F., Erricolo, D., and Wicks, M. C.: Imaging below irregular terrain using rf tomography. IEEE Trans. Geosci. Remote Sensing, 50(9):3364–3373, Sep 2012.

15. Picco, V., Negishi, T., Nishikata, S., Spitzer, D., and Erricolo, D.: RF Tomography in Free Space: Experimental Validation of the Forward Model and an Inversion Algorithm Based on the Algebraic Reconstruction Technique. International Journal of Antennas and Propagation, 2013. Article ID 528347, doi:10.1155/2013/528347.

16. Wicks, M. C.: RF tomography with application to ground penetrating radars. In Proc. IEEE 41st Asilomar Conference ACSSC 2007, pages 2017–2022, Nov 2007.

17. Picco, V.: Compressive Sensing for Radio Frequency Tomography. University of Illinois at Chicago, 2010.

18. Lo Monte, L., Erricolo, D., and Inan, U. S.: Radio frequency tomography for tunnel detection: principles and inversion schemes. In American Geophysical Union Fall Meeting, San Francisco, CA, Dec. 15-19, 2008.

19. L. Lo Monte and D. Erricolo: Distributed RF Tomography for Voids Detection. In 2008 Meeting of the Military Sensing Symposia Specialty Group on Battlespace Acoustic & Seismic Sensing, Magnetic & Electric Field Sensors, The Johns Hopkins University Applied Physics Laboratory, Laurel, MD, August 19-21, 2008.

20. Monte, L. L., Hayvaci, H. T., and Erricolo, D.: Propagation Model for RF Geotomography. In XXIX General Assembly of the International Union of Radio Science, Chicago, IL, Aug. 7-17, 2008.

21. Monte, L. L., Bagci, A. M., Erricolo, D., and Ansari, R.: Spatial Resolution in Tomographic Imaging with Diffracted Fields. In XXIX General Assembly of the International Union of Radio Science, Chicago, IL, Aug. 7-17, 2008.

CITED LITERATURE (Continued)

22. L. Lo Monte and D. Erricolo: Receiving Antenna Design for Ground Penetrating Tomographic Imaging. In IEEE AP-S International Symposium on Antennas and Propagation and USNC/URSI National Radio Science Meeting, San Diego, CA, July 5-12, 2008.

23. Monte, L. L., Erricolo, D., and Wicks, M. C.: Propagation Model and Receiver Design for RF Geotomography. In 2008 IEEE Radar Conference, Rome, Italy, May 26-30, 2008.

24. Lo Monte, L., Erricolo, D., Soldovieri, F., and Wicks, M. C.: Underground Imaging of Irregular Terrains Using RF Tomography. In The Third International Workshop on Computational Advances in Multi-Sensor Adaptive Processing, Aruba, Dutch Antilles, December 13-16, 2009.

25. Lo Monte, L., Erricolo, D., Ansari, R., Soldovieri, F., and Wicks, M.: Underground Imaging Using RF Tomography: The Effect of Lateral Waves. In International Conference on Electromagnetics in Advanced Applications ICEAA, Turin, Italy, Sept. 14-18, 2009.

26. Monte, L. L., Erricolo, D., Picco, V., Soldovieri, F., and Wicks, M. C.: Distributed RF Tomography for Tunnel Detection: Suitable Inversion Schemes. In National Aerospace & Electronics Conference, Dayton, OH, July 21-23, 2009.

27. Lo Monte, L., Erricolo, D., Soldovieri, F., and Wicks, M. C.: Imaging of Underground Anomalies using RF Tomography and Lateral Waves. In IEEE International Geoscience & Remote Sensing Symposium, Cape Town, South Africa, July 12-17, 2009.

28. Lo Monte, L., Erricolo, D., Soldovieri, F., and Wicks, M. C.: RF Tomography for Underground Target Detection in a Lossy and Cluttered Environment. In IEEE AP-S International Symposium on Antennas and Propagation and USNC/URSI National Radio Science Meeting, Charleston, SC, June 1-5, 2009.

29. Lo Monte, L., Ansari, R., Erricolo, D., and Wicks, M. C.: The Use of Geometric Diversity for Spectral Dominance in Underground Imaging. In Waveform Diversity Design Conference, Orlando, FL, February 8-13, 2009.

30. V. Picco and D. Erricolo and L. Lo Monte: Experimental Validation of RF Tomography. In International Union of Radio Science Commission B Electromagnetic

CITED LITERATURE (Continued)

Theory Symposium, Berlin, Germany, August 16-19, 2010.

31. Monte, L. L., Erricolo, D., Soldovieri, F., and Wicks, M.: Recent Advances in RF Tomography For Underground Imaging. In XIII International Conference on Ground Penetrating Radar, Lecce, Italy, June 21-25, 2010.

32. Monte, L. L., Picco, V., and Erricolo, D.: Image Formation in RF Tomography Using Compressive Sensing. In SIAM Conference on Imaging Science (IS10), Chicago, IL USA, Apr. 12-14 2010.

33. Picco, V., Negishi, T., Stephens, M., Nishikata, S., and Erricolo, D.: Experiments for RF Tomography. In USNC-URSI National Radio Science Meeting, Boulder, CO, USA, Jan. 4-7 2012.

34. Nishikata, S., Picco, V., Negishi, T., and Erricolo, D.: Imaging of dielectric targets using RF Tomography. In IEEE International Symposium on Antennas and Propagation/USNC-URSI National Radio Science Meeting, Chicago, IL, USA, July 8-14 2012.

35. Negishi, T., Nishikata, S., Picco, V., and Erricolo, D.: Advantages of Polarization Diversity in Microwave Tomography. In IEEE International Symposium on Antennas and Propagation/USNC-URSI National Radio Science Meeting, Chicago, IL, USA, July 8-14 2012.

36. Picco, V., Negishi, T., Nishikata, S., and Erricolo, D.: Comparison of reconstruction algorithms for Microwave Tomography. In IEEE International Symposium on Antennas and Propagation/USNC-URSI National Radio Science Meeting, Chicago, IL, USA, July 8-14 2012.

37. Negishi, T., Picco, V., and Erricolo, D.: The use of the Algebraic Reconstruction Technique (ART) for imaging of dielectric targets in Radio Frequency Tomography. In IEEE International Conference on Wireless Information Technology and Systems, Maui, HI, Nov. 11-16 2012.

38. Negishi, T., Picco, V., and Erricolo, D.: Challenge on dielectric and metallic recognition for Radio Frequency Tomography. In USNC-URSI National Radio Science Meeting, Boulder, CO, USA, Jan. 9-12 2013.

CITED LITERATURE (Continued)

39. Picco, V., Negishi, T., and Erricolo, D.: Resolution Analysis of a Radio Frequency Tomography System. In USNC-URSI National Radio Science Meeting, Boulder, CO, USA, Jan. 9-12 2013.

40. Negishi, T., Picco, V., Nishikata, S., and Erricolo, D.: Numerical Green's Function for Radio Frequency Tomography with Complex Geometry (invited). In URSI Commission B International Symposium on Electromagnetic Theory, Hiroshima, Japan, May 20-24 2013.

41. Negishi, T., Picco, V., Spitzer, D., Erricolo, D., and Monte, L. L.: Imaging Behind Obstacles Using Only Diffracted Fields. In IEEE Antennas and Propagation Society International Symposium/USNC-URSI National Radio Science Meeting, Orlando, FL, USA, July 9-13 2013.

42. Picco, V., Negishi, T., Nishikata, S., and Erricolo, D.: RF Tomography in Free Space: Experimental Validation of the Forward Model and of a Conjugate Gradient Inversion Algorithm. In International Conference on Electromagnetics in Advanced Applications, ICEAA, Torino, Italy, September 9-13 2013.

43. Picco, V., Soldovieri, F., Negishi, T., and Erricolo, D.: Quadratic Forward Model for RF Tomography: preliminary Results. In USNC-URSI National Radio Science Meeting, Boulder, CO, Jan. 8-11 2014.

44. Negishi, T., Picco, V., Spitzer, D., and Erricolo, D.: Buried Objects and Void Detection Using RF Tomography. In USNC-URSI National Radio Science Meeting, Boulder, CO, Jan. 8-11 2014.

45. Negishi, T., Picco, V., Monte, L. L., and Erricolo, D.: Anisotropic model for RF Tomography. In IEEE Antennas and Propagation Society International Symposium/USNC-URSI National Radio Science Meeting, Memphis, TN, USA, July 6-11 2014.

46. Picco, V., Gennarelli, G., Negishi, T., Erricolo, D., and Soldovieri, F.: RF Tomography Under the Quadratic Approximation. In IEEE Antennas and Propagation Society International Symposium/USNC-URSI National Radio Science Meeting, Memphis, TN, USA, July 6-11 2014.

47. Chew, W. C.: Waves and fields in inhomogeneous media. IEEE press, 1995.

48. Faires, J. and Burden, R.: Numerical Methods. Brooks/Cole, Cengage Learning, 2012.

CITED LITERATURE (Continued)

49. Hansen, P. C.: Truncated singular value decomposition solutions to discrete ill-posed problems with ill-determined numerical rank. SIAM Journal on Scientific and Statistical Computing, 11(3):503–518, 1990.

50. Golub, G. H., Hansen, P. C., and O'Leary, D. P.: Tikhonov regularization and total least squares. SIAM Journal on Matrix Analysis and Applications, 21(1):185–194, 1999.

51. Hansen, P. C.: Analysis of discrete ill-posed problems by means of the l-curve. SIAM review, 34(4):561–580, 1992.

52. Hansen, P. C.: The L-curve and its use in the numerical treatment of inverse problems. IMM, Department of Mathematical Modelling, Technical Universityof Denmark, 1999.

53. Claerbout, J. F. and Gubbins, D.: Earth sounding analysis: Processing versus inversion. Nature, 370(6486):190–190, 1994.

54. Soldovieri, F., Lo Monte, L., and Erricolo, D.: Tunnel detection and localization via multi-monostatic RF tomography using magnetic sources. IET Radar, Sonar & Navigation, 6(9):834–845, Dec. 2012.

55. Lo Monte, L., Soldovieri, F., Erricolo, D., Giannopoulos, A., and Wicks, M. C.: A Comprehensive Forward Model for Imaging Under Irregular Terrain Using RF Tomography. Int. J. Antennas Propag., 2012, 2012.

56. Parker, J. T., Ferrara, M., Bracken, J., and Himed, B.: Preliminary experimental results for rf tomography using distributed sensing. In 2010 International Conference on Electromagnetics in Advanced Applications, pages 549–552, Sept 2010.

57. Erricolo, D., D'Elia, G., and Uslenghi, P.: Measurements on scaled models of urban environments and comparisons with ray-tracing propagation simulation. IEEE Trans. Antennas Propag., 50(5):727–735, May 2002.

58. Erricolo, D., Crovella, U. G., and Uslenghi, P.: Time-domain analysis of measurements on scaled urban models with comparisons to ray-tracing propagation simulation. IEEE Trans. Antennas Propag., 50(5):736–741, May 2002.

CITED LITERATURE (Continued)

59. Erricolo, D.: Experimental validation of second order diffraction coefficients for computation of path-loss past buildings. IEEE Trans. Electromagn. Compat., 44(1):272–273, Feb. 2002.

60. Erricolo, D., Uslenghi, P., Elnour, B., and Mioc, F.: Scattering by a blade on a metallic plane. Electromagnetics, 26(1):57–71, Jan. 2006.

61. Erricolo, D., Canta, S. M., Hayvaci, H. T., and Albani, M.: Experimental and Theoretical Validation for the Incremental Theory of Diffraction. IEEE Trans. Antennas Propag., 56(8):2563–2571, Aug. 2008.

62. Negishi, T., Picco, V., Spitzer, D., Erricolo, D., Carluccio, G., F.Puggelli, and Albani, M.: Measurements to Validate the UTD Triple Diffraction Coefficient. IEEE Trans. Antennas Propag., 2014. in press.

63. Gilmore, C., Mojabi, P., Zakaria, A., Ostadrahimi, M., Kaye, C., Noghanian, S., Shafai, L., Pistorius, S., and LoVetri, J.: A wideband microwave tomography system with a novel frequency selection procedure. Biomedical Engineering, IEEE Transactions on, 57(4):894–904, april 2010.

64. Ostadrahimi, M., Mojabi, P., Noghanian, S., Shafai, L., Pistorius, S., and LoVetri, J.: A novel microwave tomography system based on the scattering probe technique. Instrumentation and Measurement, IEEE Transactions on, 61(2):379–390, 2012.

65. Mojabi, P. and LoVetri, J.: A novel microwave tomography system using a rotatable conductive enclosure. Antennas and Propagation, IEEE Transactions on, 59(5):1597–1605, 2011.

66. Solimene, R., Soldovieri, F., Baratonia, A., and Pierri, R.: Experimental validation of a linear inverse scattering twi algorithm by a sf-cw radar. Antennas and Wireless Propagation Letters, IEEE, 9:506–509, 2010.

67. Thajudeen, C., Hoorfar, A., Ahmad, F., and Dogaru, T.: Measured complex permittivity of walls with different hydration levels and the effect on power estimation of twri target returns. Progress In Electromagnetics Research B, 30:177–199, 2011.

68. Moon, T. K. and Stirling, W. C.: Mathematical methods and algorithms for signal processing, volume 1. Prentice hall Upper Saddle River, 2000.

CITED LITERATURE (Continued)

69. Nocedal, J. and Wright, S. J.: Conjugate gradient methods. Springer, 2006.

70. Nocedal, J. and Wright, S.: Numerical Optimization. Springer Series in Operations Research and Financial Engineering. Springer, 2006.

71. Shewchuk, J. R.: An introduction to the conjugate gradient method without the agonizing pain, 1994.

72. Björck, Å.: Numerical Methods for Least Squares Problems. SIAM, 1996.

73. Hansen, P.: Regularization tools version 4.0 for matlab 7.3. Numerical Algorithms, 46:189–194, 2007.

74. Daniel, J. W., Gragg, W. B., Kaufman, L., and Stewart, G.: Reorthogonalization and stable algorithms for updating the gram-schmidt ðİŚĎðİŚĚ factorization. Mathematics of Computation, 30(136):772–795, 1976.

75. Hoffmann, W.: Iterative algorithms for Gram-Schmidt orthogonalization. Computing, 41(4):335–348, 1989.

76. Slaney, M., Kak, A. C., and Larsen, L. E.: Limitations of imaging with first-order diffraction tomography. Microwave Theory and Techniques, IEEE Transactions on, 32(8):860–874, 1984.

77. Pierri, R., Soldovieri, F., Liseno, A., and De Blasio, F.: Dielectric profiles reconstruction via the quadratic approach in 2-d geometry from multifrequency and multifrequency/multiview data. Geoscience and Remote Sensing, IEEE Transactions on, 40(12):2709–2718, Dec 2002.

78. Kaczmarz, S.: Angenaherte auflosung von systemen linearer gleichungen. Bulletin International de l'Academie Polonaise des Sciences et des Lettres, 35:355–357, 1937. `http://jasonstockmann.com/Jason_Stockmann/Welcome_files/kaczmarz_english_translation_1937.pdf`.

79. Gordon, R., Bender, R., and Herman, G. T.: Algebraic reconstruction techniques (art) for three-dimensional electron microscopy and x-ray photography. Journal of Theoretical Biology, 29(3):471 – 481, 1970.

CITED LITERATURE (Continued)

80. Herman, G.: Fundamentals of Computerized Tomography: Image Reconstruction from Projections. Advances in Computer Vision and Pattern Recognition. Springer, 2009.

81. Basser, P. J. and Jones, D. K.: Diffusion-tensor mri: theory, experimental design and data analysis–a technical review. NMR in Biomedicine, 15(7-8):456–467, 2002.

82. Stieltjes, B., Kaufmann, W. E., van Zijl, P., Fredericksen, K., Pearlson, G. D., Solaiyappan, M., and Mori, S.: Diffusion tensor imaging and axonal tracking in the human brainstem. Neuroimage, 14(3):723–735, 2001.

83. Mori, S., Zhang, J., et al.: Principles of diffusion tensor imaging and its applications to basic neuroscience research. Neuron, 51(5):527, 2006.

84. Balanis, C.: Advanced Engineering Electromagnetics. CourseSmart Series. Wiley, 2012.

85. Harrington, R.: Time-Harmonic Electromagnetic Fields. IEEE Press Series on Electromagnetic Wave Theory. Wiley, 2001.

86. Uslenghi, P.: Electromagnetic Scattering. Elsevier Science, 1978.

87. Richmond, J.: Scattering by a dielectric cylinder of arbitrary cross section shape. Antennas and Propagation, IEEE Transactions on, 13(3):334–341, 1965.

88. Wang, Y. and Chew, W.: An iterative solution of the two-dimensional electromagnetic inverse scattering problem. International Journal of Imaging Systems and Technology, 1(1):100–108, 1989.

89. Chew, W. and Wang, Y.: Reconstruction of two-dimensional permittivity distribution using the distorted born iterative method. Medical Imaging, IEEE Transactions on, 9(2):218–225, 1990.

90. Leone, G., Brancaccio, A., and Pierri, R.: Linear and quadratic inverse scattering for angularly varying circular cylinders. JOSA A, 16(12):2887–2895, 1999.

91. Pierri, R. and Leone, G.: Inverse scattering of dielectric cylinders by a second-order born approximation. Geoscience and Remote Sensing, IEEE Transactions on, 37(1):374–382, 1999.

CITED LITERATURE (Continued)

92. Pierri, R., Soldovieri, F., Liseno, A., and De Blasio, F.: Dielectric profiles reconstruction via the quadratic approach in 2-d geometry from multifrequency and multifrequency/multiview data. Geoscience and Remote Sensing, IEEE Transactions on, 40(12):2709–2718, 2002.

93. Levenberg, K.: A method for the solution of certain problems in least squares. Quarterly of applied mathematics, 2:164–168, 1944.

94. Marquardt, D. W.: An algorithm for least-squares estimation of nonlinear parameters. Journal of the Society for Industrial & Applied Mathematics, 11(2):431–441, 1963.

95. Riddle, B., Baker-Jarvis, J., and Krupka, J.: Complex permittivity measurements of common plastics over variable temperatures. Microwave Theory and Techniques, IEEE Transactions on, 51(3):727–733, Mar 2003.

96. Knott, E. F. and Senior, T.: Studies of scattering by cellular plastic materials. 1964.

VITA

NAME: Vittorio Picco

EDUCATION:

Laurea, Ingegneria Elettronica
Politecnico di Torino, Italy, 2007

Laurea Specialistica, Ingegneria delle Telecomunicazioni
Politecnico di Torino, Italy, 2010

M.S., Electrical and Computer Engineering
University of Illinois at Chicago, 2010

Ph.D., Electrical and Computer Engineering
University of Illinois at Chicago, 2014

EXPERIENCE:

Process Engineer Intern, Michelin
Cuneo, Italy, 06/2007 – 07/2007

Interpretation Engineer Intern, Schlumberger
Houston, TX, 06/2012 – 08/2012

Intern, Schlumberger
Sugar Land, TX, 05/2013 – 08/2013

Research and Teaching Assistant
Department of Electrical and Computer Engineering
University of Illinois at Chicago, IL, 01/2010 – 06/2014

AWARDS:

TOP-UIC Fellowship, Politecnico di Torino, 2007
Fellowship to support university attendance in the United States

IEEE AP-S Student Design Challenge, 2011
Received funding for building design prototype, reached final stage,
invited to the 2011 IEEE AP-S Symposium and achieved final 3rd place

The National Academies Travel Fellowship, 2012 – 2013
Travel fellowship to support conference attendance

VITA (Continued)

PUBLICATIONS:

Lo Monte L., Erricolo D., Picco V., Soldovieri F., Wicks M.C.: Distributed RF Tomography for Tunnel Detection: Suitable Inversion Schemes, IEEE NAECON 2009, Fairborn, OH, USA

Picco V., Erricolo D., Lo Monte L.: Experimental Validation of RF Tomography,
URSI International Symposium on Electromagnetic Theory, EMTS, Berlin 2010

Picco V., Martin K.: An Automated Antenna Measurement System Utilizing Wi-Fi Hardware,
2011 IEEE International Symposium on Antennas and Propagation and CNC/USNC/URSI Radio Science Meeting, Spokane, WA, 2011

Picco V., Martin K.: An Automated Antenna Measurement System Utilizing Wi-Fi Hardware, IEEE AP-S Magazine, Vol. 53, No. 6, Dec. 2011

Picco V., Negishi T., Stephens M., Nishikata S., Erricolo D.: Experiments for RF Tomography,
URSI National Radio Science Meeting, Boulder, CO, 2012

Nishikata S., Picco V., Negishi T., Erricolo D.: Imaging of dielectric targets using RF Tomography, In
2012 IEEE International Symposium on Antennas and Propagation and CNC/USNC/URSI Radio Science Meeting, July 2012, Chicago, IL

Negishi T., Nishikata S., Picco V., Erricolo D.: Advantages of Polarization Diversity in Microwave Tomography, In
2012 IEEE International Symposium on Antennas and Propagation and CNC/USNC/URSI Radio Science Meeting, July 2012, Chicago, IL

Picco V., Negishi T., Nishikata S., Erricolo D.: Comparison of reconstruction algorithms for Microwave Tomography, with applications to experimental data, In
2012 IEEE International Symposium on Antennas and Propagation and CNC/USNC/URSI Radio Science Meeting, July 2012, Chicago, IL

VITA (Continued)

Picco V., Negishi T., Erricolo D.: Resolution Analysis of a Radio Frequency Tomography System,
URSI National Radio Science Meeting, Boulder, CO, 2013

Negishi T., Picco V., Erricolo D.: Challenge on Dielectric and Metallic Targets Recognition for Radio Frequency Tomography,
URSI National Radio Science Meeting, Boulder, CO, 2013

Negishi T., Picco V., Nishikata S., Erricolo D.: Numerical GreenâĂŹs Function for Radio Frequency Tomography with Complex Geometry,
URSI International Symposium on Electromagnetic Theory, EMTS, Berlin 2013

Negishi T., Picco V., Spitzer D., Erricolo D., Lo Monte L.: Imaging Behind Obstacles Using Only Diffracted Fields, In
2013 IEEE International Symposium on Antennas and Propagation and CNC/USNC/URSI Radio Science Meeting, July 2013, Orlando, FL

Picco V., Negishi T., Spitzer D., Erricolo D., Carluccio G., Puggelli F., Albani M.: Experimental Validation of the UTD Third Order Diffraction Coefficient, In
2013 IEEE International Symposium on Antennas and Propagation and CNC/USNC/URSI Radio Science Meeting, July 2013, Orlando, FL

Picco V., Negishi T., Nishikata S., Erricolo D.: RF Tomography in Free Space: Experimental Validation of the Forward Model and of a Conjugate Gradient Inversion Algorithm, In
International Conference on Electromagnetics in Advanced Applications, ICEAA, September 2013, Torino, Italy

Picco V., Soldovieri S., Negishi T., Erricolo D.: Quadratic Forward Model for RF Tomography: Preliminary Results,
URSI National Radio Science Meeting, Boulder, CO, 2014

Negishi T., Picco V., Spitzer D., Erricolo D.: Buried objects and void detection using RF Tomography,
URSI National Radio Science Meeting, Boulder, CO, 2014

VITA (Continued)

Negishi T., Picco V., Lo Monte L., Erricolo D.: Anisotropic model for RF Tomography, In
2014 IEEE International Symposium on Antennas and Propagation and CNC/USNC/URSI Radio Science Meeting, July 2014, Memphis, TN

Picco V., Gennarelli G., Negishi T., Erricolo D., Soldovieri F.: RF Tomography Under the Quadratic Approximation, In
2014 IEEE International Symposium on Antennas and Propagation and CNC/USNC/URSI Radio Science Meeting, July 2014, Memphis, TN

Negishi T., Picco V., Spitzer D., Erricolo D., Carluccio G., Puggelli F., Albani M.: Measurements to Validate the UTD Triple Diffraction Coefficient, IEEE Transactions on Antennas and Propagation, in print

Picco V., Negishi T., Nishikata S., Spitzer D., Erricolo D.: RF Tomography in Free Space: Experimental Validation of the Forward Model and of an Inversion Algorithm based on the Algebraic Reconstruction Technique,
International Journal of Antennas and Propagation, vol. 2013, Article ID 528347, 2013